Flow in Fractured Chalk

Final Report for EFP-98 Project no. 1313/98-0008

Dan Olsen, Niels Bech, Carsten Møller Nielsen,
Flemming If and Jesper W. Christensen

GEUS

Flow in Fractured Chalk

Final Report for EFP-98 Project no. 1313/98-0008

Dan Olsen, Niels Bech, Carsten Møller Nielsen,
Flemming If and Jesper W. Christensen

Contents

Appendix E   Nørgaard, Olsen, Reffstrup & Springer, *SPE Reservoir Evaluation and Engineering **2,2**, p 141-148, 1999.*

Appendix F   Bech, Olsen & Nielsen*, abstract accepted for presentation at SPE Annual Technical Conference and Exhibition, 30 September – 3 October 2001, New Orleans, 2001.*

Summary

The aim of the project is to improve the knowledge of flow mechanisms in fractured chalk reservoirs, and to improve the simulation tools for studying such reservoirs.

Fractured plugs of chalk from wells in the Danish North Sea were used for flooding experiments simulating the behaviour of a fractured oil reservoir. The experiments were monitored by a chemical shift NMR technique quantifying the distribution of fluids during the experiments.

The fluid system H_2O – D_2O, i.e. light water – heavy water, was used for studying the permeability of fractures. Results show that within a single fracture large permeability variations sometimes exist within distances of a few centimeters. In other instances the permeability distribution is much more homogeneous. An unexpected, but reproducible, pressure evolution remains unexplained.

The fluid system H_2O – D_2O – oil was used in a model of a waterflooding operation on a fractured reservoir containing oil and connate water. The experiments give detailed descriptions of fluid movements inside the sample matrix and between matrix and fracture during waterfloods. In particular it is seen that the connate water become mobilized by the injection water and travels ahead of the injection water as a bank. The mobile oil of the sample mainly becomes mobilized by this bank of connate water, and the produced oil experiences little contact with the injection water.

The H_2O – D_2O – oil experiments were simulated by a reservoir simulator. In general the agreement between experiment and model is good. The banking of connate water is well displayed by the simulations. Instances of disagreement between experiment and model are mainly attributed to the inhomogeneity of the sample, fracture system, and initial fluid saturation. The simulations show that most of the oil is produced by counter-current flow. An additional cause of the disagreement between experiments and simulation may be the use of co-current saturation functions for the whole experiment

A separate study compares capillary pressure functions determined by the porous plate technique, the mercury injection technique and the BON method. Fair agreement exists between the porous plate technique and the BON-method, with greater discrepancy between these and the mercury injection method. NMR determinations of the fluid distributions reveal considerable inhomogeneity mainly caused by hairlines of the sample. The porous plate experiment is not yet completed, due to the time requirement of this technique.

It has been investigated to which extent it is possible with a double-porosity model to reproduce results from a detailed single-porosity description. The work was concentrated on the oil/water system. It is concluded that the single-porosity description should be used whenever it is practically possible. That is, when the density of larger fractures is so small that they can be described individually. In all other situations the double-porosity/double permeability model must be used with pseudo capillary pressure and relative permeability functions.

Simulation results of small-scale models of water flooding of low permeable fractured system have been examined in detail. It has been shown analytically how to derive the matrix and fracture properties, in order to describe a specific fracture trajectory in the double continuum formulation. The results from these small-scale models have been used to derive a fast and easy applicable method for estimation of the magnitude of the shape factors for arbitrary fracture patterns.

Results from the project have so far been published in 2 refereed articles, 2 technical papers, and 1 technical report. One abstract has been accepted for presentation.

Introduction

The project "Flow in fractured chalk" with the Danish title "Strømning i opsprækket kalk" was financed by the Ministry of Environment and Energy through the EFP-98 research programme grant ENS J.no. 1313 / 98-0008. It was a co-operation between COWI Rådgivende Ingeniører AS (COWI) and Geological Survey of Denmark and Greenland (GEUS).

The aim of the project was to improve the understanding of flow mechanisms in fractured chalk reservoirs. One element of the project was displacement experiments on fractured chalk core samples, with subsequent computer simulation of the experimental results. Another project element was methodological improvements of up-scaling and simulation procedures for fractured reservoirs.

Four tasks were defined in the project:
- Task 1. Determination of absolute permeability for matrix and fracture (GEUS).
- Task 2. Determinations of saturation functions for matrix and fracture (GEUS).
- Task 3. Description of the flow of oil and water between matrix and fracture in a double porosity model (GEUS).
- Task 4. Development of a method for two-phase up-scaling (COWI)

A major part of the project (Tasks 1 and 2) was concerned with experimental work on fractured core plugs of Maastrichtian age from wells in the Danish North Sea. The investigated fractures were artificially induced. A number of displacement experiments were monitored by a Nuclear Magnetic Resonance (NMR) technique giving information of the fluid distribution within the sample material. The experimental work was done at GEUS, while the NMR work was done at Danish Research Centre of Magnetic Resonance (DRCMR). The experiments were simulated by a reservoir simulator (ECLIPSE), and the production mechanisms and the dynamics of the matrix-fracture exchange were analysed.

In Task 3 the flow of oil and water between fracture and matrix in a core plug was described by means of a dual-porosity models with difference grids of varying fineness. The objective of this work was to investigate to which extent it is possible to reproduce results from the detailed single-porosity description and to find out how much faster (or slower) the double-porosity model is.

Simulation results of small-scale models of water flooding of low permeable fractured system were examined in detail in Task 4. It was shown analytically how to derive the matrix and fracture properties, in order to describe a specific fracture trajectory in the double continuum formulation. The results from these small-scale models were used to derive a fast and easy applicable method for estimation of the magnitude of the shape factors for arbitrary fracture patterns.

Most of the work of the project "Flow in fractured chalk" has been published. For the published work this report only contains short summaries with references to the relevant publications, that are included as appendices. Some work, as yet unpublished, is described in more detail.

Task 1: Determination of absolute permeability for matrix and fracture (GEUS)

The fluid system H_2O – D_2O, i.e. light water – heavy water, is a fully miscible two component, one phase fluid system. Working with this system in a porous medium has the advantage of eliminating all effects from capillary pressure, and reducing relative permeability to a simple linear relationship. Determination of absolute permeability then becomes simplified. A spin echo NMR technique was used to determine the spatial distribution of H_2O during two flooding experiments on core samples containing a single fracture along the sample axis, giving information about the fluid movements between matrix and fracture.

The first experiment showed the existence of a significant permeability variation along the fracture, and the experimental results were simulated by a reservoir simulator in order to quantify the variation. A permeability variation along the fracture in excess of a factor 10 was indicated by the simulation. The experiment and the results are described in Olsen et al. (2000), cf. Appendix C. A second flooding experiment on another core sample, using the same experimental set-up, showed a regular piston displacement indicating a smooth pressure gradient along the sample. This indicates that only small permeability variations existed along the fracture in this experiment, and therefore, the experimental results on this sample were not simulated.

The two miscible flooding experiments behaved quite differently. One experiment indicates the existence of large permeability variations over centimeter-size distances along the length of a fracture, while the other experiment indicates the existence of a much smoother permeability profile. In reservoir simulation of fractured reservoirs it is commonly assumed that the permeability along a fracture is constant. The present work shows that sometimes this assumption is in error, though it do not give any indication of the magnitude and frequency of fracture permeability variations in a real reservoir.

Injection pressure in miscible displacement experiments

During the two miscible displacement experiments an unexpected increase in injection pressure was observed. The pressure increase was described for the first experiment in Olsen et al. (2000), Appendix C, and tentatively explained as fines deposition around fracture blockages. In the second experiment the same progress of increase in injection pressure was observed, again. But any growth in fracture blockage was not detectable from the NMR pictures. So the cause of increase in pressure was not understood. For both experiments the pressure increased 2-3 times the initial injection pressure.

The increase was not to be explained by the difference in viscosities between light water and heavy water, as the viscosity of heavy water is 1.23 times that of light water. So, for the displacement of heavy water with light water a decrease in injection pressure was to be expected. The linearity between applied flow rate and pressure drop was checked for the flow rate interval used in the displacement experiments and no secondary effects were detectable.

Additional experiments were then conducted in order to investigate this phenomenon. For the sample used in the experiment of Olsen et al. (2000) the fracture was closed with epoxy. Then the miscible displacement experiment was repeated. The recorded progress in injection pressure now developed as expected, i.e. a slight *decrease* in pressure, which precisely balanced the ratio of the viscosities for the displacement.

Two supplementary samples were used to further examine whether it was the choice of fluid system and/or the presence of a fracture plane that caused the anomalous pressure increase. The two samples were chosen to be lithologically similar to the sample used in Olsen et al. (2000). From the suite of miscible flooding experiments the following was concluded:

- The progress in recorded injection pressure may be solely explained by the difference in viscosities in the following instances:
  - when H_2O displaces D_2O in a non-fractured sample.
  - when H_2O displaces methanol both in a non-fractured and fractured sample.
  - when H_2O displaces H_2O in a fractured sample.

- When H_2O displaces D_2O in a fractured sample a puzzling and significant increase in injection pressure is recorded.

The project did not succeed to bring an explanation for the phenomenon. Whether it is caused by some physical-chemical difference between light water and heavy water in conjunction with the presence of a fracture remains to be resolved.

Task 2: Determination of saturation functions for matrix and fracture (GEUS)

Waterflooding operations on a fractured chalk reservoir were investigated by displacement experiments on chalk core plugs with induced fractures. The experiments used the fluid system H_2O – D_2O – n-decane, i.e. light water – heavy water − oil, which is a three component, two phase system. Within a chalk sample, the spatial distribution of the components H_2O and oil were quantitatively determined by a Chemical Shift Imaging (CSI) NMR technique (Nielsen et al., 2000, Appendix B). Experiments were conducted with two samples of chalk, each containing a single fracture along the sample axis. The same samples were used in Task 1 for the miscible displacement experiments. For the second sample, N36D, matrix saturation functions were determined by the BON-method, (Bech et al., 2000, Appendix A) prior to the H_2O – D_2O − oil experiment and prior to sample fracturing. These saturation functions were later used in the simulation of the experiments on the fractured sample. For the first sample, M16I, saturation functions determined by the BON-method on another, but similar, sample (M16H) were used.

Initially the samples contained n-decane and D_2O-brine. The saturation of D_2O-brine was respectively 12 % and 27 % at the start of the two experiments. Each sample was flooded with H_2O-brine displacing the oil and D_2O-brine until it contained H_2O-brine and residual oil. During the experiments the distribution of H_2O-brine and oil was monitored by CSI NMR. The distribution of D_2O-brine was not directly determined, but was calculated from the assumption that the signal response per H-atom was constant for each voxel during the experiment. In this way the D_2O-saturation of a particular voxel at a particular time was calculated from the difference between the total signal of the voxel at that time and the total signal of the same voxel at the end of the experiment, where the voxel only contained H_2O-brine and oil. The experimental results were simulated by a reservoir simulator to obtain information about the fluid movements.

Nielsen et al. (2000) describes the first experiment, cf. Appendix B. The second experiment confirms the main results of the first experiment. At the time of writing the second experiment has not been published. It is described later in this section.

The experiments were designed to simulate a chalk reservoir, where oil and connate water were displaced by injected water. Connate water was simulated by D_2O-brine, and injection water was simulated by H_2O-brine. The two experiments are in good accordance about the course of the displacement. The injection water enters each sample from the inlet end in a well defined piston front that moves through the sample. At the same time capillary forces pull injection water from the fracture into the matrix, creating a second front that moves into the matrix from the fracture plane. Ahead of these two fronts, the connate water is mobilized and travels as a bank, reaching saturations exceeding 50 % in parts of both samples. The oil in the sample is mainly produced by interaction with the water in this bank of connate water. The injection water has only limited contact with the produced oil. When injection water, during the course of the displacement, gets in contact with oil, the local oil saturation is getting close to S_{or} , and the oil has mainly become immobile and possibly partly disconnected. This

finding may have significance for the application of chemical EOR processes in connection with waterflooding operations on chalk reservoirs.

Another finding of the experiments is that saturation contrasts caused by hairlines were significantly weakened during waterflooding. At the start of the experiments the hairlines were distinguished from the matrix by large saturation contrasts, while at the end of the waterflooding only small saturation contrasts remained.

The course of the experiments was simulated with fair agreement by ECLIPSE. In particular, the connate water bank was well simulated, though the size of the bank tends to be underpredicted. The inhomogeneity of the samples made precise simulation difficult. Counter-current flow was the dominant flow mechanism for producing most of the oil from the samples.
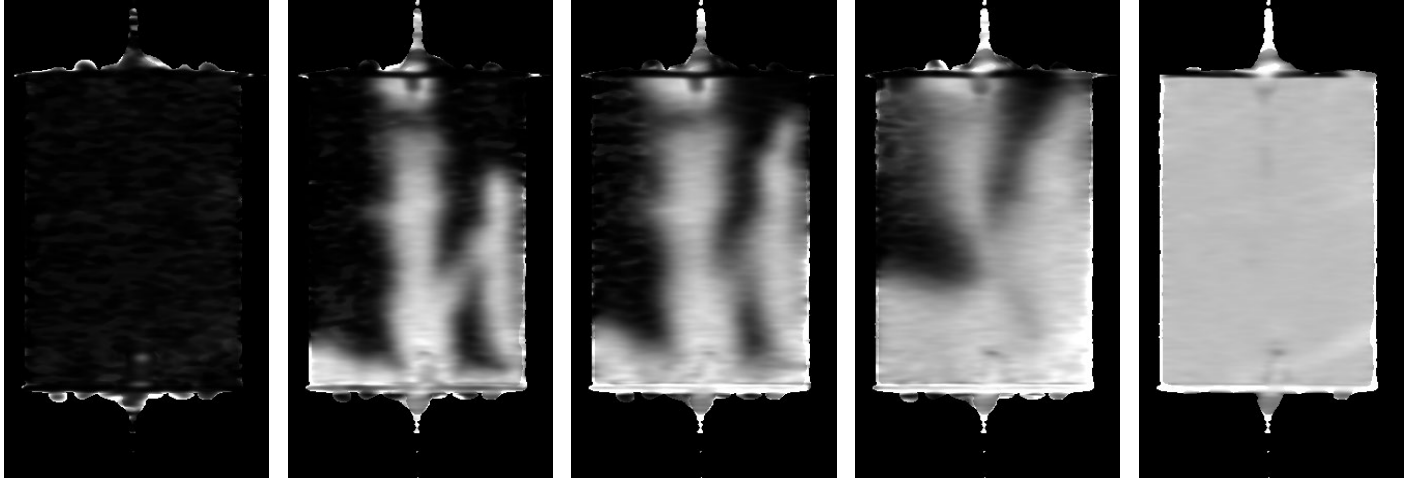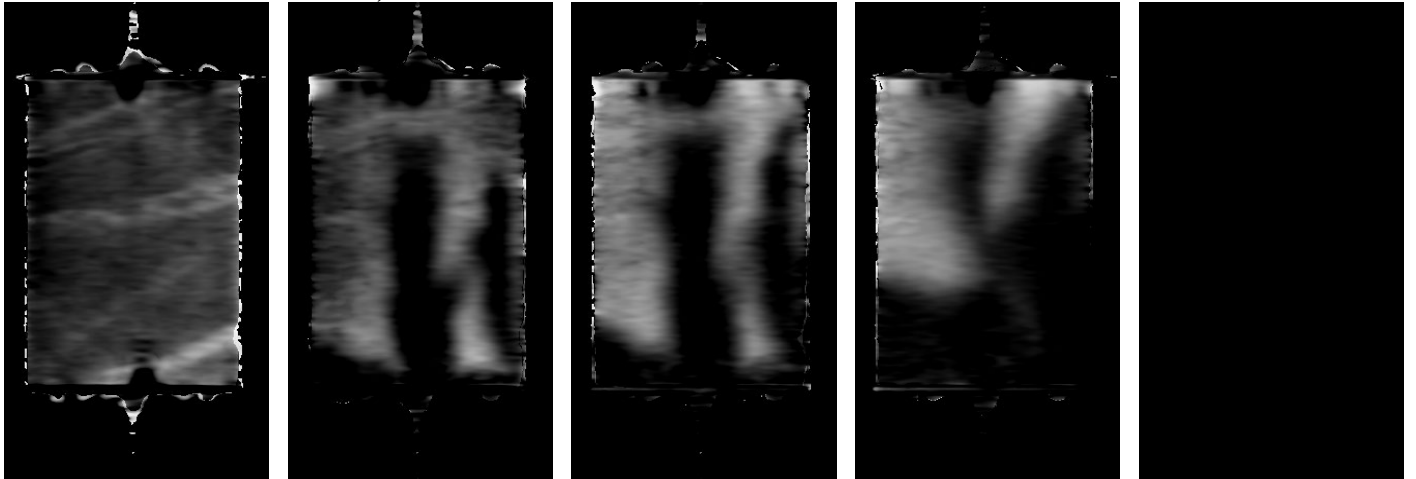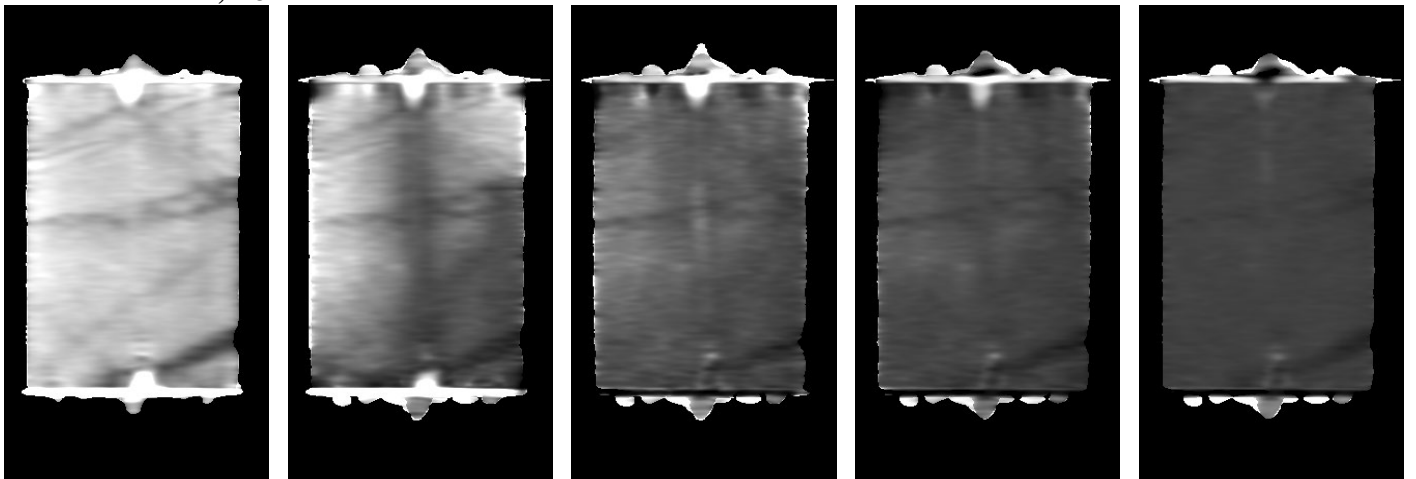
Attempts to determine saturation functions for the fractures were not successful, because of too little sensitivity of the measured saturation distribution to the changes in the fracture saturation functions.

Immiscible displacement experiment on sample N36D

To verify the results obtained from the first immiscible displacement experiment on sample M16I (Nielsen et al., 2000, Appendix B) the experimental protocol was repeated on sample N36D, a chalk sample of Maastrichtian age from the Gorm N-36A well. As in the first experiment H_2O-brine was used as injection water, and D_2O-brine was used as connate water.
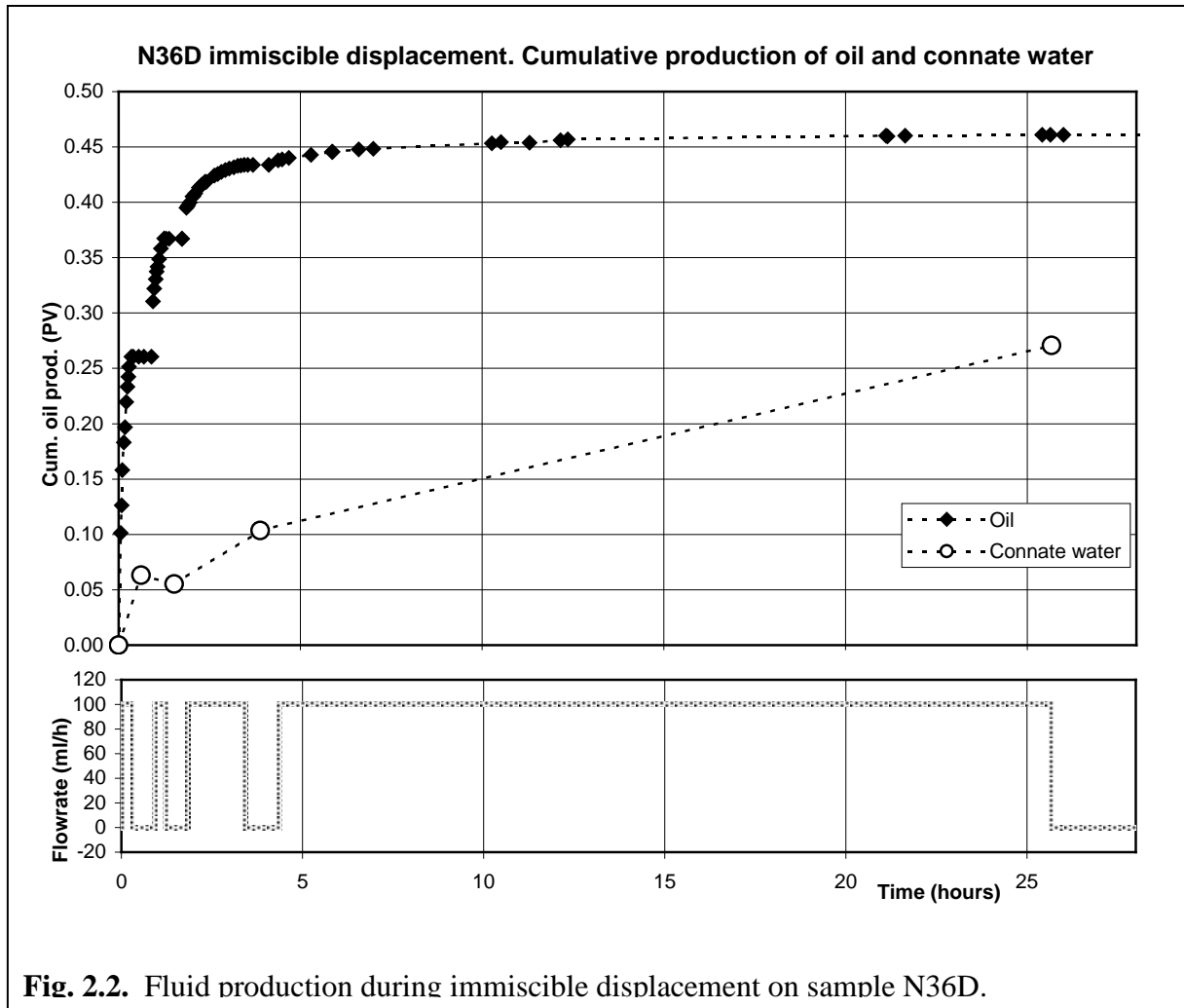
Initially, the saturation functions for the matrix of the sample were determined by the BON-method (Bech et al. 2000, Appendix A). An axial fracture was then induced in the sample. The sample was saturated with D_2O-brine to 100 %, was placed on a porous plate, and drained to S_{wir} with n-decane. At the end of the drainage the sample contained 73 % n-decane and 27 % D_2O-brine. From this state the immiscible displacement experiment started by flooding with H_2O-brine at a rate of 100 ml/h, and monitoring by CSI NMR. The flooding was stopped three times to allow acquisition of quantitative NMR data sets. In the case of the M16I experiment the signal/noise-ratio in part of the sample was significantly lowered by the accidental introduction of some relaxation-enhancing compound. This was avoided for sample N36D. As in the case of M16I, the distribution of D_2O-brine was not directly measured, but was calculated from the assumption that the signal response per H-atom was constant for each voxel during the experiment.

The experiment allowed the calculation of the distribution of all three fluid components at five times during the experiment, i.e. at the start and end and at the three intermediate flow-stops. The calculated fluid distributions are shown in Fig. 2.1. Initially, the injection water rapidly fills the main fracture, and also a set of secondary fractures, which appears in the right part of the saturation models. The injection water rapidly begins imbibing into the sample from the fracture, and from the inlet end plane it enters the sample by a combination of imbibition and forced injection. In the right part of the sample, as seen on Fig. 2.1, relations are complicated by the existence of the set of secondary fractures. These fractures were caused by the handling of the sample. In the left part of the sample a fairly simple situation is seen. The injection water traverses the sample with a well defined front, progressing both from the fracture plane and the inlet end. Ahead of the injection water front the connate water is mobi-

Injection water distribution, S_{H2O}

| S_{H2O}=.04 | S_{H2O}=.31 | S_{H2O}=.39 | S_{H2O}=.52 | S_{H2O}=.74 |

Connate water distribution, S_{D2O}

| S_{D2O}=.20 | S_{D2O}=.19 | S_{D2O}=.24 | S_{D2O}=.19 | S_{D2O}=.00 |

Oil distribution, S_O

| S_{OIL}=.76 | S_{OIL}=.50 | S_{OIL}=.37 | S_{OIL}=.29 | S_{OIL}=.26 |

Step:	Start	Flowstop 1	Flowstop 2	Flowstop 3	End
Inj. (PV):	0.00	1.40	2.79	10.04	106.90
Time (h):	0.00	0.31	0.61	2.21	23.51

Fig. 2.1. Distribution of fluids in sample N36D during immiscible experiment. Flow direction is upwards. For each model is indicated the mean fluid saturation. Fluid saturation is visualized with a grey tone scale, where 0 % is black, and 100 % is white. Field of view is 6 x 9 cm.

N36D immiscible displacement. Cumulative production of oil and connate water

Fig. 2.2. Fluid production during immiscible displacement on sample N36D.

lized and travels as a bank, reaching saturations above 50 % in large parts of the sample. The oil in the sample is produced much more rapidly than the connate water (Fig. 2.2), and is mainly produced by interaction with the bank of connate water. The injection water has little contact with the produced oil. These results are in close agreement with the experiment on M16I (Nielsen et al., 2000, Appendix B). It is further found that saturation contrasts caused by hairlines are significantly reduced during the water injection. At the end of the experiment the hairlines only have a modest influence on the saturation distribution.

Numerical simulation of immiscible displacement experiment on sample N36D

The immiscible flooding experiment with the core plug N36D has been simulated by means of the ECLIPSE reservoir simulator. The set-up closely follows the simulation of core plug M16I as described in Nielsen et al. (2000), Appendix B. Modelling assumptions imposed are:

- The plug is homogeneous.
- The cylindrical core plug contains a single vertical fracture plane through the axis.
- The initial saturation distribution is uniform (27% D2O and 73% oil).
- The flow pattern in the plug is symmetric with respect to the fracture plane and a plane perpendicular to the fracture plane through the plug axis.

TABLE 2 - Plug N36D Simulation Grid		
$n_x = 62$	Δx	= 0.09783 cm
$n_y = 25$	Δy_1	= 0.0025 cm
	Δy_2	= 0.0036 cm
	Δy_3	= 0.0053 cm
	Δy_4	= 0.0077 cm
	Δy_5	= 0.0113 cm
	Δy_6	= 0.0164 cm
	Δy_7	= 0.0240 cm
	Δy_8	= 0.0349 cm
	Δy_9	= 0.0509 cm
	Δy_{10}	= 0.0742 cm
	Δy_{11}	= 0.1080 cm
	Δy_{12-25}	= 0.11134cm
$n_z = 16$	Δz	= 0.11859 cm

TABLE 1 - Dimensions of Core Plug N36D	
L_{plug}	5.87 cm
D_{plug}	3.795 cm
a	0.005 cm

TABLE 3 - Core Plug N36D Rock and Fluid Properties	
K_m	1.6 mD
K_f	2.9E4 mD
φ_m	0.318
φ_f	1.0
C_{rock}	1.76E-3 1/bar
C_w	4.48E-5 1/bar
μ_w	1.12 cp
C_o	1.11E-4 1/bar
μ_o	0.92cp

The latter assumption does not hold which is evident from the NMR images. Secondary fractures in the right half of the plug attract plenty of water. It is believed, however, that it is possible to model the development in the left half of the plug by the assumptions stated above.

Grid. The dimensions of the plug are given in Table 1. Please refer to the end of this section for nomenclature. The assumptions made dictate that only one quarter of the plug is considered. This quarter plug section and its bounding inlet and outlet chambers are modelled by means of a 3D Cartesian grid with $(n_x, n_y, n_z) = (62, 25, 16)$, see Table 2. The inlet and outlet chambers are modelled by the grid planes $i = 1$ and $i = n_x$, respectively. The core plug thus contains 60*25*16 = 24000 grid cells.

Rock Properties. Plug porosity and absolute permeability were determined before fracturing to 0.3186 and 1.6 mD, respectively. The permeability of the induced fracture was determined from the total pressure drop, Δp_T, across the plug measured during the experiment. The initial 3.4 hr of the experiment has been simulated (Effective flow time: 2.2 hr). During this period the total pressure drop varied between 0.3 bar and 0.35 bar corresponding to an average permeability, K_{av}, around 50 mD. Neglecting the difference between the water and oil viscosities we have:

$$Q_T = \frac{A_T K_{av} \Delta p}{\mu L} \qquad \text{Eq. 2.1}$$

$$Q_m = \frac{A_m K_{m,eff} \Delta p}{\mu L} \qquad \text{Eq. 2.2}$$

$$Q_f = \frac{A_f K_f \Delta p}{\mu L} \qquad \text{Eq. 2.3}$$

leading to

$$K_f = K_{m,eff} + \frac{\pi r_{plug} (K_{av} - K_{m,eff})}{2a} \qquad \text{Eq. 2.4}$$

or

$$K_f \cong \frac{\pi r_{plug} K_{av}}{2a}$$
<div align="right">Eq. 2.5</div>

The plug radius is 1.8975 cm and the aperture of the fracture is estimated to 0.005 cm. With $K_{av} = 50$ mD we find $K_f = 2.9E4$ mD.

The rock and fluid properties are shown in Table 3.

Saturation Functions. Capillary pressure and relative permeabilities was determined by the BON method (Bech et al. 2000, Appendix A). The relative permeability and capillary pressure functions are shown in Fig. 2.3.

Operating Conditions. From time zero, light water was injected at a constant rate of 100 ml/hr. In the simulations, the injected water (H_2O) was doped with a passive tracer in order to permit a distinction between injection water and formation water (D_2O). In order to create a uniform inlet velocity the water injection was carried out through n_y wells completed in each of the n_z layers as described in Olsen et al. 2000, Appendix C.

Results.
Flow Patterns. Several observations can be made from the oil and water flow patterns calculated at different points of time:

- Oil is produced by counter-current flow to the inlet chamber.
- Oil is produced by counter-current flow to the fracture.
- Oil is produced to the outlet chamber by
  - co-current flow in the very beginning and at later times.
  - a mixture of co-current and more or less counter-current flow at intermediate times,
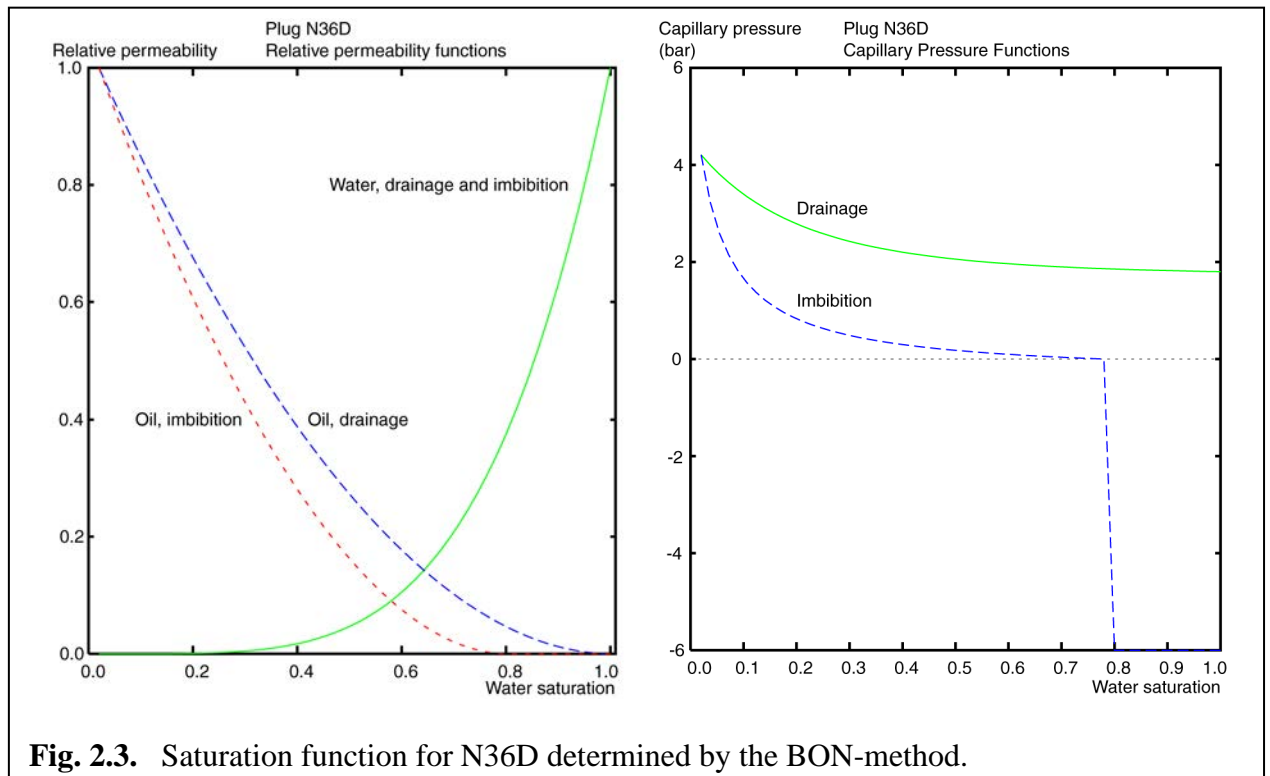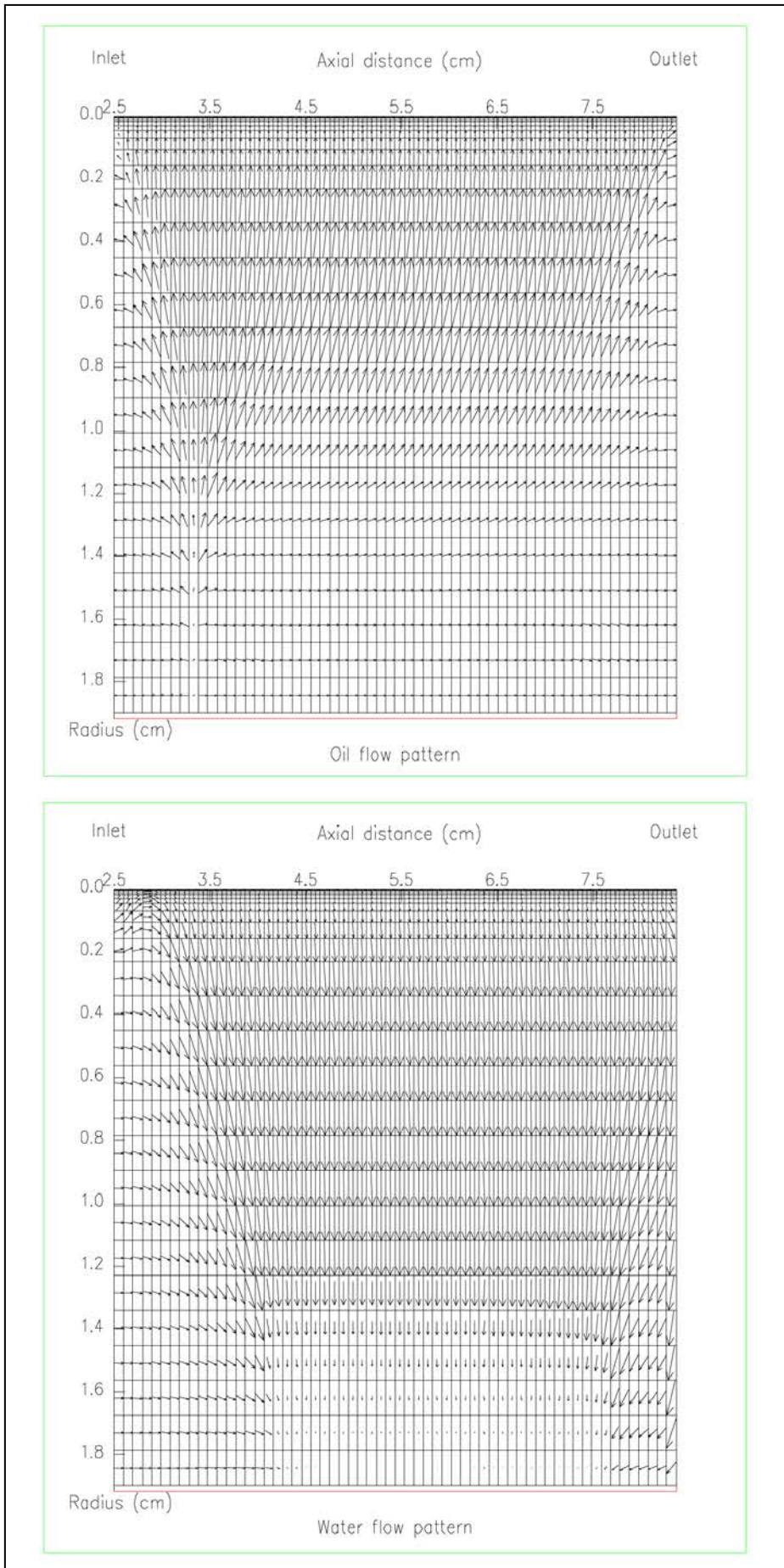

Fig. 2.3. Saturation function for N36D determined by the BON-method.

where water im-
bibes from the out-
let chamber back
into the plug.

Oil flow pattern

Water flow pattern

Fig. 2.4. Oil and
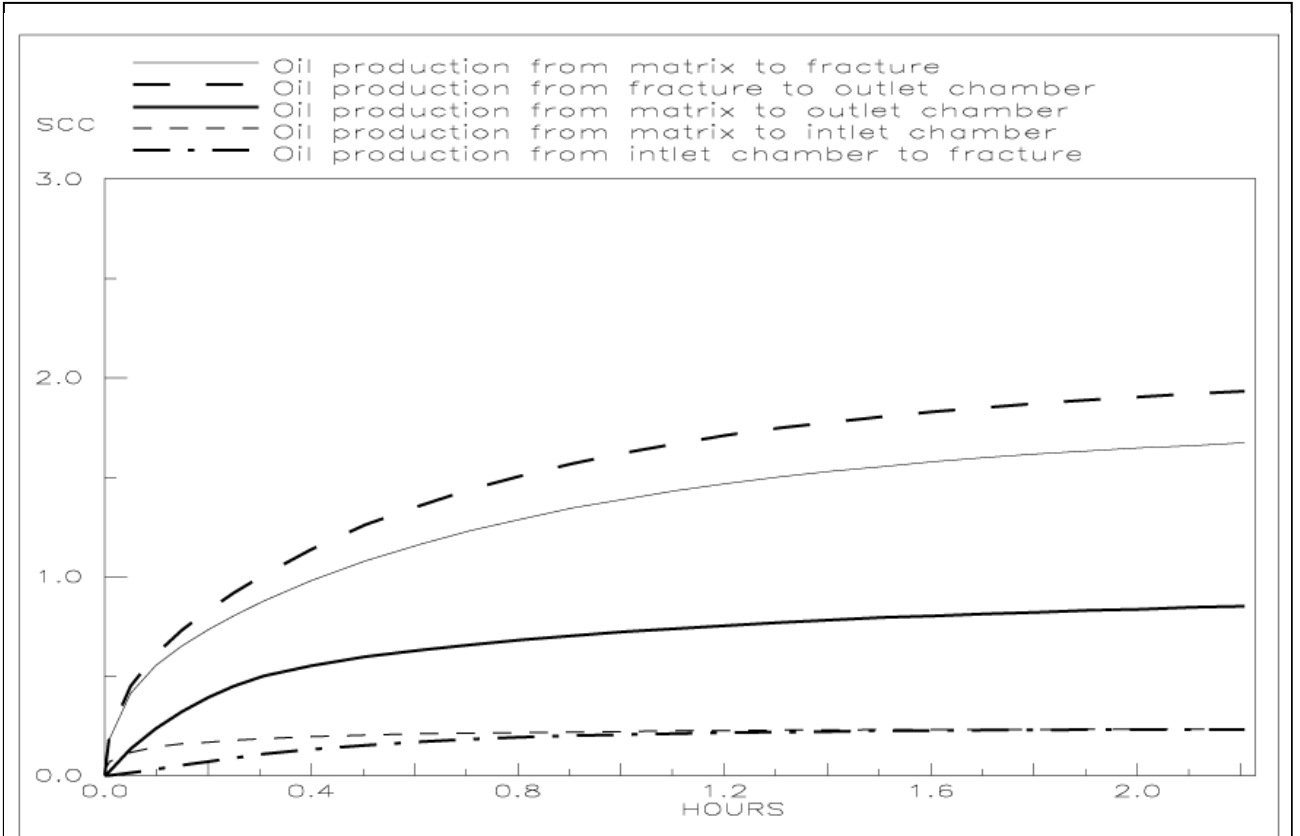water flow patterns
after injection of

Fig. 2.5. Mode of oil production from plug.

1.40 PV. The fracture is located at the top of the model.

Oil and water flow patterns are exemplified in Fig. 2.4 by the situation after injection of 1.40 pore volumes (PV) (The axial length of the inlet chamber is modelled to be 2.5 cm. So in this figure, the plug inlet and outlet are located at axial distances 2.5 and 8.37 cm, respectively).

Production Pattern. The contributions to the cumulative production of oil are given in Fig. 2.5. The results show that about twice as much oil is produced by imbibition to the fracture than by flooding to the outlet chamber.

Saturation Distributions. In Fig. 2.6 are shown an example of the axial saturation distributions of total water (H_2O + D_2O), injection water (H_2O) and formation water (D_2O) after injection of 1.40 PV. It is seen that the D_2O is mobilized and travels as a bank in front of the injected H_2O. The radial profiles in Fig. 2.7 show that the water imbibing from the fracture has a similar effect on the D_2O.

Comparison to Measurements. Measured and calculated saturation profiles after injection of 1.40 PV are compared in Figs. 2.8, 2.9 and 2.10. Fig. 2.8 compares axial profiles, while Figs. 2.9 and 2.10 compares radial profiles.

The axial oil saturation at 0.61 hr effective flooding time is somewhat overpredicted which results in a comparatively underprediction of the D2O saturation. Radial profiles at 0.31 hr compare quite well. The imbibition rate is slightly overpredicted. At 0.61 hr the match of the radial profiles is poorer as the overpredicted imbibition has been effective for a longer period of time. This leads to an overprediction of the water saturation and a resulting underprediction
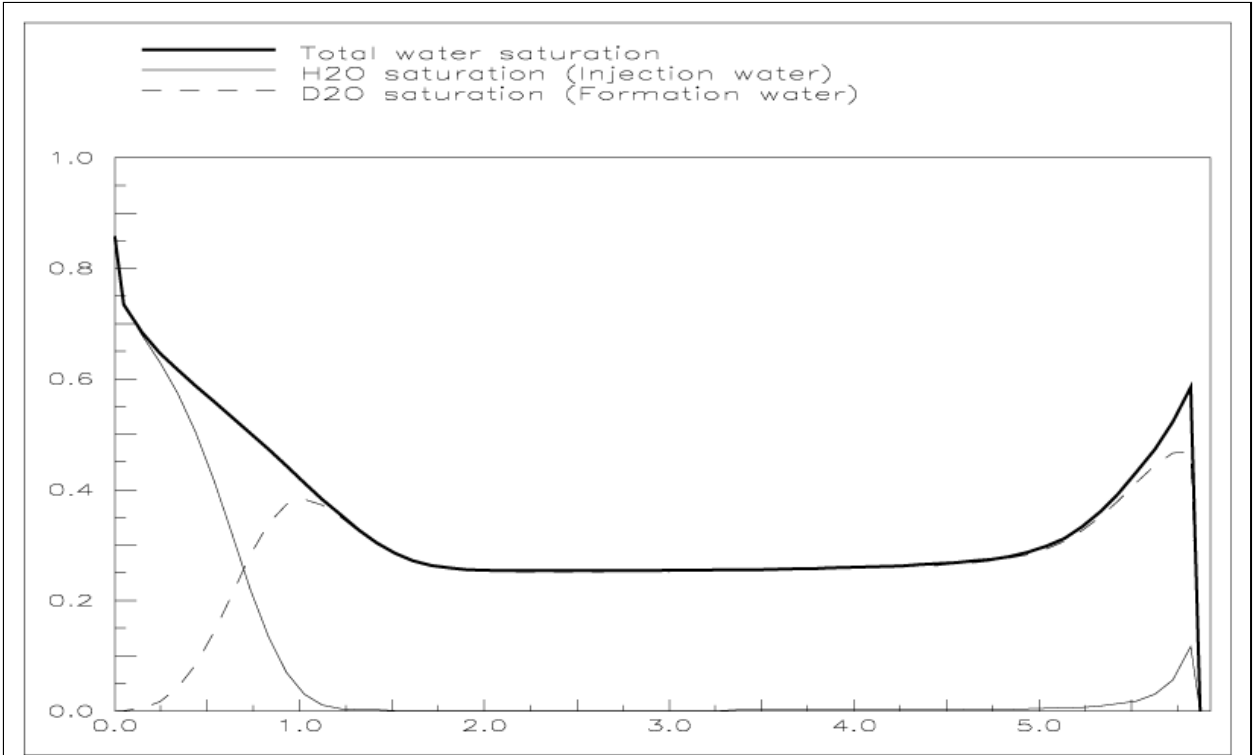
Fig. 2.6. Axial saturation at r=1.16 cm after injection of 1.40 PV.
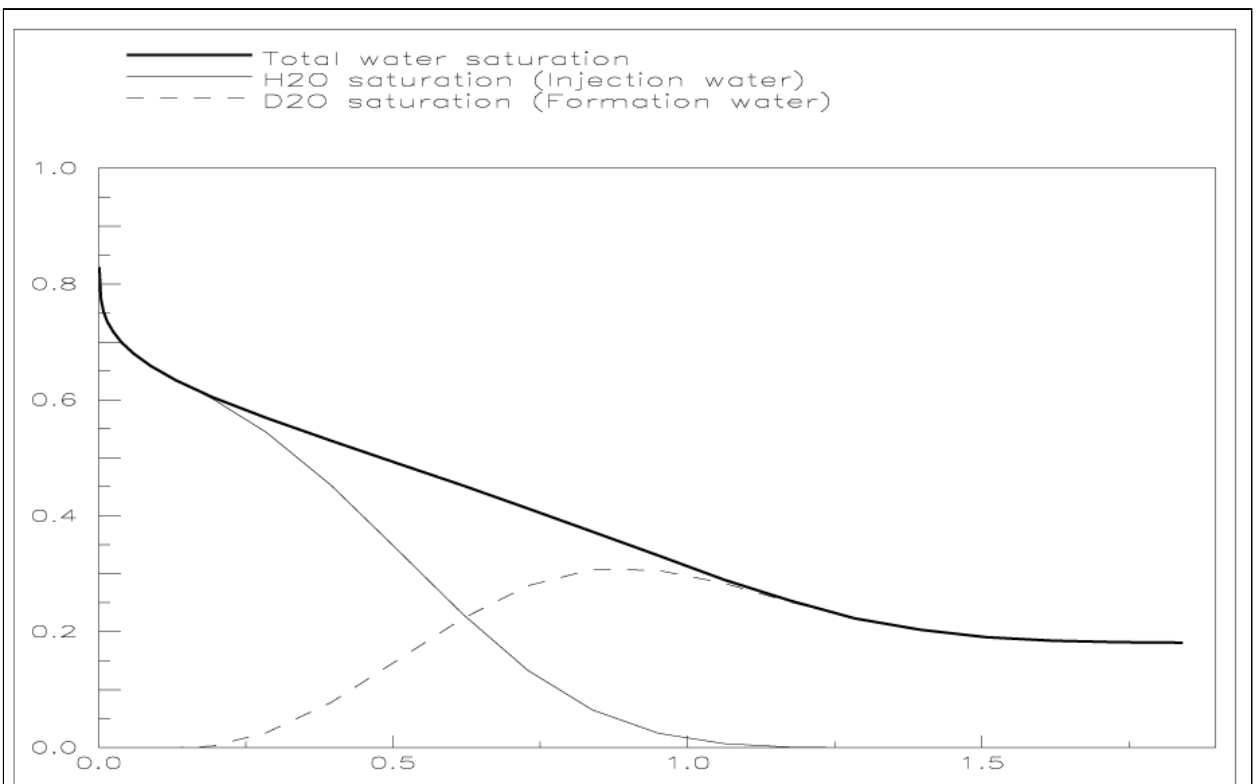

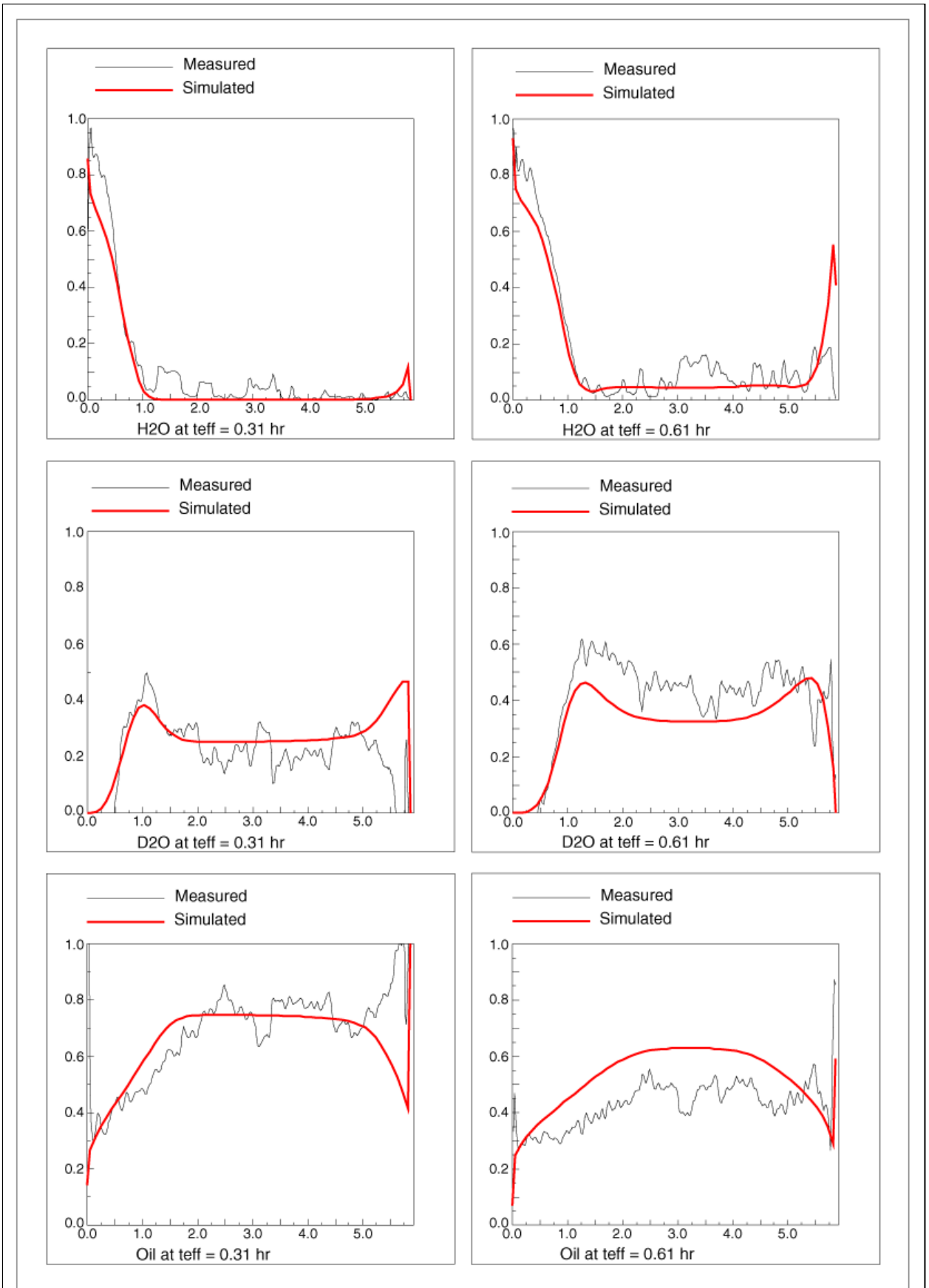**Fig. 2.7.** Radial saturation at x=2.26 cm after injection of 1.40 PV.

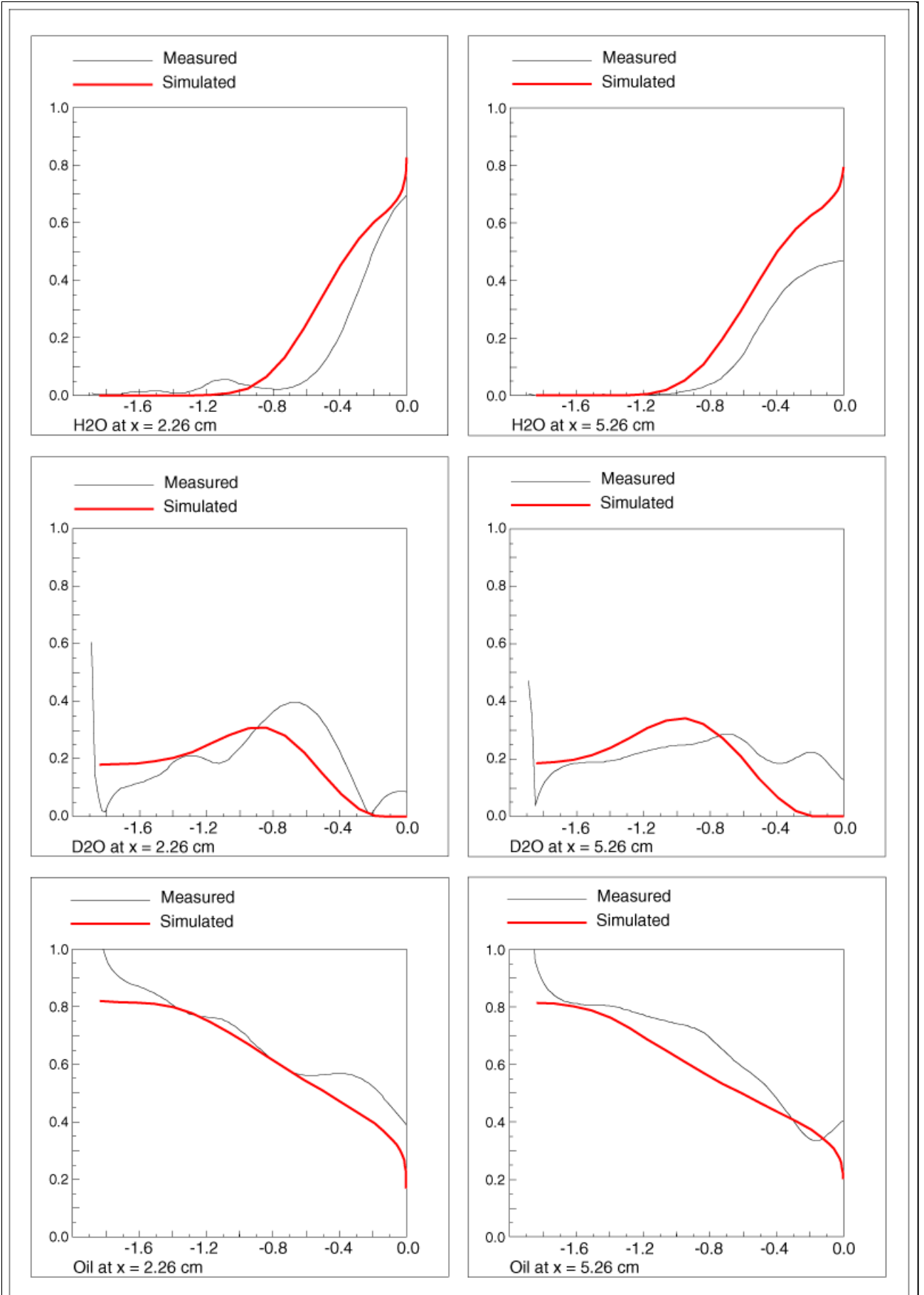**Fig. 2.8.** N36D axial profiles at r = 1.16 cm.
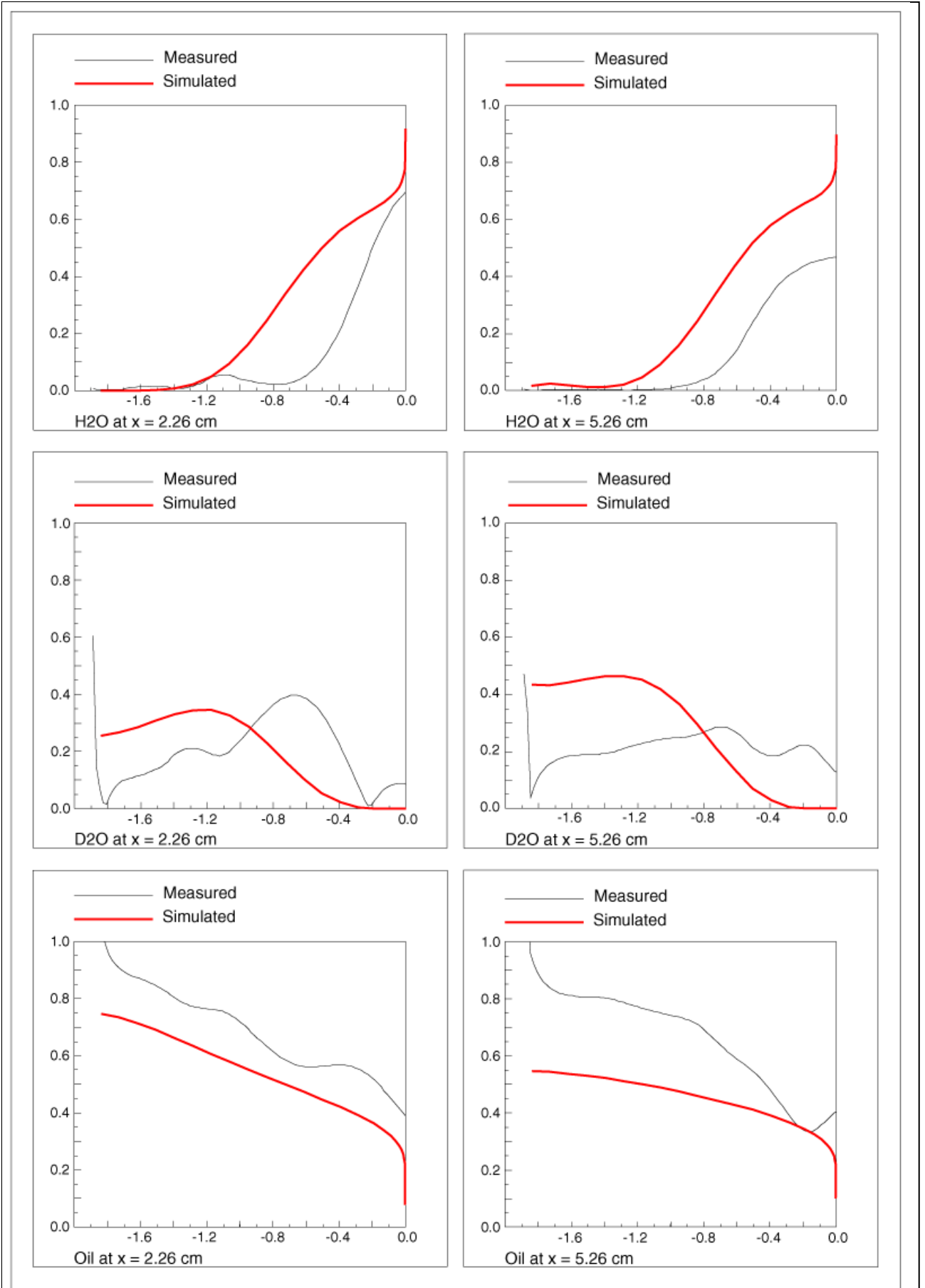
Fig. 2.9. N36D radial profiles at teff = 0.31 hr.
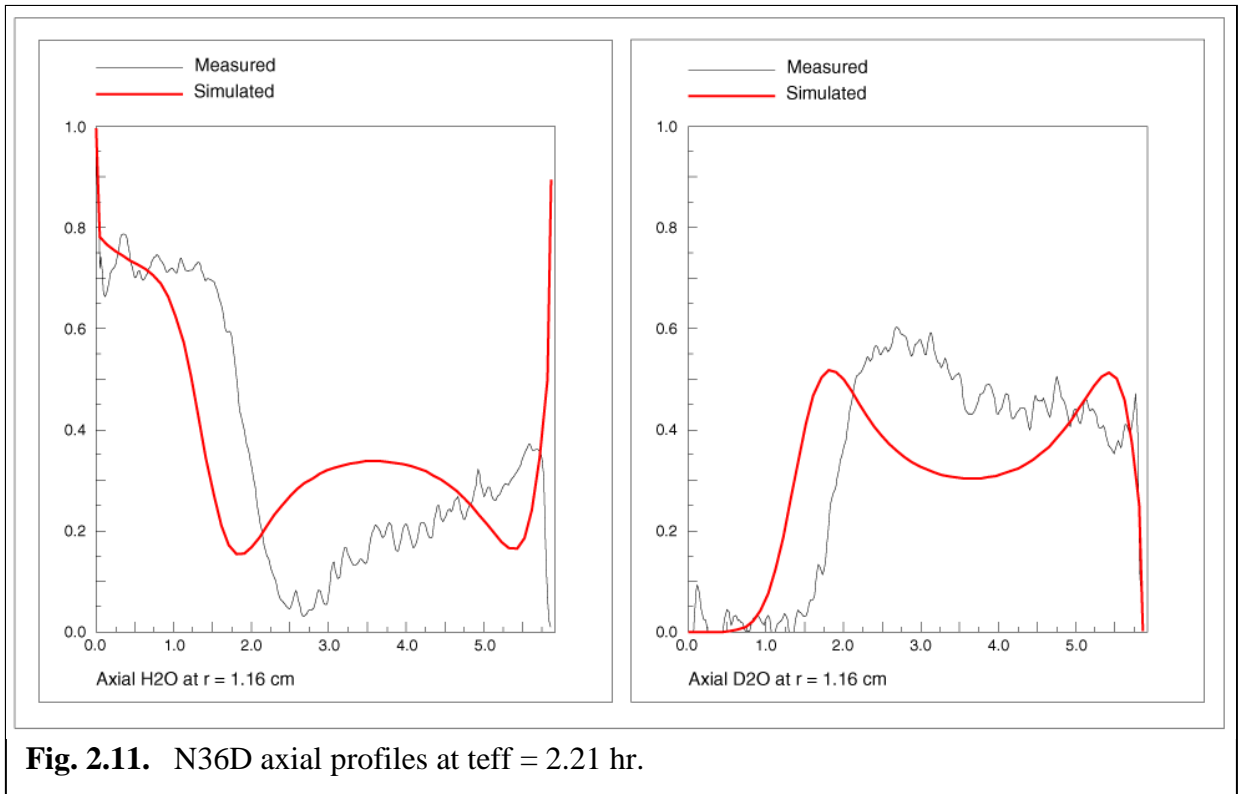
Fig. 2.10. N36D radial profiles at teff = 0.61 hr.

Fig. 2.11. N36D axial profiles at teff = 2.21 hr.

of the oil saturation. The too large amount of imbibed water pushes the D2O further into the plug and away from the fracture than the measurements show.

The calculated increase in water saturation and resulting reduction in oil saturation at the outlet (Figs. 2.6 and 2.8) are not seen in the measurements. The simulated increase in the water saturation is caused by imbibition of water from the outlet chamber. Apparently, this does not happen in the experiment.

Another observation is that the progression of the calculated flood front slows down during the later stage of the experiment relative to what is measured, cf. Fig. 2.11. The reason why this happens is not obvious.

Possible reasons for discrepancies in the simulated results are:

- Judging from the NMR images the plug is obviously not homogeneous. This affects the fluid distributions.
- The assumed uniform initial saturation distribution (27% D2O and 73% oil) deviates from the true initial state.
- The water viscosity used is that of H_2O. The viscosity of D_2O is 23% larger.
- The spontaneous imbibition capillary pressure may be overestimated so that the simulated capillary uptake from the fracture is too fast.
- The relative permeability functions used are determined for co-current flow conditions. However, the major part of the oil is produce by counter-current flow of oil and water. Relative permeabilities are in this situation typically less than the co-current ones (Bourbiaux et al. 1990).

Porous plate experiment on sample M16H1

A comparison of capillary pressure measured by the mercury injection technique, the porous plate technique, and the BON-method is in progress. Because of the extreme time requirement of the porous plate technique to obtain equilibrium on low permeable material the work has not been completed within the present project. The porous plate part of the experiment continues, and is estimated to end in the beginning of 2002. At the time of writing (March 2001) the porous plate experiment has been running for 3.5 year.

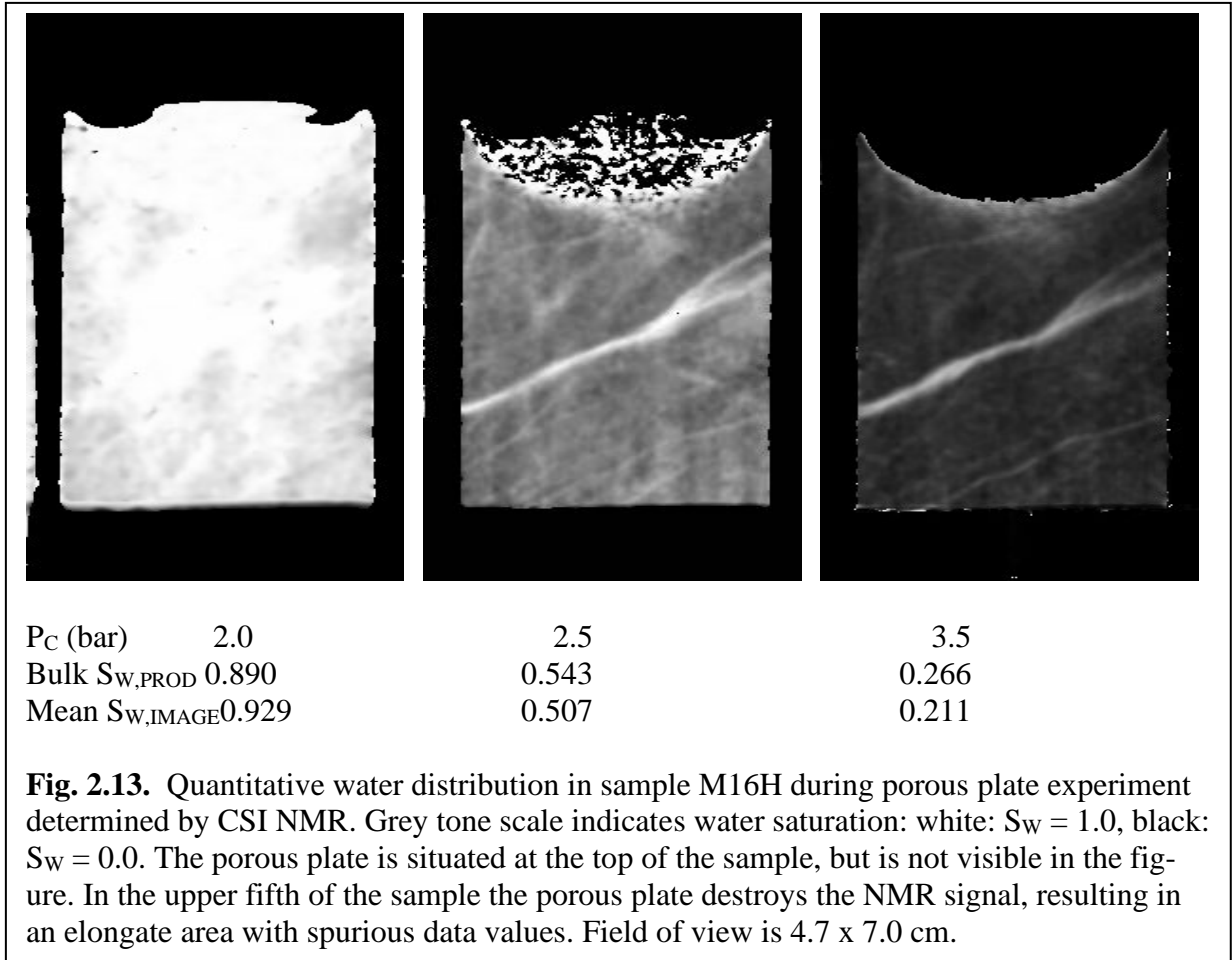Preliminary results are presented in Fig. 2.12. The fluid saturation determinations for the porous plate method may be influenced by evaporation during the long experiment. At the end of the experiment the final fluid saturation will be determined by three independent methods, gravimetry, Dean Stark extraction and NMR spectrometry, and the fluid saturation determinations will be corrected accordingly.

The curve for the mercury injection method of Fig. 2.12 is located at capillary pressures considerably below the curves for the porous plate and BON-methods. Earlier work has shown that capillary pressure curves obtained by mercury injection lie significantly below a curve obtained by the centrifuge method on the same sample of North Sea chalk (Nørgaard et al, 1999, Appendix E). The reason for the mercury injection curves to fall below the three other methods may lie in problems with scaling the interfacial tension and contact angle of the mercury liquid – mercury vapour system to the water – oil system (Anderson, 1987). Alternatively, the discrepancy may be due to failure of the chalk matrix caused by the high injection pressure during the drainage cycle of the mercury injection experiment (Christoffersen, 1992; Bech et al., 2000, Appendix A). The preliminary porous plate capillary pressure curve and the BON-method curve are in fair, but not perfect, agreement (Fig. 2.12). Presently, improved mathematical expressions for the capillary curves of the BON-method are sought (Bech et al.,

Fig. 2.12. Capillary pressure functions for sample M16H

P_C (bar)	2.0	2.5	3.5
Bulk $S_{W,PROD}$	0.890	0.543	0.266
Mean $S_{W,IMAGE}$	0.929	0.507	0.211

Fig. 2.13. Quantitative water distribution in sample M16H during porous plate experiment determined by CSI NMR. Grey tone scale indicates water saturation: white: $S_W = 1.0$, black: $S_W = 0.0$. The porous plate is situated at the top of the sample, but is not visible in the figure. In the upper fifth of the sample the porous plate destroys the NMR signal, resulting in an elongate area with spurious data values. Field of view is 4.7 x 7.0 cm.
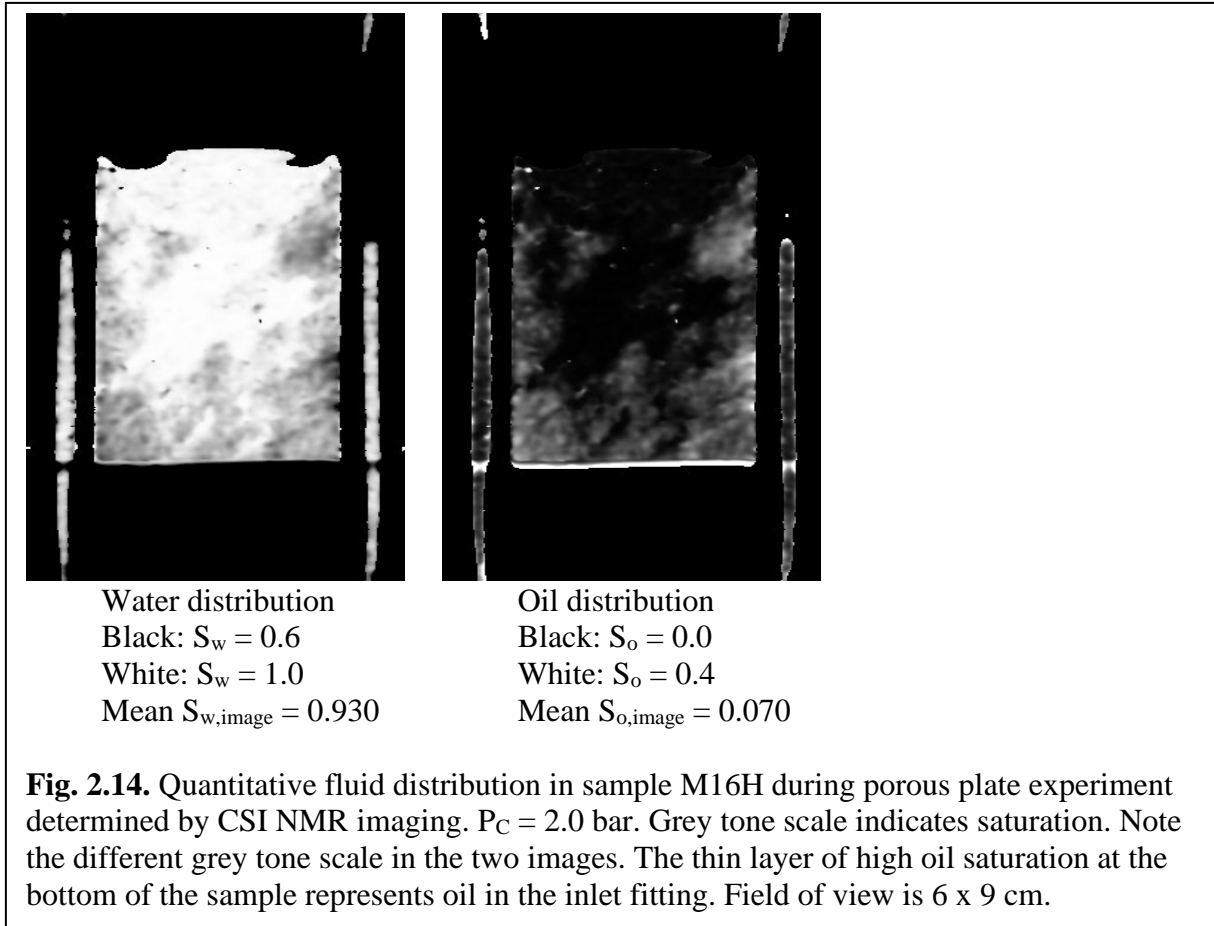
2001, Appendix F), which may improve the agreement.

During the porous plate experiment on sample M16H the fluid distribution inside the sample has been imaged several times by the CSI NMR technique. Fig. 2.13 presents the water distribution at Pc equal to 2.0, 2.5 and 3.5 bar. The sample contained only water and oil, so the oil saturation of each voxel is simply 1-S_w (not shown). The mean fluid saturations of the NMR models are in good agreement with the bulk saturation determined from production (Fig. 2.13). Please notice that the NMR fluid saturation values refer to an image slice of thickness 5 mm, while the bulk saturation values refer to the whole sample volume. Therefore, a perfect agreement is not expected. The NMR saturation models show a distinctly inhomogeneous fluid distribution.

A prominent hairline traverses the sample in an oblique angle with a water saturation level far above the water saturation level of the matrix (Fig. 2.13). Many small hairlines show the same general distribution.

The fluid distribution at $P_C = 2.0$ bar is presented with a grey tone scale of larger contrast in Fig. 2.14. The water saturation model is the same as shown in Fig. 2.13, but the matching oil saturation model has been added to the figure. The threshold pressure of the sample was measured to 1.7 bar, so Fig. 2.14 shows the fluid distribution at a capillary pressure slightly above the threshold pressure. The fluid distribution is strongly inhomogeneous, with a large area in the central part of the sample containing no oil at all. Comparison with Fig. 2.13

Water distribution   Oil distribution
Black: $S_w = 0.6$ Black: $S_o = 0.0$
White: $S_w = 1.0$ White: $S_o = 0.4$
Mean $S_{w,image} = 0.930$ Mean $S_{o,image} = 0.070$

Fig. 2.14. Quantitative fluid distribution in sample M16H during porous plate experiment determined by CSI NMR imaging. $P_C = 2.0$ bar. Grey tone scale indicates saturation. Note the different grey tone scale in the two images. The thin layer of high oil saturation at the bottom of the sample represents oil in the inlet fitting. Field of view is 6 x 9 cm.

shows that this oil-free area is located around the prominent hairline. The hairline clearly has influenced the distribution of oil. However, oil has managed to cross the hairline at several places, e.g. close to the right sample margin, and evidently the hairline has not acted as a complete barrier. The inhomogeneous oil distribution is considered mainly to reflect pore size variations.

The areas of high oil saturation at $P_C = 2.0$ bar are found at $P_C = 2.5$ bar to retain a slightly higher than normal oil saturation, compare Figs. 2.13 and 2.14. The areas with highest oil saturation at $P_C = 2.0$ bar appear close to the right margin of the sample with oil saturations around 0.25 (Fig. 2.14).

Task 3: Description of the flow of oil and water between matrix and fracture in a double-porosity model (GEUS)

A double-porosity model (DPM) of the core plug M16I has been set-up with difference grids of varying fineness. The objective of this work was to investigate to which extent it is possible to reproduce results from the detailed single-porosity description (SPM) and to find out how much faster (or slower) the double-porosity model is. The work has been concentrated on the oil/water system.

It is obvious that a coarser grid leads to a coarser determination of the saturation distributions. Emphasis was put on two requirements:

1. The ultimate oil production and saturation must agree
2. The transient oil production must agree

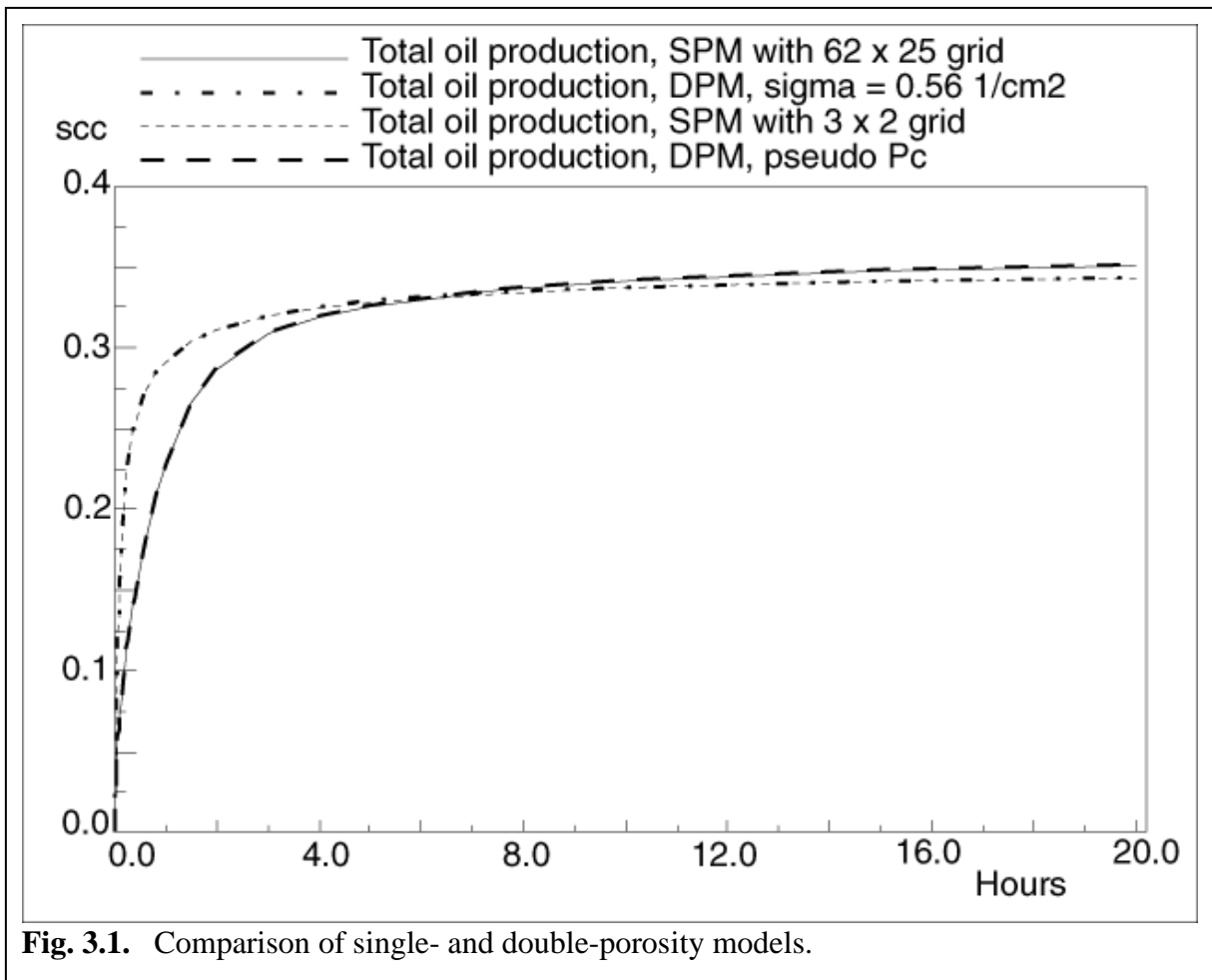Both conditions must be satisfied in the fully submerged as well as in the partially submerged case.

Fig. 3.1.   Comparison of single- and double-porosity models.

The conclusions concerning the double-porosity model are:

By use of measured capillary pressure curves and standard expressions for the geometrical shape factor the following holds:

- Neither requirement 1. nor 2. can be fulfilled
- The ultimate oil production can be made correct in some cases through an adjustment of the point Pc = 0 on the imbibition curve.
- Even for very coarse grids the results are not better than those obtained with the single-porosity model and a similar grid.

The shape factor is a purely geometric parameter. It is therefor not surprising that it cannot describe problems with solutions that are strongly saturation dependent, like the imbibition dominated production of oil from a core plug submerged in water. In Fig. 3.1. two solutions are compared of the total oil production from a cubic matrix block next to a vertical fracture filled with water. (Only one block face is open to flow). The single-porosity reference solution is obtained with a detailed 60 by 25 2D Cartesian grid. In the dual-porosity model the matrix block is described by only one grid cell. The shape factor, σ, is calculated from the standard Kazemi expression

$$\sigma = \frac{2}{L^2}$$

Eq. 3.1

which for the present case with L equal to the radius of plug M16I gives $\sigma = 0.56$ cm^{-2}. The calculated dual-porosity solution has in general two typical characteristics: 1) The production rate is too big initially 2) The ultimate production is too small.
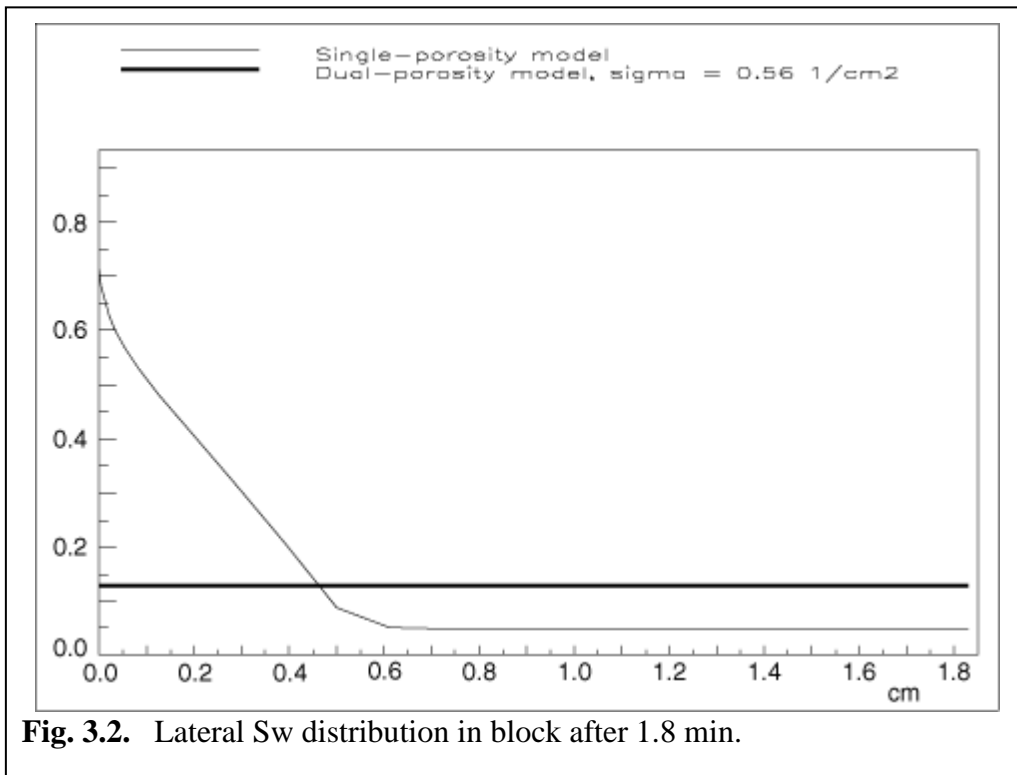

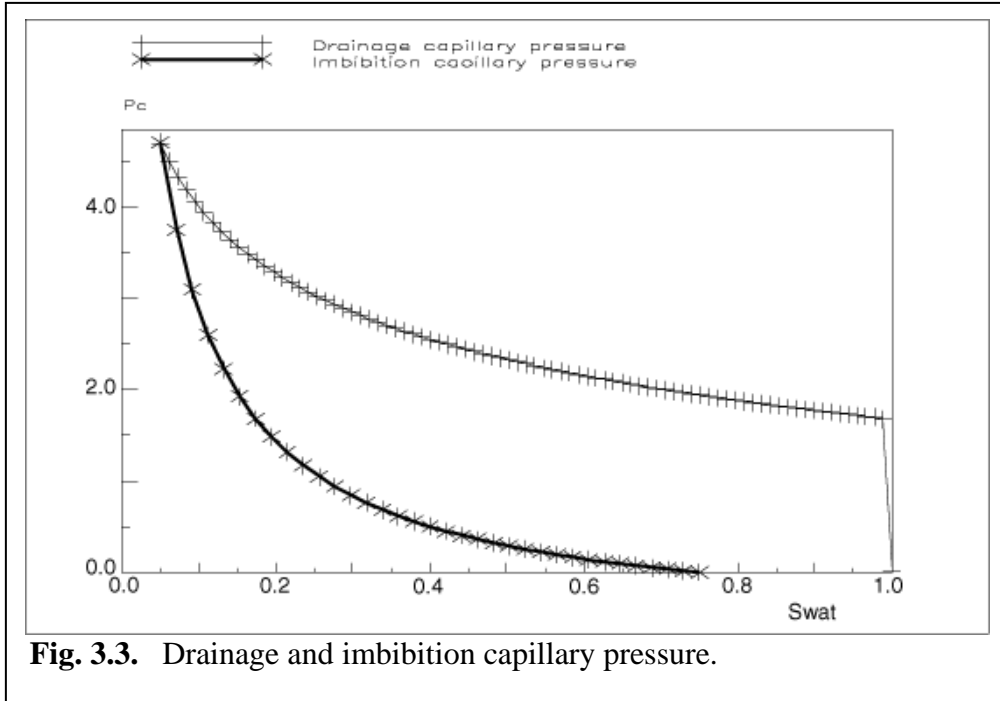**Fig. 3.2.** Lateral Sw distribution in block after 1.8 min.

Fig. 3.3. Drainage and imbition capillary pressure.

When the production is imbibition dominated the rate is proportional to the capillary pressure. In the dual-porosity case the driving capillary pressure is initially large because it is evaluated from the small average saturation in the matrix block, see Figs. 3.2. and 3.3. In the single-porosity model the surface of the matrix block rapidly attains a saturation close to the value corresponding to zero capillary pressure. The driving force is therefor considerably smaller.

In the general case, the ultimate production is underpredicted with the dual-porosity model because the gravitational contribution is not modelled. It is possible in some cases to correct for this through an adjustment of the point Pc = 0 on the imbition curve. The discrepancy shown in Fig. 3.1 has however, different causes as gravitation is not a factor in the 2D x-y case. The reason is that the DPM production rate becomes smaller during the later part of the transient and the approach to the ultimate saturation (Sw = 0.75, cf. Fig. 3.3) is slower.

More accurate expressions than the standard Kazemi have been developed for the shape factor. For example, Lim and Aziz (1995) arrived at the expression

$$\sigma = \frac{4.93}{L^2}$$
Eq. 3.2

In Fig. 3.4 are shown solutions with shape factors ten times larger and ten times smaller, respectively, than the Kazemi shape factor. It is evident, that it is not possible to match the reference solution with a constant shape factor.

The theoretical advantage of the dual-porosity/dual-permeability method relative to the fine-grid, single-porosity method is twofold:

1. It is easier to use, when the fracture density is high
2. It is faster

When the fracture density is not high little if anything is gained by using the DPM in favour of the SPM. In the present test case an equivalent solution is obtained with a 3 by 2 grid cell single-porosity model. The solution of this problem is as fast as the DPM case and the solution obtained is practically identical (Fig. 3.1) The advantage of using the SPM in this situation is that you do not have to bother with any shape factors.

Improved DPM results can be obtained by utilization of pseudo capillary pressure curves. In principle, these are straight forward to calculate from the results of a fine-grid simulation. They do, however, depend upon matrix block sizes as well as saturation functions so the work involved in their determination can be considerable in case of a strongly inhomogeneous reservoir. An additional limitation in relation to use in a commercial simulator such as ECLIPSE is that the matrix pseudo curves in some situations depend on the saturations in both matrix and fracture.

For the case presented here the pseudo capillary pressure is computed as shown below.

Assuming incompressible flow and neglecting gravity we have

$$Q_{o,mf} + Q_{w,mf} = 0 \qquad\qquad \text{Eq. 3.3}$$

$$Q_{o,mf} = KV\sigma\lambda_o(p_{o,m} - p_{o,f}) \qquad\qquad \text{Eq. 3.4}$$

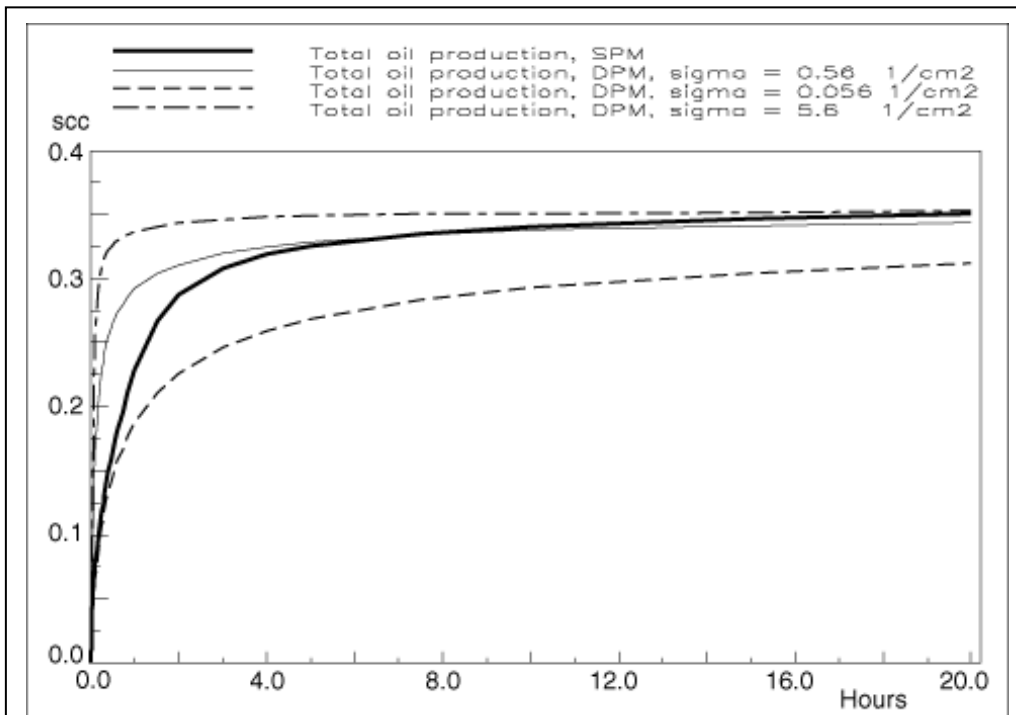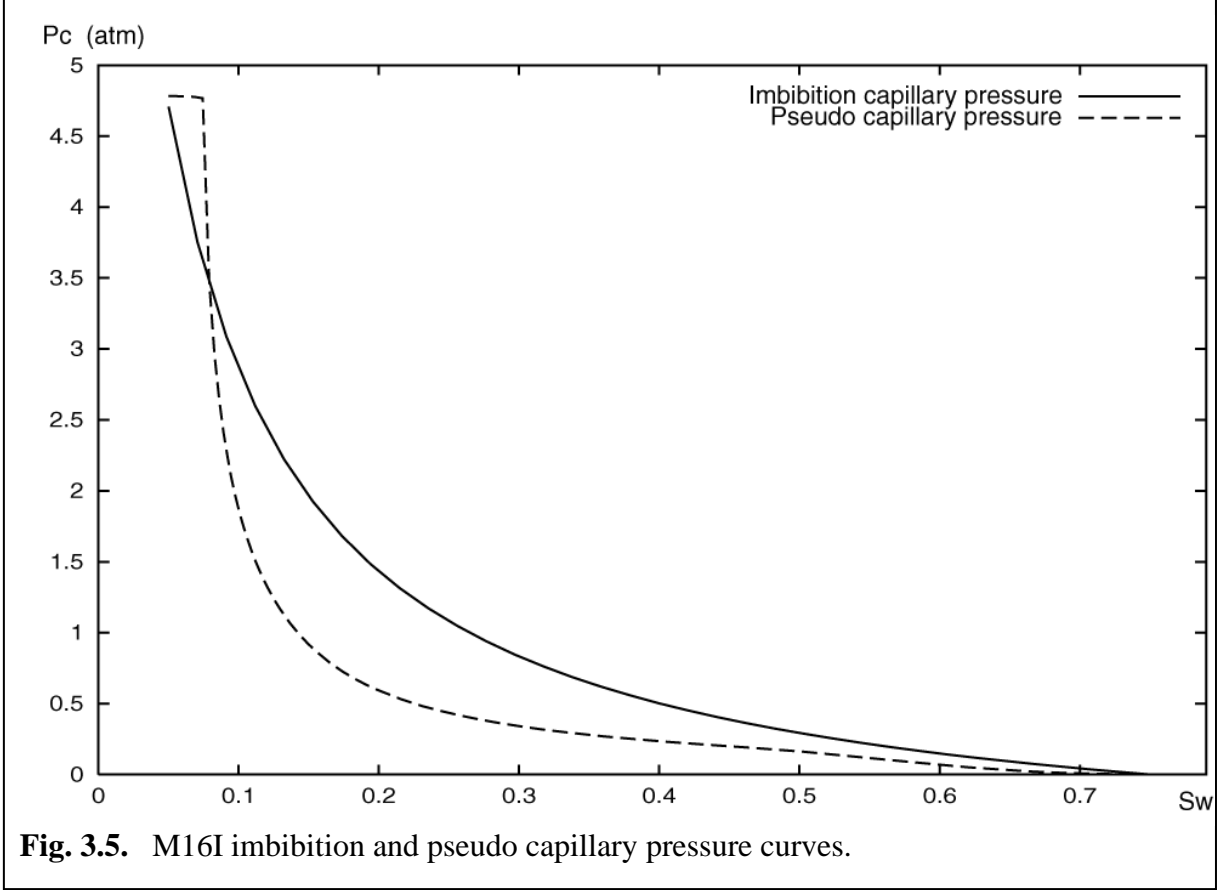$$Q_{w,mf} = KV\sigma\lambda_w(p_{w,m} - p_{w,f}) \qquad\qquad \text{Eq. 3.5}$$

where

Fig. 3.4. Comparison of single- and double-porosity models.

Fig. 3.5. M16I imbibition and pseudo capillary pressure curves.

$$p_c = p_o - p_w \qquad\qquad \text{Eq. 3.6}$$

Eqs. 3.3 – 3.6 give

$$Q_{o,mf} = KV\sigma\bar{\lambda}p_c \qquad\qquad \text{Eq. 3.7}$$

where

$$\bar{\lambda} = \frac{\lambda_o \lambda_w}{\lambda_o + \lambda_w} \qquad\qquad \text{Eq. 3.8}$$

Now, if $Q_{o,mf}$ and the corresponding average matrix block water saturation $\bar{S}_{w,m}$ are calculated from a fine-grid single-porosity simulation the a pseudo-capillary pressure can be calculated from Eq. 3.7, viz.:

$$\hat{p}_c(\bar{S}_{w,m}) = \frac{Q_{o,mf}(\bar{S}_{w,m})}{KV\sigma\bar{\lambda}} \qquad\qquad \text{Eq. 3.9}$$

The calculated pseudo-capillary pressure function is shown in Fig. 3.5 together with the imbibition branch of the matrix capillary pressure curve. The pseudo-capillary pressure is scaled (by means of the average mobility) so that the maximum value matches the maximum of the

matrix curve. The calculated production is compared in Fig. 3.1. to the SPM and standard DPM solutions. It is not possible in the figure to distinguish between the single-porosity solution and the pseudo function solution.

The main conclusion is:

- The single-porosity description should be used whenever it is practically possible. That is, when the density of larger fractures is so small that they can be described individually.
- In all other situations the double-porosity/double permeability model is used with pseudo capillary pressure functions.

Task 4: Development of a method for two-phase up-scaling (COWI)

Part I: Study of water flooding of a fractured system using small-scale simulation models

Displacement mechanisms of water flooding a low permeable fractured system have been examined in detail using small-scale single continuum models (COWI report 42039 Part I (1999), Appendix D). It has been shown that internal fractures, even though connected to the main fracture system, are not flooded before the water saturation in the matrix increases above the spontaneous imbibition end point. In order for this to happen a pressure gradient must be applied over the system.

It has been shown analytically how to derive the matrix and fracture properties: porosity, shape factors and transmissibility factors, in order to describe a specific fracture trajectory in the double continuum formulation. There is good agreement between the simulation results obtained from the single and double continuum models, even in cases where the number of grid cells has been reduced by a factor of 10 in the double continuum formulation.

Part II: Up-scaling of shape factors

Using the results from the small-scale models a fast and easy applicable method for estimation of the magnitude of the shape factors for arbitrary fracture patterns is derived (COWI report 42039 Part II (1999), Appendix D). A specific fracture pattern is sampled on a fine grid and approximated by a large number of straight lines. The applicability of the method is demonstrated by calculating the shape factor for a realistic 2D (100m x 100m) fracture pattern. The method is verified for some simple fracture patterns with varying matrix permeability anisotropy for which analytical expressions for the shape factors exist.

The method is implemented as an add-on module in a 2D general fracture analysis tool. In this tool, specific fracture patterns may be extracted from scanned photos of e.g. outcrops and the up-scaled matrix permeabilities used in the shape factor estimation method are also calculated. The method may also be used for calculation of connection factors for induced fractures to be used as input to reservoir simulation. The method may be extended to 3 dimensions.

Publications

At the time of writing a total of 4 publications have resulted from the project. Two of these are refereed journals articles, and two are non-refereed scientific papers. The latter two papers were also subjects of oral presentations at international conferences. One abstract has been accepted for presentation at the SPE ATCE 2001 conference.

Below the publications, reports, posters and presentations resulting from the project are listed, together with a description of the most important results.

Articles with peer review
Bech, N., Olsen, D. & Nielsen, C.M. "Determination of Oil-Water Saturation Functions of Chalk Core Plugs from Two-Phase Flow Experiments" *(SPE Reservoir Evaluation and Engineering **3**,**1**, p 50-59, 2000)* presents the BON-method, which is based on work by Nielsen et al. (1997), Bech et al. (1998), and Nørgaard et al. (1999). The BON-method was developed by the EFP-96 project ENS J.No. 1313 / 96-0005.

Nørgaard, J.V., Olsen, D., Reffstrup, J. & Springer, N. "Capillary Pressure Curves for Low Permeability Chalk Obtained by Nuclear Magnetic Resonance Imaging of Core Saturation Profiles" *SPE Reservoir Evaluation and Engineering **2**,**2**, p 141-148, 1999.* This article is a revised version of SPE paper 30605 (1995) presenting an earlier approach to calculating saturation functions from displacement experiment data.

Conference papers without review
Olsen, D., Nielsen, C.M. & Bech, N. "Variation in Fracture Permeability in Chalk Core Plugs" *(SPE paper 60302 ,13 pp, 2000)* presented at *SPE Rocky Mountain Regional/Low Permeability Reservoirs Symposium, Denver, Colorado, 12-15 March 2000.* This paper concerns a miscible H_2O – D_2O displacement experiment. It is shown that a fracture in as sample of chalk has a large variation in absolute permeability along the length of a sample.

Nielsen, C.M., Olsen, D. & Bech, N. "Imbibition Processes in Fractured Chalk Core Plugs with Connate Water Mobilization" *(SPE paper 63226, 10 pp, 2000)* presented at *SPE Annual Technical Conference and Exhibition, Dallas, Texas, 1-4 October 2000.* This paper concerns an immiscible H_2O – D_2O - oil displacement experiment. It is shown that injection water has limited contact with the oil that is produced during a waterflood. It is further shown that a significant part of the connate water travels ahead of the injection water as a bank.

Report
COWI "Flow in Fractured Chalk" *COWI report no. 42039/D1,D2, October 1999*, pp 36. Part 1 analyses waterflooding processes in small-scale single continuum and double continuum models, and evaluates the performance of the double continuum model. Part 2 presents a method for estimating shape factors for simple fracture patterns.

Poster

Bech, N., Olsen, D. & Nielsen, C.M. "Determination of Oil/Water Drainage and Imbibition Saturation Functions of Chalk Core Plugs from Flooding Experiments" presented as a poster at *SPE Applied Technology Workshop "Field Management of Maturing Reservoirs", Scheveningen, Netherlands, 5-8 June 2000.* The poster gives a summary of the BON-method (Bech et al., 2000).

Abstract accepted for presentation

Bech, N., Olsen, D. & Nielsen, C.M. "Improved Determination of Oil/Water Drainage and Imbibition Saturation Functions of Chalk Core Plugs From Flooding Experiments". Abstract accepted for presentation at *SPE Annual Technical Conference and Exhibition 30 September-3 October 2001, New Orleans, Louisiana.* The paper will present improvements to the BON-method. The most important improvement is more realistic and flexible mathematical expressions of the saturation functions.

Oral presentation

Nielsen, C.M., Olsen, D. & Bech, N. "Imbibition Processes in Fractured Chalk Core Plugs with Connate Water Mobilization". Presented at *SPE Copenhagen Section meeting 25 February 2001.* Contents as Nielsen et al. (2000).

Nomenclature

a	=	fracture aperture
A	=	flow area
C	=	compressibility
D	=	diameter
K	=	absolute permeability
L	=	length of plug
n	=	number of grid cells
p	=	pressure
Δp	=	pressure drop
$\hat{p}_c$	=	pseudo capillary pressure
Q	=	volume flow rate
r	=	plug radius
S	=	saturation
$\bar{S}$	=	average saturation
V	=	Volume
Δx	=	x-direction grid length
Δy	=	y-direction grid length
Δz	=	z-direction grid length
φ	=	porosity
λ	=	mobility
$\bar{\lambda}$	=	average mobility
μ	=	viscosity
σ	=	shape factor

Subscripts

av	=	average
c	=	capillary
eff	=	effective (two-phase) permeability
f	=	fracture
i	=	x-direction coordinate index
m	=	matrix
o	=	oil
$plug$	=	core plug
$rock$	=	matrix rock
T	=	total
x	=	refers to x-direction
y	=	refers to y-direction
z	=	refers to z-direction
w	=	water

References

Anderson, W.G. (1987); "Wettability Literature Survey – Part 4: Effects of Wettability on Capillary Pressure"; *J. Petroleum Technology 30, p 1283-1300, October 1987.*

Bech, N.; Olsen, D.; Nielsen, C.M. (2000); "Determination of Oil-Water Saturation Functions of Chalk Core Plugs from Two-Phase Flow Experiments"; *SPE Reservoir Evaluation and Engineering 3,1, p 50-59, 2000*

Bech, N.; Olsen, D. & Nielsen, C.M. (1998); "Determination of Oil/Water Saturation Functions of Chalk Core Plugs From Two-Phase Flow Experiments"; *SPE paper 49325, 1998.*

Bourbiaux, B.J. & Kalaydjian, F.J. (1990); "Experimental Study of Cocurrent and Countercurrent Flows in Natural Porous Media"; *SPE Reservoir Engineering August 1990, p 361-368, 1990.*

Christoffersen, K.R. (1992); "High-Pressure Experiments With Application to Naturally Fractured Chalk Reservoirs, 1. Constant Volume Diffusion, 2. Gas-Oil Capillary Pressure", *Ph.D. dissertation, University of Trondheim, 214 pp, 1992.*

COWI (1999); "Flow in Fractured Chalk"; COWI report no. 42039/D1,D2, October 1999, *pp 36.*

Lim, K.T. & Aziz, K. (1995); "Matrix-fracture transfer shape factors for dual-porosity simulators*"; J. Pet. Sci. Eng., 13, p 169-178, 1995.*

Nielsen, C.M.; Olsen, D.; Bech, N. (2000); "Imbibition Processes in Fractured Chalk Core Plugs with Connate Water Mobilization"; *SPE paper 63226 presented at the SPE Annual Technical Conference and Exhibition 1-4 October 2000, Dallas, Texas, 10 pp, 2000.*

Nielsen, C.M.; Larsen, J.K.; Bech, N.; Reffstrup, J.; Olsen, D. (1997); "Determination of Saturation Functions of Tight Core Samples Based on Measured Saturation Profiles"; *SCA paper 9721, 1997.*

Nørgaard, J.V.; Olsen, D.; Reffstrup, J.; Springer, N. (1999); "Capillary Pressure Curves for Low Permeability Chalk Obtained by Nuclear Magnetic Resonance Imaging of Core Saturation Profiles"; *SPE Reservoir Evaluation and Engineering 2,2, p 141-148, 1999.*

Olsen, D.; Nielsen, C.M.; Bech, N. (2000); "Variation in Fracture Permeability in Chalk Core Plugs", *SPE paper 60302 presented at the SPE Rocky Mountain Regional/Low Permeability Reservoirs Symposium 12-15 March 2000, Denver, Colorado, 13 pp, 2000.*

Appendix A

Bech, Olsen & Nielsen, *SPE Reservoir Evaluation and Engineering 3,1, p 50-59, 2000.*

Determination of Oil/Water Saturation Functions of Chalk Core Plugs From Two-Phase Flow Experiments

Niels Bech, SPE, Dan Olsen, SPE, and C.M. Nielsen, Geological Survey of Denmark and Greenland (GEUS)

Summary

A new procedure for obtaining oil/water saturation functions, i.e., capillary pressure and relative permeability, of tight core samples uses the pronounced end effect present in flooding experiments on such material. In core material with high capillary pressure, the end effect may allow determination of the saturation functions for a broad saturation interval. A complex coreflooding scheme provides the fluid distributions and production data from which the saturation functions are computed for both drainage and imbibition by a least-squares technique. A chemical shift NMR technique is used for fluid distribution determination. An undesirable interdependency of the saturation functions is avoided by their calculation from different data sets. Killough's method is employed to account for the scanning effect in hysteresis situations for both capillary pressure and relative permeability. The procedure is demonstrated on chalk samples from the North Sea. The experimental time is intermediate between the centrifuge and porous plate methods.

Introduction

Petrophysical parameters are an integrated part of every simulation study concerning displacement processes in porous media. A prerequisite for meaningful modeling is reliable petrophysical data. Simulations and models rapidly evolve in the direction of more details and greater precision, and the underlying petrophysical data should evolve accordingly. Several workers have presented methods utilizing coreflooding techniques in combination with computer simulations to determine saturation functions of rock samples.[1-9] The aim of the present work is to develop an experimental method, which is particularly suitable for determination of the oil/water capillary pressure and relative permeability for samples of chalk for both drainage and imbibition. Inherently, chalk has high capillary pressure, and laboratory determinations of saturation functions on such material are complicated by strong scale effects, particularly by the capillary end effect. This capillary retention of the wetting phase in displacement experiments results in a saturation gradient through the core sample. Although being a problem in many traditional core analyses, the end effect actually contains detailed information about the saturation functions of the sample, and can cover a large saturation interval. The idea of the work is to make use of this information to calculate relative permeability functions and capillary pressure curves.

Conventional methods for determination of saturation functions are mainly developed for rocks of lower capillary pressure and higher mechanical strength than chalk, and their application to chalk may be questionable. The mercury injection method for capillary pressure determination uses a fluid system with wetting characteristics and surface tension much different from the oil/water fluid system of an oil reservoir. The centrifuge method for determination of capillary pressure is largely unsuitable due to the low mechanical strength of chalk, as well as the difficulty of obtaining the necessary high rotational speed. In addition, no general agreement exists on the flow equations for deriving capillary pressure from centrifuge data.[10-13] The porous plate method for determination of capillary pressure appears to be valid, but is extremely time consuming for low permeability materials. The steady-state and unsteady-state methods for determination of relative permeability are experimentally viable, but must be coupled to computational procedures to account for the saturation gradients caused by capillary pressure. Classical Buckley-Leverett theory does not account for capillary pressure.

The method to be presented is based on a parameter estimation technique, utilizing saturation data obtained from a complex experimental coreflooding procedure developed by Nielsen et al.[14] It uses the prominent end effect that is caused by the strong capillary forces of rocks with low permeability and allows calculation of both drainage and imbibition saturation functions. The method assumes capillary continuity of the fluid phases, and homogeneity of the sample with respect to the saturation functions.

Experimental Technique

The method depends on experimental data on the distribution of fluids during flooding experiments. A one-dimensional (1D) nuclear magnetic resonance (NMR) imaging technique is used for quantification of the fluid distribution.[15] This technique is restricted to rocks with NMR spin-spin relaxation constants above approximately 6 ms, encompassing many types of limestone, but excluding nearly all types of sandstone. Fortunately, the computational method is not dependent on a specific technique for quantifying the fluid distribution. Gamma-ray attenuation,[16] x-ray computerized tomography (CT) scanning,[3,17] or microwave scanning techniques,[18] may be suitable.

Sample Material. The material used in the experimental work is chalk of Maastrichtian age from the Dan field in the Danish sector of the North Sea known to comply with the NMR requirements.[15] Results are presented for two samples. Both are cylindrical 38 mm plug samples, drilled with the cylinder axis parallel to any visible bedding or layering, to minimize effects of sample inhomogeneity on the flooding experiments. 1D signal intensity profiles indicate that samples M113 and M16H are homogeneous within experimental scatter, while two-dimensional (2D) spin-echo images reveal the presence of minor hairlines. The samples were cleaned by Soxhlet extraction with methanol and toluene prior to the flooding experiments. The samples are strongly water-wet. Basic parameters for the samples are given in **Table 1**.

Fluid Data. A synthetic formation brine with a salinity of 7% was used. The brine is similar in composition to formation water from the Dan field. N-decane was used as the nonwetting oil phase. A prerequisite for the parameter estimation technique and the NMR measurements is that the fluid system can be described as a two-phase system. It is thus essential to avoid the presence of a free-gas phase. This was accomplished by degassing of all fluids.

Flooding Experiments. Information for calculation of both drainage and imbibition capillary pressure functions, as well as drainage and imbibition relative permeability functions is obtained from a complex coreflooding procedure. The procedure consists of a sequence of five flooding experiments as follows:

- Step 1: Threshold pressure experiment.
- Step 2: Transient flow drainage experiment.
- Step 3: Stationary flow drainage experiment.
- Step 4: Stationary flow internal imbibition experiment.
- Step 5: Forced flow imbibition experiment.

1094-6470/2000/3(1)/50/10/$3.50+0.15

TABLE 1–NMR PARAMETERS

Sample (ID)	M113	M16H
T_1 (ms)		500
T_2 (ms)		10.6
NMR profile length (mm)	90	90
NMR profile resolution (mm/pixel)	0.35	0.35
NMR profile acquisition time (hour)	6	9
NMR frequency window for integration (Hz)	500	500
t_r (s)	6.0	9.0
No. of t_e value	7	7
Minimum t_e value (ms)	2.5	2.5
Duration of rf pulses (ms)	0.1	0.1
$\rho_{p,w}$	0.9759	0.9759
$\rho_{p,o}$	1.0185	1.085
Reproducibility (1 s.d.) (p.u.)	2	2
Accuracy (pixel saturation) (p.u.)	5	5
Accuracy (bulk saturation) (p.u.)	2	2

Fig. 1–Measured saturation profiles for sample M113.

The steady-state situation at the end of a primary drainage experiment allows calculation of the drainage capillary pressure and the drainage oil relative permeability. The water relative permeability is calculated from the unsteady-state data obtained during the transient part of this experiment. After a flow reversal, a new end effect develops at the opposite end of the core by an internal imbibition process, which at steady state allows calculation of the spontaneous imbibition capillary pressure and the imbibition oil relative permeability. Following a change from oilflooding to waterflooding, the forced imbibition capillary pressure is calculated from transient pressure drop measurements.

A nonmagnetic Hassler-type core holder connected to a Mobile Flooding Unit[19] is used to allow NMR measurement during the experimental steps while sustaining fluid flow through the sample.

Step 1: Threshold Pressure Experiment. The sample is saturated with brine, and a drainage experiment is set up with a very slow linear upramping of the inlet oil pressure, while displaced fluid volume is recorded. A plot of the inlet oil pressure vs displaced fluid volume shows a distinct break at the point when the oil phase enters the sample. The inlet pressure at this point is the threshold pressure p_{th}.

Step 2: Transient Flow Drainage Experiment. After the threshold pressure experiment, the sample is cleaned and resaturated with brine. Then, a transient flow drainage experiment is conducted at constant rate q_o with monitoring of fluid production and $\Delta p_{o,T}$ as a function of time. The data are used for calculation of the drainage relative permeability to water, k_{rw}^{dr}. This experiment is similar to a conventional unsteady-state Buckley-Leverett experiment, but the use of the resulting data set is different.

Step 3: Stationary Flow Drainage Experiment. During the transient flow drainage experiment the flow is sustained at controlled temperature and flow rate until a stable $\Delta p_{o,T}$ is obtained, and until water production has ceased. At steady state, a stable fluid saturation gradient is present in the sample (see, e.g., **Fig. 1**), and the stationary flow drainage experiment is conducted, with monitoring of the S_w profile. The data set is used for calculation of k_{ro}^{dr} and p_c^{dr}. The fluid saturation profile is measured by NMR.

Step 4: Stationary Flow Internal Imbibition Experiment. The oil flow direction is now reversed and the water contained in the end effect is displaced through the sample towards the former inlet, where a new end effect evolves due to the capillary retention of the water. By this flow reversal one part of the sample undergoes a drainage process and another an imbibition process. The buildup of the new end effect follows a spontaneous imbibition process because the oil pressure is higher than the water pressure during the displacing of the end effect. The flow rate must be large enough to create a water production from the sample. If the flow rate is insufficient to cause water production, the water saturation measured in the downstream part of the sample may be controlled by the availability of water rather than by the bounding
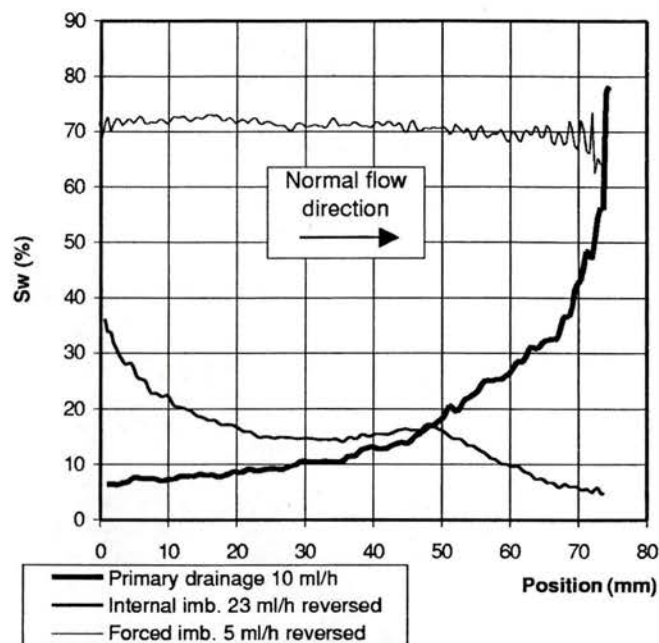
imbibition capillary pressure curve of the sample, leading to erroneous calculation of $p_{c,spt}^{imb}$ and dependent parameters. The stationary flow internal imbibition data set is measured, when $\Delta p_{o,T}$ is stable, and water production has ceased (see, e.g., Fig. 1). Again, NMR is used to monitor the S_w profile. The data are used for calculation of k_{ro}^{imb} and k_{ro}^{imb}, together with the capillary pressure scanning parameter ϵ.

Step 5: Forced Flow Imbibition Experiment. In the last experiment step, a forced imbibition process is produced in the sample by flooding the sample with brine. During the transient flooding period $\Delta p_{w,T}$, as a function of time, is measured. When a static flow situation is reached, NMR is used to monitor the water saturation profile from which the value of irreducible oil saturation is determined (see, e.g., Fig. 1). The data set is used to calculate $p_{c,\text{forced}}^{imb}$.

NMR Measurements

Hardware. A 4.7 T SISCO experimental NMR scanner is used for the NMR work. It is equipped with a 130-mm-diam insert gradient set, capable of producing magnetic gradient up to 100 mT/m along any of three orthogonal directions. The gradient rise rate is 2×10^5 mT/m·s. A radio-frequency (rf) coil of a slotted tube resonator design is used. It has a good signal homogeneity until a maximum length of 90 mm.

Pulse Sequence. The objective of the NMR measurements is to obtain fluid saturation information, that is spatially resolved along the direction of fluid flow through a sample. This is accomplished by using a one-dimensional chemical shift pulse sequence named TST.[15] Assuming homogeneity of the sample, the flooding experiments are essentially 1D experiments, and the use of a 1D pulse sequence is appropriate.

In the investigated samples the contents of paramagnetic and ferromagnetic minerals are low, and the main magnetic field B_0, has good homogeneity across the sample. The linewidth of the oil and water resonances lies between 100 and 200 Hz full width at half maximum (FWHM), with the two resonances separated by 700 to 800 Hz. Mutual interference between the two resonances is below 5% of the total signal intensity. The interference is significantly compensated by an interference correction procedure using interference factors determined on single-fluid profiles, where mutual interference is absent.

Data Processing. A data set from the *TST* pulse sequence represents a stack of spectra at consecutive spatial positions. The following data processing steps are necessary to transform this 2D data set to a quantitative 1D saturation profile:

- Step 1: Frequency dimension elimination.
- Step 2: Relaxation correction.
- Step 3: Proton density correction.
- Step 4: Calculation of saturation.

The saturation profiles have 256 pixels (data values) and are, typically, 90 mm long. The time requirement for a high-quality saturation profile is approximately 2 hours. Compliance with t_r (repetition time), resolution, number of values for t_e (echo time), phase cycling, and spatial resolution may bring the acquisition time for a saturation profile down to 5 minutes, and still retain a fair signal-to-noise ratio. Readers interested in the NMR data processing procedure are referred to Olsen et al.[15]

Relaxation Correction. The effect of spin-lattice relaxation is eliminated by selecting t_r at least five times as long as the longest T_1 component of the sample. With this convention, it is assured that the error on signal intensity due to differential saturation of the NMR signals is less than 1% of the detected signals.

Spin-spin relaxation of an inhomogeneous system is a complex process, which in principle follows a multiexponential behavior according to

$$M(t) = M(t=0) \int P(a) \exp[-t/T_2(a)] \, da, \qquad (1)$$

where $M(t)$ is the magnetization at time t, $P(a)$ is the volume probability density function for pore size a, and $T_2(a)$ is the spin-spin relaxation constant for pores of size a.[20]

The spin-spin relaxation of a sample is compensated by a relaxation modeling on an array of data sets.[9,21-24] The array of data sets is acquired, with identical acquisition parameters, except for different values of t_e. A spin–spin relaxation modeling is then performed for each pixel array, producing 1D data sets of the fitted parameters, which include the magnetization at time zero, $M(t=0)$. The t_e values of the setup are selected for optimal definition of the relaxation. Downwards, the setting of t_e is restricted by system hardware constraints. Slightly dependent on the setup, the smallest possible t_e value, $t_{e,\min}$, is 2.5 ms for the *TST* pulse sequence. The smallest t_e value is usually selected to be close to $t_{e,\min}$, in order to trace the relaxation path as close to the $M(t=0)$ condition as possible. The largest t_e value in a t_e array is usually selected to be approximately three times the anticipated single-exponential T_2 relaxation constant, at which time the magnetization $M(t)$ has declined to 5% of the $M(t=0)$ value.

An important issue is the choice of spin-spin relaxation model. Single-exponential, biexponential, and stretched-exponential models were tested by Kim et al.,[25] while Kenyon et al.[26] tested biexponential, triexponential, and stretched-exponential modeling. The conclusion of Kim et al. is that biexponential fitting is preferable, while Kenyon et al. find that stretched-exponential fitting is preferable. Working on chalk samples, Olsen[15] finds that $M(t=0)$ in chalk is confidently determined by single-exponential fitting. In the present project single-exponential modeling is used, i.e.,

$$M(t) = M(t=0) \exp(-t/T_2) + E, \qquad (2)$$

where E is the signal level (noise) at $t=\infty$. For nearly all pixels the extrapolation of the fit from $M(t=t_{e,\min})$ to $M(t=0)$ is short, because the ratio $M(t=t_{e,\min})/M(t=0)$ is above 0.5. For a large majority of pixels modeling by Eq. 2 results in good precision for the estimation of $M(t=0)$. Failure to produce good fits mainly occurs at the ends of a sample, where susceptibility contrasts destroy the homogeneity of the magnetic field. These inferior fits cannot be improved by choosing another relaxation model. The validity of the single-exponential model is confirmed by good agreement [around 2 percentage units (p.u.)] between bulk saturation determinations by integration of NMR profiles and conventional methods (Dean-Stark extraction and gravimetric determination).

The success of the single-exponential model may be explained by low surface relaxivity caused by the high static magnetic field[27] and low contents of paramagnetic material,[28] which creates approximately single-exponential relaxation by fulfilling the conditions of the fast-diffusion regime.[29,30] The condition may be enhanced by an environment with relatively homogeneous pore structure.

Limitations and Accuracy of the NMR Method. Spin-spin relaxation and resolution of the NMR resonances restrict the choice of samples suitable for NMR saturation profile measurement. The samples in this work have T_2 values around 10 ms and good resolution of the NMR resonances. Comparison of the mean saturations of saturation profiles with conventional bulk saturation determinations indicates an accuracy for the NMR method of 2 p.u. on the mean saturations.[15] The accuracy of the pixel saturations is inferior, probably around 5 p.u., but dependent on the setup. The reproducibility of the pixel saturations is 2 p.u., as estimated from replicate analyses and saturation profile smoothness.

Parameter Estimation Technique

The experimental data used for the determination of the saturation functions, are the pressure data and saturation profiles obtained from the complex flooding procedure. The saturation functions are determined as analytical functions of the saturation.

The flooding experiments are divided into a drainage case and two imbibition cases. Inlet flow rates are constant within each case. The flow directions of the two imbibition cases are reversed relative to the drainage case. The origin for the length scale is the sample inlet in the drainage case. In flooding situations with reversed flow direction the origin is the sample outlet. The length scale is thus fixed relative to the sample.

Like the experimental procedure, the parameter estimation technique is divided into drainage and imbibition parts, as described below. Elaborate information on initial and boundary conditions for the mathematical model can be found in Bech et al.[31]

Drainage. The drainage case initial conditions correspond to a core plug saturated with water. The plug is drained by injecting oil at a constant rate. Given enough time, flooding the sample at constant rate results in a steady-state situation, where only the displacing fluid is flowing. The Darcy equation for the water phase shows that the pressure gradient in the displaced water phase is zero. In other words, the water pressure is uniform throughout the sample. If the functional relationships of relative permeability to oil and capillary pressure with respect to water saturation are known, then the water saturation profile of a horizontal core plug can be calculated from the following equation, assuming constant porosity and fluid densities:

$$\frac{dS_w}{dx} = -\frac{\mu_o}{kk_{ro}} \frac{q_o}{A} \frac{1}{\dfrac{dp_c}{dS_w}}. \qquad (3)$$

The functional relationships of the oil relative permeability and the capillary pressure are assumed to be uniquely described by two sets of parameters

$$k_{ro}(S_w) = f_a(a_1, a_2, \dots, a_{no}, S_w), \qquad (4)$$

$$p_c(S_w) = f_b(b_1, b_2, \dots, b_{nc}, S_w). \qquad (5)$$

To determine the drainage capillary pressure and the drainage relative permeability to oil, data from the stationary flow drainage experiment is used, i.e., step 3 of the experimental procedure. In this experiment the steady-state saturation profile of the sample and the oil-phase pressure at the inlet is measured. The unknown parameters a_i, $i=1,no$ and b_i, $i=1,nc$ are determined by means of a parameter estimation technique. For a given set of coefficients a_i and b_i in Eqs. 4 and 5 the water saturation S_w, the oil relative permeability k_{ro}, and the capillary pressure p_c are calculated from Eqs. 3–5. The coefficients a_i and b_i are determined so that they minimize the following least-squares objective function

$$J_1(\bar{a},\bar{b}) = \sum_{i=1}^{M} [S_w^C(x_i) - S_w^m(x_i)]^2 F_{w1}^2 + (\Delta p_{o,T}^C - \Delta p_{o,T}^m)^2 F_{w2}^2$$

$$+ (p_{th}^C - p_{th}^m)^2 F_{w3}^2 + (p_{o,\text{out}}^C - p_{o,\text{out}}^m)^2 F_{w4}^2. \tag{6}$$

The squared residuals are scaled by means of weight factors F_w to make their contribution to the objective function similar in size.

The objective function Eq. 6 is minimized by use of a standard nonlinear least-square solver [MI0L2 (Ref. 32)].

In order to determine the relative permeability to water, the transient flow drainage experiment is used, i.e., step 2 of the experimental procedure. The relative permeability to water is also represented by a functional relationship of the water saturation:

$$k_{rw}(S_w) = f_c(c_1, c_2, \ldots, c_{nw}, S_w). \tag{7}$$

The coefficients are determined so that they minimize the following least-squares objective function, by use of the same nonlinear least-square solver as above:

$$J_2(\bar{c}) = \sum_{i=1}^{N} [\Delta p_{o,T}^C(t_i) - \Delta p_{o,T}^m(t_i)]^2. \tag{8}$$

For a given set of coefficients, c_i, the relative permeability to water is calculated from Eq. 7. The relative permeability to oil and the capillary pressure are known from above.

The transient part of the drainage process is computed by means of a commercial reservoir simulator [ECLIPSE 100 (Ref. 33)]. The extraction of results from the ECLIPSE output file is performed by means of software developed by Frandsen.[34] The objective function Eq. 8 is minimized by use of the nonlinear least-square solver referenced above.

Imbibition. It is assumed in the present work that the water relative permeability exhibits no hysteresis.[35,36] In other words, the relative permeability function determined for the drainage case also applies to the imbibition cases. In order to determine the imbibition part of the saturation functions, the experiment is continued in two steps:

Experimental step 4: The end effect is shifted to the opposite end of the core ($x=0$) by reversing the direction of the oil flow.

Experimental step 5: The plug is flooded by water injected through the face $x=L$.

The experiments are simulated by means of ECLIPSE.

Imbibition Case I (Experimental Step 4). The development of an end effect at the new sample outlet follows an internal imbibition process, while the old end effect is broken down by an internal drainage process. The saturation profile at the new sample outlet can be used in the calculation of the saturation functions for the imbibition process. Recall that the bounding saturation curves are obtained under the initial condition of $S_w = 100\%$ and $S_w = S_{iw}$ for the drainage and imbibition processes, respectively. The reversed drainage process violates this condition and scanning curves between the bounding saturation functions will, therefore, control the process. The scanning process is described by a method developed by Killough.[36] The scanning curves are dependent on the local saturation history of the sample.

Data from the stationary flow internal imbibition experiment, i.e., experimental step 4, are used to determine the imbibition relative permeability to oil, the spontaneous part of the imbibition capillary pressure, and the scanning parameter ϵ, which controls how the primary drainage and spontaneous imbibition capillary pressure curves are weighted to form the scanning curves. In this experiment the total pressure drop and the saturation profile are measured in the steady state, which follows the reversal of the oil flow direction. The imbibition relative permeability to oil and the imbibition capillary pressure are represented by functional relationships similarly to Eqs. 4 and 5. The coefficients a_i, b_i, and ϵ are determined by the least-squares solver so they minimize the following least-square objective function:

$$J_3(\bar{a},\bar{b},\epsilon) = \sum_{i=1}^{M} [S_w^C(x_i) - S_w^m(x_i)]^2 F_{w1}^2$$

$$+ (\Delta p_{o,T}^C - \Delta p_{o,T}^m)^2 F_{w2}^2. \tag{9}$$

Imbibition Case II (Experimental Step 5). Finally, in order to determine the forced part of the imbibition capillary pressure, the core plug is flooded with water in the forced flow imbibition experiment, i.e., step 5 of the experimental procedure. The capillary pressure is represented by a functional relationship similar to Eq. 5. The coefficients b_i are determined so that they minimize the following least-square objective function:

$$J_4(\bar{b}) = \sum_{i=1}^{N} [\Delta p_{w,T}^C(t_i) - \Delta p_{w,T}^m(t_i)]^2. \tag{10}$$

Analytical Representation of Saturation Functions. The saturation functions are given as functional relationships of the water saturation.

Relative Permeabilities. The relative permeabilities are represented by power laws. The water relative permeability is given by the following expression, which is used both for drainage and imbibition, i.e., no hysteresis for the wetting-phase permeability occurs,

$$k_{rw} = c_1 (S_w^{*,dr})^{c_2}, \tag{11}$$

where

$$S_w^{*,dr} = \frac{S_w - S_{iw}}{1 - S_{iw}}. \tag{12}$$

The oil relative permeability is given as

$$k_{ro} = a_1 (S_o^*)^{a_2}, \tag{13}$$

where hysteresis is taken into account by

$$S_o^{*,dr} = \frac{S_o}{1 - S_{iw}}, \tag{14}$$

$$S_o^{*,imb} = \frac{S_o - S_{or}}{1 - S_{or} - S_{iw}}. \tag{15}$$

Capillary Pressure. The capillary pressure function is divided into a drainage and an imbibition case. In the drainage case the capillary pressure is represented by the following functions:

$$p_c = \frac{b_1}{(S_w + b_2)^{b_3}} + f_1 \quad \text{if} \quad S_w \leq S_w^0, \tag{16}$$

$$P_c = \frac{f_2}{S_w + b_4} + f_3, \quad \text{if} \quad S_w > S_w^0. \tag{17}$$

Two pieces of the curve are used in order to permit a proper representation of cases with a point of inflection.

The parameters f_1 to f_3 are determined in such a way that the capillary pressure function Eqs. 16–17 satisfy

$$p_c(S_{iw}) = p_{c,\max}, \tag{18}$$

$$p_c(S_w^0) = p_c^0, \tag{19}$$

$$p_c(1) = 0, \tag{20}$$

$$\left(\frac{dp_{c,\text{Eq. 16}}}{dS_w}\right)_{S_w = S_w^0} = \left(\frac{dp_{c,\text{Eq. 17}}}{dS_w}\right)_{S_w = S_w^0}. \tag{21}$$

The capillary pressure, p_c^0 at $S_w = S_w^0$ is a sixth unknown. The expressions for the parameters f_1 to f_3 are given in Olsen et al.[37] We define the threshold pressure as

$$p_{th} = p_c^0 + \left(\frac{dp_c}{dS_w}\right)_{S_w = S_w^0} (1 - S_w^0). \tag{22}$$

In the imbibition case the capillary pressure is given as

TABLE 2– PLUG M113 PARAMETERS

$L = 74.7$ mm	$\mu_o = 0.92$ cp
$A = 1124$ mm^2	$S_{or} = 0.28$
$\phi = 0.264$	$S_{wi} = 0.064$
$k = 0.70$ mD	$S_{w,spt} = 0.68$
$C_r = 1.76 \times 10^{-3}$ atm^{-1}	$p_{c,max} = 5.527$ atm
$\rho_w = 1.049$ g/mL	$p_{o,out} = 1.0$ atm
$\mu_w = 1.12$ cp	$p_{th} = 1.836$ atm
$C_w = 4.58 \times 10^{-5}$ atm^{-1}	$q_o^{dr} = 10.0$ mL/h
$\rho_o = 0.73$ g/mL	$q_o^{imb} = -23.0$ mL/h
$C_o = 1.16 \times 10^{-4}$ atm^{-1}	$q_w^{imb} = -5.0$ mL/h

$$p_c = \frac{e_1}{S_w + d_1} + e_2, \quad \text{if } S_w \leq S_{w,spt}, \qquad (23)$$

$$p_c = e_3(S_w - d_2)^{e_5} + e_4, \quad \text{if } S_w > S_{w,spt}. \qquad (24)$$

The parameters e_1 to e_5 are determined in such a way that the capillary pressure function Eqs. 23–24 satisfy

$$p_c(S_{iw}) = p_{c,max}, \qquad (25)$$

$$p_c(S_{w,spt}) = 0, \qquad (26)$$

$$p_c(1 - S_{or}) = p_{c,min}, \qquad (27)$$

$$\left(\frac{dp_{c,\text{Eq. 23}}}{dS_w}\right)_{S_w = S_{w,spt}} = \left(\frac{dp_{c,\text{Eq. 24}}}{dS_w}\right)_{S_w = S_{w,spt}}. \qquad (28)$$

$S_{w,spt}$ is the saturation where the imbibition capillary pressure is zero. It is assumed here that $S_{w,spt}$ is known. The expressions for the parameters e_1 to e_5 are given in Olsen et al.[37]

Test of the Parameter Estimation Technique. The parameter estimation technique was tested on a numerical core plug characterized by a set of synthetic saturation functions. The drainage case and imbibition cases I and II were simulated by means of ECLIPSE. The resulting fluid saturation distributions and pressure drop curves were treated as measured experimental results in this synthetic case.

Excellent agreement was found to exist between the calculated results and the specified saturation functions demonstrating that the present procedure for calculating saturation functions from saturation profiles and production data is valid for ideal synthetic data.

It was found that it is important to know the threshold pressure. If the threshold pressure is not available the simultaneous iterations on oil relative permeability and capillary pressure may converge towards an erroneous solution. This is because the water saturation gradient, Eq. 3, is a function of the product of the oil relative permeability and the gradient of the capillary pressure with respect to water saturation. An additional fixpoint of the capillary pressure curve is needed other than the two end points.

Results and Discussion

For two plugs labeled M113 and M16H, saturation functions are presented, as determined by use of the five-step flooding procedure and the parameter estimation technique.

Plug M113. The M113 plug parameters and some experimental conditions are given in **Table 2** and the measured saturation profiles in Fig. 1.

Primary Drainage, Results. The calculated capillary pressure as well as the relative permeabilities to oil and water for the drainage case are shown in **Figs. 2 and 3**.

The resulting match of the steady-state water saturation profile and the transient total pressure drop are shown in **Figs. 4 and 5**. Good agreement exists between the calculated and measured saturation profiles. For the pressure drop some deviations exist but the general curve shapes are similar.
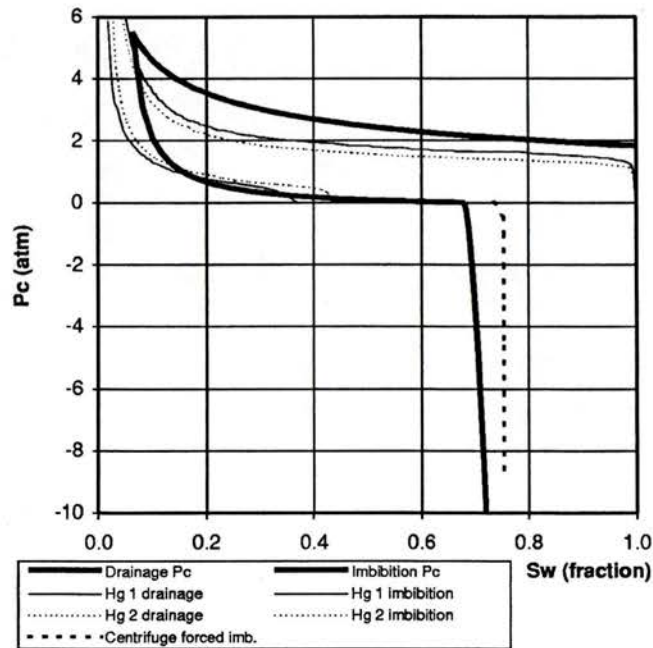

Fig. 2–Measured and calculated capillary pressure functions for sample M113.

Imbibition, Results. The calculated imbibition capillary pressure and relative permeability to oil are shown in Figs. 2 and 3. The scanning parameter was estimated to be 0.0375. The resulting match of the steady-state water saturation profile following the reversal of the oil flow direction is shown in Fig. 4. The general curve shape is predicted well. This is, however, not the case with the transient pressure drop during the reverse waterflooding, **Fig. 6**. The calculated pressure drop is smaller than the measured one. The reason for this behavior is not clear. It may be that the relative permeability to water is overestimated for the upper part of the water saturation interval. This in turn could indicate that the assumption of no hysteresis in the water relative permeability does not hold. Another supplementary explanation could be that the functional form, Eq. 11, is not satisfactory. It might be better to
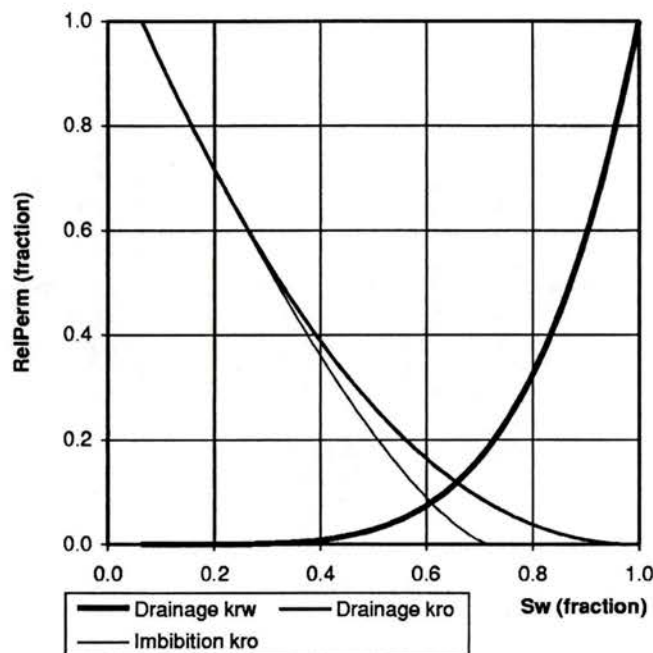

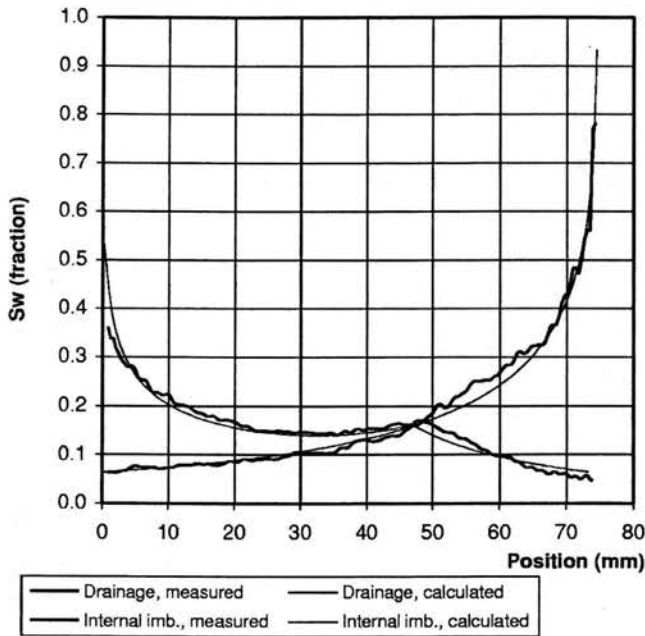Fig. 3–Calculated relative permeability functions for sample M113.
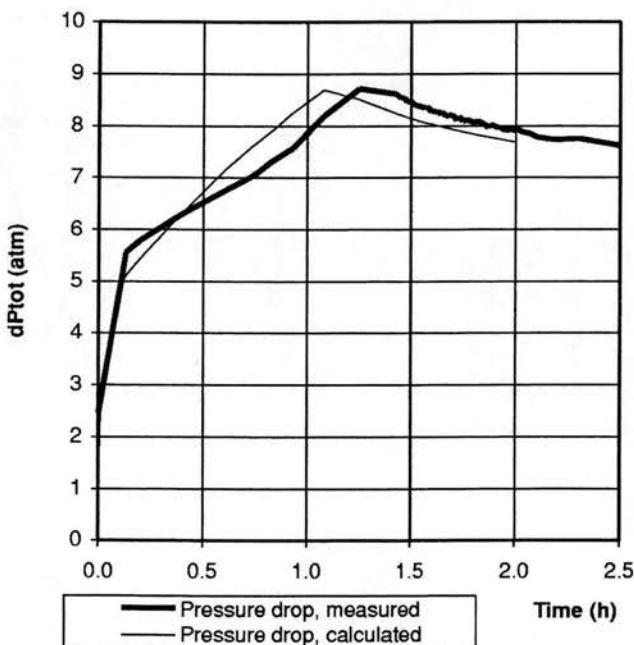
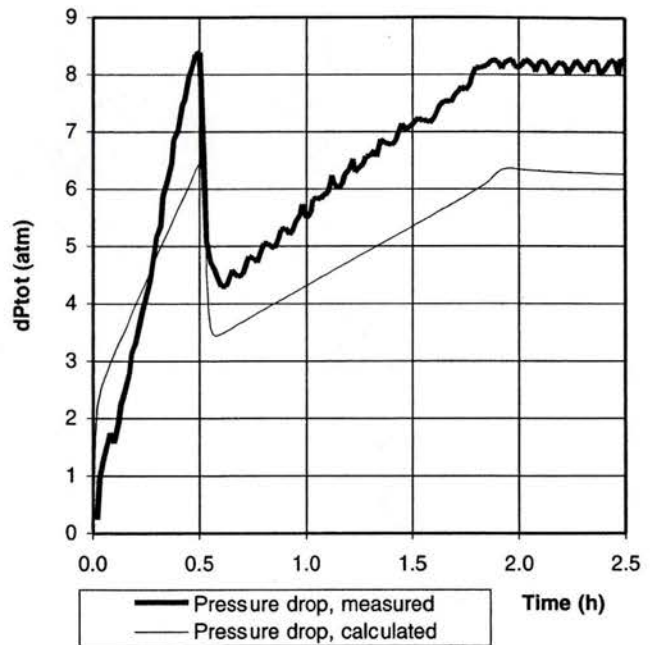Fig. 4–Measured and calculated saturation profiles for sample M113.

Fig. 6–Measured and calculated pressure drop for sample M113, forced imbibition case. At 0.5 h the flow rate was reduced from 10 to 5 mL/h.

use a combination of two different exponential functions, an exponential function and a straight line or perhaps B splines as suggested by Nordtvedt et al.[7] As pointed out by Kerig and Watson,[4] the exponential function is rather stiff. We have been using it here primarily to test the parameter estimation technique. In the future we will be looking for more flexible analytical representations of the relative permeabilities. At the same time, however, we will try to limit the number of unknowns as far as possible in order to reduce computation time as well as the risk of arriving at false solutions. A small objective function is no guarantee for a good solution.

The determined capillary pressure curves are compared with results obtained from a standard mercury injection technique and centrifuge method on the same plug, Fig. 2. The mercury injection

curves are scaled by Leverett's J function using a standard value of 480 mN/m for the interfacial tension for the mercury/vapor system and a measured value of 38 mN/m for the oil/water system. No correction for contact angle is applied as the sample was strongly water-wet.[38] The drainage part of the capillary pressure curve is similar in shape to the mercury drainage curves, but the mercury injection data have a wider and more flat plateau. A similar situation has been reported previously.[19,39] The spontaneous part of the capillary pressure curve shows a significant deviation with respect to the mercury curves. The mercury injection technique gives a much lower capillary pressure at wetting-phase saturations below 0.15, together with a lower irreducible saturation. The lower irreducible saturation for the mercury injection technique may be caused by the high mercury drainage pressure, up to 2,000 bar. This may cause failure of the matrix as mercury penetrates into pore space, which previously was isolated for the nonwetting phase, as suggested by Christoffersen.[39] This may also explain the lower wetting-phase saturation obtained at $p_c = 0$ for the mercury curves compared to the presented spontaneous capillary pressure curve. The forced imbibition capillary pressure curve compares reasonably well with a curve determined by the centrifuge technique, Fig. 2. The shape indicates strong wetting preference to water. This is also verified by the measured saturation profile for the waterflood, Fig. 1, which shows an almost uniform water saturation. The centrifuge data do show a lower oil residual saturation, which may be explained from the performance of the centrifuge experiment. The primary drainage of the centrifuge experiment was not completed, i.e., there was water production at the last pressure step applied in the centrifuge. Therefore, the oil residual saturation, for the centrifuge data, is obtained by scanning curves from an incomplete primary drainage process, which will give a saturation between $S_w = 1.0$ and $S_w = 1 - S_{or}$.[36,40] A primary drainage capillary pressure curve could not be calculated from the centrifuge experiment, because the Hassler and Brunner calculation model[10] does not apply when water production has not ceased.

Plug M16H. The M16H plug parameters and some experimental conditions are given in **Table 3**, and the measured saturation profiles in **Fig. 7**.

Fig. 5–Measured and calculated pressure drop for sample M113, drainage case.

Primary Drainage, Results. The calculated capillary pressure as well as the relative permeabilities to oil and water are shown in **Figs. 8 and 9**.

The resulting match of the steady-state water saturation profile and the transient total pressure drop are shown in **Figs. 10 and 11**.

The drainage capillary pressure curve for plug M16H is also compared to mercury data obtained on the same plug, Fig. 8. The results are very similar to plug M113.

Imbibition, Results. The calculated imbibition capillary pressure and relative permeability to oil are shown in Figs. 8 and 9. The scanning parameter was estimated to be 0.0265. The resulting match of the steady-state water saturation profile following the reversal of the oil flow direction is shown in Fig. 10. Again, the general curve shape is predicted well. This is, however, not the case with the transient pressure drop during the reverse water-flooding, **Fig. 12**. The calculated pressure drop is smaller than the measured one just as it was in the case of plug M113. This supports the possible explanation that the relative permeability to water is overestimated for the upper part of the water saturation interval either due to an unsatisfactory analytical representation or because the assumption of no hysteresis in the water relative permeability does not hold.

The determined capillary pressure curves are compared with data obtained from a standard mercury injection technique, Fig. 8. Again, the results are similar to those of plug M113.
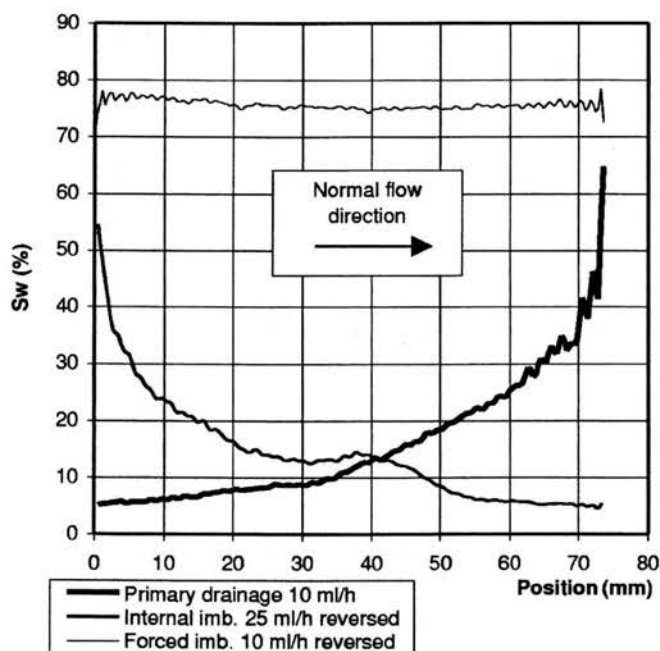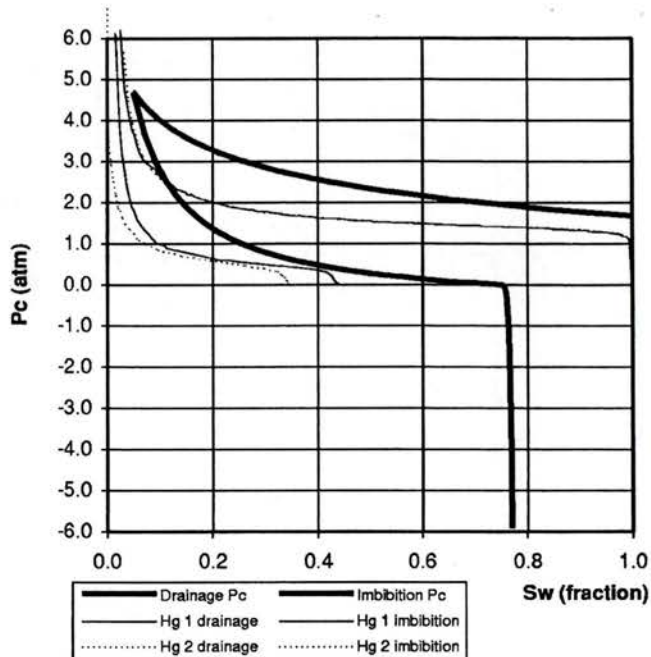

Fig. 8–Measured and calculated capillary pressure functions for sample M16H.

Conclusions

• A procedure to determine saturation functions for low-permeability rocks by a complex flooding procedure combined with a parameter estimation technique has been developed. The procedure utilizes the strong capillary retention of the wetting phase in such rocks. Capillary pressure functions and relative permeability functions, which are unbiased by capillary end effects, are produced for both drainage and imbibition situations.

• The procedure is based upon the following assumptions:
   1. The plug is homogeneous.
   2. The experiments reach a steady state.
   3. The analytical functions used are able to represent the saturation functions of the plug.
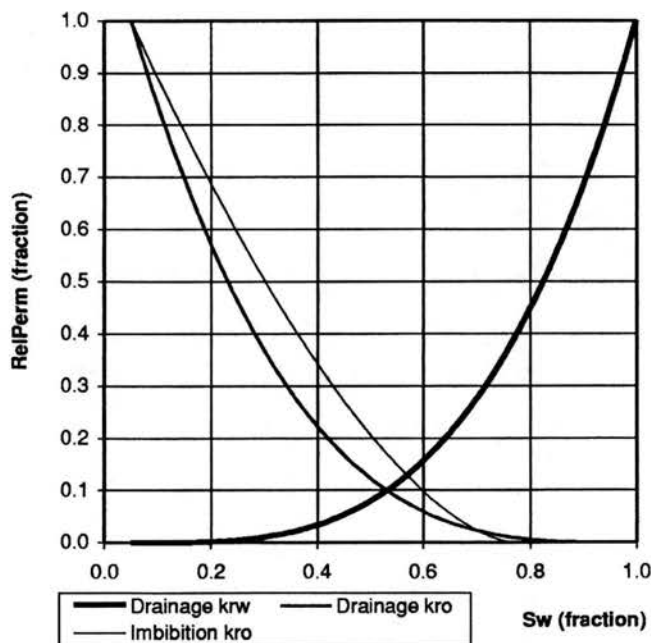

Fig. 7–Measured saturation profiles for sample M16H.

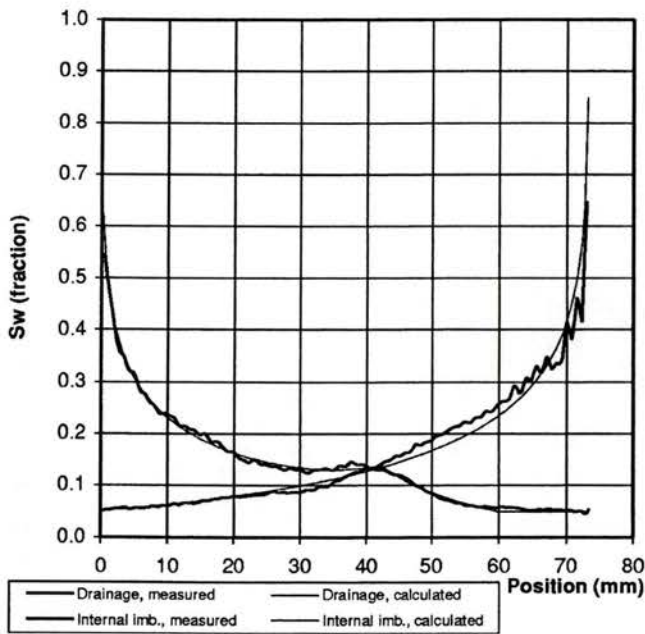**Fig. 9–Calculated relative permeability functions for sample M16H.**

Fig. 10–Measured and calculated saturation profiles for sample M16H.
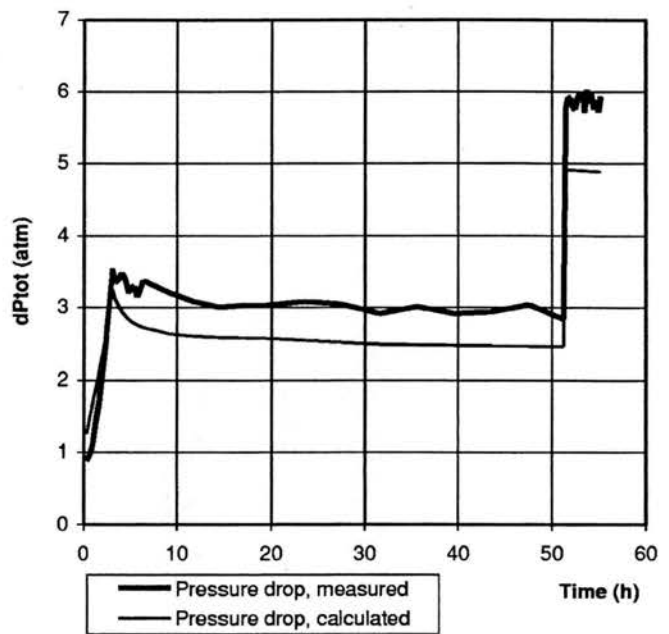

Fig. 12–Measured and calculated pressure drop for sample M16H, forced imbibition case. At 52 h the flow rate was increased from 5 to 10 mL/h.

• The procedure possesses the following advantages:
1. The end effect is utilized and is, therefore, eliminated as a problem.
2. The effects of oil and water relative permeabilities are separated.
3. A consistent set of drainage and imbibition saturation functions are determined.
4. Reservoir-like fluids can be used.
5. The number of simultaneous unknowns is small (1 to 8).

• A complex five-step flooding procedure is presented from which information for calculation of both the drainage and imbibition part of the saturation functions is gained. The procedure utilizes a nonmagnetic core holder connected to a mobile flooding unit to allow saturation profile measurement in an NMR scanner, while the flooding is in progress.
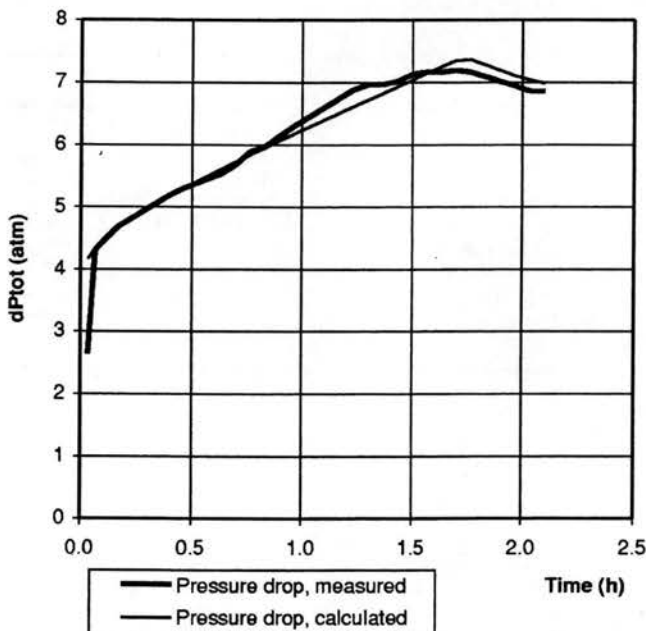
• Saturation profiles are obtained from a 4.7 T NMR scanner, with a one-dimensional chemical shift imaging pulse sequence. The mean accuracy of the pixel fluid saturations is better than 5 p.u., and reproducibility of pixel fluid saturations is better than 2 p.u. The accuracy of the mean fluid saturation of a sample is 2 p.u.

• The drainage saturation functions are calculated from a measured saturation profile, the pressure drop across the sample, and the threshold pressure obtained during a primary drainage process. The calculated drainage capillary pressure curves for two chalk samples are compared with scaled mercury injection data obtained from the same samples. The plateaus of the mercury data are consistently located at significantly lower capillary pressures. It is tentatively suggested that the mercury capillary data are invalidated by the highly aberrant surface tension and contact angle of the mercury/vacuum system, compared to an oil/brine system, and by destruction of the chalk pore structure by the high-pressure injection of mercury. Drainage relative permeabilities for the same two samples are calculated, but no independent verification is available.

• The imbibition saturation functions are calculated from measured saturation profiles and the pressure drop across the sample during two imbibition processes. The calculated spontaneous imbibition capillary pressure curve for two chalk samples are compared with scaled mercury injection data obtained from the same sample. Again, it is found that the plateaus of the mercury data are located at significantly lower capillary pressures, and in addition, the crossover points $p_c = 0$ are located at a much lower wetting-phase saturation. The suggestion of invalid mercury results is advanced as for the drainage case. Contrary to the mercury data, the forced imbibition capillary pressure curve for a centrifuge experiment is found to be in fair agreement with the results.

• The parameter estimation technique determines the capillary pressure scanning parameter ϵ. The determination presented here is based on Killough's method.

• In the present procedure, it is assumed that the relative permeability to water does not exhibit hysteresis. There is some indication that hysteresis is present. For both plugs considered, the measured forced imbibition pressure drop was underestimated using drainage water relative permeabilities. It may be an improvement to include a determination of the imbibition relative permeability to water in the parameter estimation technique.

Fig. 11–Measured and calculated pressure drop for sample M16H, drainage case.

• The wettability of a sample can be obtained directly from the set of capillary pressure curves.

Nomenclature

a = pore size, μm or coefficient
$\bar{a}$ = parameter vector
A = flow area, mm^2
b = coefficient
$\bar{b}$ = parameter vector
B_0 = main magnetic field, T
c = coefficient
$\bar{c}$ = parameter vector
C = Compressibility, atm^{-1}
e_1 = parameter in the analytical expression of the imbibition capillary pressure
e_2 = parameter in the analytical expression of the imbibition capillary pressure, atm
e_3 = parameter in the analytical expression of the imbibition capillary pressure
e_4 = parameter in the analytical expression of the imbibition capillary pressure, atm
e_5 = parameter in the analytical expression of the imbibition capillary pressure
E = noise level
f_a = analytical representation of the oil relative permeability
f_b = analytical representation of the capillary pressure, atm
f_c = analytical representation of the water relative permeability
f_1 = parameter in the analytical expression of the drainage capillary pressure, atm
f_2 = parameter in the analytical expression of the drainage capillary pressure
f_3 = parameter in the analytical expression of the drainage capillary pressure, atm
F_w = weight factor
J = objective function
k = absolute permeability, md
k_{ro} = relative permeability to oil, fraction
k_{rw} = relative permeability to water, fraction
L = length of core sample, mm
M = magnetization or number of squared saturation residuals
N = number of squared pressure drop residuals
p = pressure, atm
p_c^0 = $p_c(S_w^0)$
P = probability density function
q = flow rate, ml/h
S = fluid saturation, fraction
S_{or} = oil residual saturation, fraction
S_{iw} = irreducible water saturation, fraction
S^* = scaled saturation
S_w^0 = defined by Eqs. 16 and 17
t = time, hours
t_e = echo time, ms
t_r = repetition time, ms
T_1 = spin-lattice constant, ms
T_2 = spin-spin constant, ms
x = direction of flow downstream, mm
ϵ = scanning parameter
ϕ = porosity, fraction
μ = viscosity, cp
ρ = density, g/mL
ρ_p = proton density relative to distilled water, mol/L

Subscripts

c = capillary pressure
forced = forced imbibition
in = inlet of core sample
nc = number of coefficients (capillary pressure)

no = number of coefficients (relative permeability to oil)
nw = number of coefficients (relative permeability to water)
o = oil
out = outlet of core sample
spt = spontaneous imbibition
T = total
th = capillary threshold
w = water

Superscripts

C = calculated
dr = drainage
imb = imbibition
m = measured

Acknowledgments

References

1. Kulkarni, R.N., et al.: "Estimation of Multiphase Flow Functions from Dynamic Displacement Data: Applications of NMR Imaging," paper SPE 36855 presented at the 1996 SPE European Petroleum Conference, Milan, Italy, 22–24 October.
2. Kohhedee, J.A.: "Simultaneous Determination of Capillary Pressure and Relative Permeability of a Displaced Phase," paper SPE 28827 presented at the 1994 European Petroleum Conference, London, 25–27 October.
3. Chardaire-Riviére, C. et al.: "Simultaneous Estimation of Relative Permeabilities and Capillary Pressure," SPEFE (December 1992) 283.
4. Kerig, P.D. and Watson, A.T.: "Relative-Permeability Estimation From Displacement Experiments: An Error Analysis," SPERE (March 1986) 175; Trans., AIME, 281.
5. Watson, A.T. et al.: "A Regression-Based Method for Estimating Relative Permeabilities From Displacement Experiments," SPERE (August 1988) 953.
6. Richmond, P.C. and Watson, A.T.: "Estimation of Multiphase Flow Functions From Displacement Experiments," SPERE (February 1990) 121.
7. Nordtvedt, J.E., et al.: "Determination of Three-Phase Relative Permeabilities From Displacement Experiments," SPEFE (December 1997) 221.
8. Ramakrishnan, T.S. and Capiello, A.: "A New Technique to Measure Static and Dynamic Properties of a Partially Saturated Porous Medium," Chem. Eng. Sci. (1991) 46, No. 4, 1157.
9. Fordham, E.J. et al.: "Saturation Gradients in Drainage of Porous Media: NMR Imaging Measurements," AIChE. J. (1993) 39, No. 9, 1431.
10. Hassler, G.L. and Brunner, E.: "Measurement of Capillary Pressures in Small Core Samples," Trans., AIME (1945) 160, 114.
11. Christensen, R.L.: "Geometric Concerns for Accurate Measurement of Capillary Pressure Relationships With Centrifuge Methods," SPEFE (December 1992) 311; Trans., AIME, 293.
12. Forbes, P.L., Chen, Z.A., and Ruth, D.W.: "Quantitative Analysis of Radial Effects on Centrifuge Capillary Pressure Curves," paper SPE 28182 presented at the 1994 SPE Annual Technical Conference and Exhibition, New Orleans, 25–28 September.
13. Forbes, P.: "Centrifuge Data Analysis Techniques: An SCA Survey on the Calculation of Drainage Capillary Pressure Curves from Centrifuge Measurements," SCA paper 9714 presented at the 1997 International Symposium of the Society of Core Analysis, Calgary, Alberta, Canada, 8–10 September.
14. Nielsen, C.M. et al.: "Determination of Saturation Functions of Tight Core Samples Based on Measured Saturation Profiles," paper SCA 9721 presented at the 1997 International Symposium of the Society of Core Analysts, Calgary, Alberta, Canada, 8–10 September.
15. Olsen, D. et al.: "Quantitative 1D Saturation Profiles on Chalk by NMR," Magn. Reson. Imaging (1996) 14, No. 7/8, 847.
16. Nicholls, C.I. and Heaviside, J.: "Gamma Ray Absorbtion Techniques Improve Analysis of Core Displacement Tests," paper SPE 14421 presented at the 1985 SPE Annual Technical Conference and Exhibition, Las Vegas, Nevada, 22–25 September.
17. Hicks, P.J.: "X-Ray Computer-Assisted Tomography for Laboratory Core Studies," JPT (December 1996) 1120.

18. Honarpour, M.M., Huang, D.D., and Dogru, A.H.: "Simultaneous Measurements of Relative Permeability, Capillary Pressure, and Electrical Resistivity with Microwave System for Saturation Monitoring," paper SPE 30540 presented at the 1995 SPE Annual Technical Conference and Exhibition, Dallas, 22–25 October.
19. Nørgaard, J.V., et al.: "Capillary Pressure Curves for Low Permeability Chalk Obtained by NMR Imaging of Core Saturation Profiles," paper SPE 30605 presented at the 1995 SPE Annual Technical Conference and Exhibition, Dallas, 22–25 October.
20. Halperin, W.P. et al.: "Magnetic Resonance Relaxation Analysis of Porous Media," in Molecular Dynamics in Restricted Geometries, J. Klafter and J.M. Drake (eds.), John Wiley & Sons, New York City (1989) 311.
21. Edelstein, W.A., et al.: "NMR Imaging for Core Analysis," paper SPE 18272 presented at the 1988 Annual Technical Conference and Exhibition, Houston, 2–5 October.
22. Chen, S. et al.: "NMR Imaging of Multiphase Flow in Porous Media," AIChE. J. (1993) 39, 925.
23. Kulkarni, R. and Watson, A.T.: "Robust Technique for Quantification of NMR Imaging Data," AIChE. J. (1997) 43, No. 8, 2137.
24. Chen, S., Qin, F., and Watson, A.T.: "Determining Fluid Saturations During Multiphase Flow Experiments by NMR Imaging Techniques," AIChE. J. (1994) 40, No. 7, 1238.
25. Kim, K. et al.: "Use of NMR Imaging for Determining Fluid Saturation Distributions During Multiphase Displacement in Porous Media," paper SCA 9219 (1992).
26. Kenyon, W.E. et al.: "A Three-Part Study of NMR Longitudinal Relaxation Properties of Water-Saturated Sandstones," SPEFE (September 1988) 622.
27. Kleinberg, R.L. et al.: "Nuclear Magnetic Resonance of Rocks: T_1 vs T_2," paper SPE 26470 presented at the 1993 SPE Annual Technical Conference and Exhibition, Houston, 3–6 October.
28. Howard, J.J.: "Nuclear Magnetic Resonance Measurements of Wettability and Fluid Saturations in Chalk," 1994 EAPG/AAPG Special Conference on Chalk, Copenhagen, Denmark, 7–9 September.
29. Brownstein, K.R. and Tarr, C.E.: "Importance of Classical Diffusion in NMR Studies of Water in Biological Cells," Phys. Rev. A (1979) 19, No. 6, 2446.
30. Banavar, J.R. and Schwartz, L.M.: "Probing Porous Media with Nuclear Magnetic Resonance," in Molecular Dynamics in Restricted Geometries, J. Klafter and J.M. Drake (eds.), John Wiley & Sons, New York City (1989) pp. 273–309.
31. Bech, N., Olsen, D., and Nielsen, C.M.: "Determination of Oil/Water Saturation Functions of Chalk Core Plugs From Two-Phase Flow Experiments," paper SPE 49325 prepared for presentation at the 1998 SPE Annual Technical Conference and Exhibition, New Orleans, 27–30 September.
32. Madsen, K., Hegelund, P., and Hansen, P.C.: "Nongradient Subroutines for Nonlinear Optimization," 1991 Report Ni-91-05, Institute for Numerical Analysis, Technical University of Denmark, June.
33. ECLIPSE 100, 95A Release, Intera Information Technologies, Ltd., Highlands Farm, Henley-on-Thames, Oxfordshire, U.K. (1994).
34. Frandsen, P.E.: "SIMPE—Small Interface Module for Parameter Estimation," Geological Survey of Denmark and Greenland Report (1998) p. 61.
35. Braun, E.M. and Holland, R.F.: "Relative Permeability Hysteresis: Laboratory Measurements and a Conceptual Model," SPERE (August 1995) 222.
36. Killough, J.E.: "Reservoir Simulation With History-Dependent Saturation Functions," SPEJ (February 1976) 37; Trans., AIME, 261.
37. Olsen, D., Bech, N., and Nielsen, C.M.: "Determination of Saturation Functions and Wettability for Chalk Based on Measured Fluid Saturations," Geological Survey of Denmark and Greenland Report (1998) p. 30.
38. Anderson, W.G.: "Wettability Literature Survey—Part 4: Effects of Wettability on Capillary Pressure," JPT (October 1987) 1283.
39. Christoffersen, K.R.: "High-Pressure Experiments With Application to Naturally Fractured Chalk Reservoirs, 1. Constant Volume Diffusion, 2. Gas-Oil Capillary Pressure," PhD dissertation, University of Trondheim (1992) 214 pp.
40. Aziz, K. and Settari, A.: "Petroleum Reservoir Simulation," Elsevier Applied Science Publishers, Ltd., U.K. (1979).

SI Metric Conversion Factors

cp $\times$ 1.0[*]	E$-$03	= Pa·s
md $\times$ 9.869 233	E$-$16	= m^2
mL/h $\times$ 2.778	E$-$10	= m^3/s
atm $\times$ 1.013 250*	E$+$05	= Pa

*Conversion factors are exact.   **SPEREE**

Niels Bech is a senior researcher in the Dept. of Reservoir Geology at the Geological Survey of Denmark and Greenland (GEUS) in Copenhagen, Denmark. e-mail: nbe@geus.dk. He has worked for more than 13 years with the development and application of reservoir simulators. Bech holds an MS degree in electronic engineering and numerical mathematics from the Technical U. of Denmark. **Dan Olsen** is a senior petrophysicist at the Geological Survey of Denmark and Greenland. e-mail: do@geus.dk. He has worked with the application of NMR imaging and X-ray CT imaging to core analysis since 1989, primarily with measurement of spatially resolved fluid flow, fluid saturation, and porosity in core samples. Olsen holds an MS degree in petrology from the U. of Copenhagen. **Carsten Møller Nielsen** is a petrophysicist at the Geological Survey of Denmark and Greenland. His research interests are fluid flow in porous media and NMR. He holds an MS degree in chemical engineering from the Technical U. of Denmark

Appendix B

Nielsen, Olsen & Bech, *SPE paper 63226 presented at the SPE Annual Technical Conference and Exhibition 1-4 October 2000, Dallas, Texas, 10 pp, 2000.*
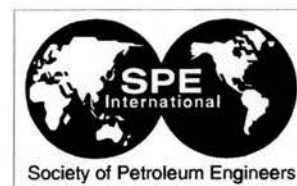
SPE 63226

Imbibition Processes in Fractured Chalk Core Plugs with Connate Water Mobilization

C.M. Nielsen, SPE, Geological Survey of Denmark and Greenland; D. Olsen, SPE, Geological Survey of Denmark and Greenland; N. Bech, SPE, Geological Survey of Denmark and Greenland

Abstract

A displacement process in a chalk core plug with an induced axial fracture uses the fluid system H_2O-D_2O-n-decane. Initially the plug contains a mixture of D_2O and n-decane with oil saturation equal to 88 %. The plug is flooded with H_2O. The displacement process is monitored by NMR with a chemical shift technique enabling spatial resolution of the H_2O and oil signals. The D_2O component is not directly detected, but is calculated from the difference between the actual signal intensities and the signal intensities in a situation where the pore space is completely saturated with H_2O and oil.

H_2O-D_2O-oil constitutes a partly miscible fluid system which is an analogy to the injection water-formation water-oil system of a hydrocarbon reservoir under waterflooding.

The injected H_2O traverses the sample as a well-defined front together with capillary uptake from the fracture plane. Ahead of the H_2O front the D_2O of the sample is mobilized and travels as a bank in front of the H_2O. Though the initial concentration of D_2O is only 12 % the D_2O concentration reaches 50 % at the bank.

The experiment was simulated by means of ECLIPSE with a fair match of the displacement process.

The injected H_2O has only made limited contact with the produced oil of the sample. In case of chemical EOR processes connected to waterflooding of hydrocarbon reservoirs a similar displacement situation could seriously affect the efficiency of the EOR process.

Introduction

Ongoing enhanced oil recovery processes in tight chalk formations, in the Danish section of the North Sea is mainly based on water injection. Fractures, natural or induced, influence the water injection process. Fractures increase the con-ductivity of the reservoir, but the hydrocarbon recovery is greatly dependent on the fracture connectivity and the matrix/fracture mass exchange properties. The present work presents an experimental and numerical study of the water flooding behavior in a plug sample with an axial fracture, i.e. a fracture plane directed parallel to the flow. An NMR chemical shift imaging technique is used to follow both the progressing displacement front and the capillary uptake from the fracture plane.

Experimental procedure

To distinguish between the connate water and the injection water a two component fully miscible brine system is used, i.e. a D_2O-brine (Deuterium Oxide-brine) and H_2O-brine, respectively. At the resonance frequency used herein no NMR signal is acquired from the D_2O component. During the imbibition process the sample contains both oil and the two brines. The D_2O-brine is mapped as the decrease in total NMR signal intensities relative to the final state where the sample only contains oil and H_2O-brine. A 2D NMR chemical shift imaging technique is used. The displacement front is readily resolved by the present imaging technique. The image plane is perpendicular to the fracture plane. No attempt is made to differentiate between signal intensity from the matrix and the fracture. Other workers have used different relaxation techniques to discriminate between fracture/matrix signals and the different phases.[1,2]

Sample Material. A chalk sample labeled M16I of Maastrichtian age from the Dan field in the Danish sector of the North Sea is used in the present work. The sample contains a faint bedding plane and some minor hairlines and trace fossils. The sample was cleaned by Soxhlet extraction prior to the flooding experiment. The absolute permeability of the non-fractured sample is 2 mD. An artificial fracture was mechanically induced in the axial direction following the visible bedding plane. A Brazilian test apparatus was use.[3] The sample was dry when fractured. Before reassembling the sample the fracture aperture was adjusted by applying a thin layer of quarts grains onto the fracture plane. The size of the quarts grains is in the range of 63 – 75 μm. The fracture aperture was determined to be approximately 50 μm.

The initial saturation of the sample was adjusted before the imbibition experiment. First the clean sample was fully satu-

rated with a D_2O-brine. Then it was drained with n-decane on a porous plate to S_w = 12%. The porous plate technique was used to ensure an uniform initial saturation through the sample.

Fluid Data. A three component fluid system is used, a D_2O-brine and H_2O-brine together with n-decane. The salinity of both brines are 1.1 M NaCl. The two brines are doped with $5*10^{-3}$ M $Ni(NO_3)_2$ for NMR purpose. The D_2O used was 99.9% in purity. All fluids are degassed. The viscosity and density for the fluids are given in **Table 1**.

Imbibition experiment. The sample is placed in a non-magnetic Hassler type core holder allowing for NMR measurements. Pure D_2O is used as confining medium to avoid unwanted NMR interference. Initially the sample contains a connate water saturation equal to 12% D_2O-brine and an oil saturation equal to 88% n-decane.

H_2O-brine is injected at constant rate displacing the oil. The injection rate is 150 ml/h. The oil recovery is monitored together with the displacing water pressure, **Fig. 1**. During the imbibition experiment fast non-quantitative 2D NMR data were acquired to follow the progressive imbibition. At two intervals the injection pump was stopped (see Fig. 1) and quantitative 2D NMR data were acquired, **Fig. 2** The two intervals without flow, flow stop 1 and 2, lasted for 40 and 57 minutes, respectively. At the beginning and end of each flow stop NMR measurements were made to check for any redistribution of the phases. For flow stop 1 a minor, but measurable change in distribution is found. This can explain the sudden increase in the displacing water pressure after flow stop 1, Fig. 1. Although the injection is stopped the water in the sample will continue to imbibe into regions of low water saturation due to the strong capillary forces. This redistribution was not measurable during flow stop 2, probably because the water saturation has reached a relative high value in the majority of the sample.

NMR Technique

NMR hardware. A 4.7 T SISCO experimental NMR scanner was used for the NMR work. It was equipped with a 154 mm diameter insert gradient set, capable of producing magnetic gradient up to 140 mT/m along any of three orthogonal directions, with a rise rate of $5.4*10^5$ mT/m*s. The gradient set provides active shielding. A Radio Frequency (RF) coil of slotted tube resonator design with good signal homogeneity until a maximum length of 9 cm was used.

NMR Pulse sequence. The displacement process was monitored with a chemical shift (CSI) technique enabling resolution of the H_2O and oil signals in 2D. The pulse sequence was a spin-echo type sequence, which uses a gauss-shaped RF pulse to selectively excite the desired signal. This method requires that the water and oil resonances are well separated,[4] which was the case for the present work. The water and oil resonances were 700 hz apart with linewidths of 250 hz (FWHM). A sinc-shaped RF pulse was used for slice selec-

tion. The slice thickness was 0.6 cm. The D_2O component was not directly detected, but was calculated from the difference between the actual signal intensities and the signal intensities in situations where the pore space was completely saturated with H_2O and oil.

NMR calculations. Three types of quantitative image data were acquired during the experiment, termed Type AW, Type AO and Type BO, cf. **Table 2**.

Type AW axial images. Six quantitative data sets of type AW with an axial orientation were acquired with the selective RF pulse tuned to water. A technique of arrayed acquisition was used. By this a number of images corresponding to an array of t_e values are acquired, allowing relaxation correction to be done. A drawback of this method is that it is relatively slow. This circumstance required the fluid flow to be stopped during data acquisition. Duplicate data sets were acquired during the no-flow periods as a check for fluid redistribution. Type AW images were also acquired before the start and after the end of the displacement experiment.

Axial images Type AO and BO. Six quantitative data sets were acquired with the selective RF pulse tuned to oil. These data sets are similar to the type AW images. Type AO and type BO only differ by the value of the repetition time t_r.

Additional axial and transaxial images. A total of 42 additional data sets were acquired during the experiment as images using a single t_e value. The benefit compared to the arrayed-t_e images is a much faster data acquisition. The acquisition time for the single-t_e value images was reduced to 60-90 seconds, allowing tracking of the displacement while the flooding was in progress. The cost of this comparatively fast data acquisition was the inability to correct for signal relaxation. Therefore, the additional images are not quantitative. The additional images were used to confirm that the displacement process as shown on the quantitative images are representative for the whole sample.

Relaxation Correction. The effect of spin-lattice relaxation may be eliminated by selecting the repetition time t_r at least 6 times the longest T_1 component present in the sample. This convention assures that the error on signal intensity due to differential saturation of the NMR signals is less than 1% of the detected signals. The convention was followed for the type AW and AO images. Due to time constraints, t_r was reduced to 3 times the value of the longest T_1 component for the type BO images. This resulted in up to 10% saturation of the NMR signal. The effect was partially compensated by multiplying the signal intensities of the BO images by the ratio of intensities AO/BO determined at the start and end of the experiment. It is, however, estimated that an uncorrected variation of a few percent remains.

The spin-spin relaxation of the sample is compensated by a relaxation modelling on an array of data sets.[5-9] The array of data sets is acquired, with identical acquisition parameters, except for different values of t_e. A spin-spin relaxation model is then calculated for each pixel array, producing 2D data sets of the fitted parameters, which includes the magnetization at time zero, $M(t=0)$. The t_e values of the setup are selected for

optimum definition of the relaxation. Downwards the setting of t_e is restricted by system hardware constraints, which in the case of the CSI pulse sequence resulted in $t_{e,min}$, being 7.1 ms. The smallest t_e value is selected to be equal to $t_{e,min}$, in order to trace the relaxation path as close to the $M(t=0)$ condition as possible.

An important issue is the choice of spin-spin relaxation model. Bi-exponential or stretched exponential models are commonly necessary to produce reliable models,[10,11] but a cleaned chalk sample, like the actual sample, is usually confidently modelled by a single-exponential model.[12-14] In the present work single-exponential modelling is used, i.e.

$$M(t) = M(t=0)exp(-t/T_2) + E \quad \dots\dots\dots\dots\dots\dots(1)$$

where E is the signal level (noise) at $t=\infty$. The CSI pulse sequence used in the present work has a large $t_{e,min}$, which results in long extrapolations from $M(t=t_{e,min})$ to $M(t=0)$. The apparent spin-spin time constant T_2^* for both H_2O and oil varies mainly between 3.3 and 4.2 ms., and the ratio $M(t=t_{e,min})/M(t=0)$ varies mainly between 0.11 and 0.18. These long extrapolations in the relaxation model are the main causes of the poor signal/noise ratios in the saturation model (Fig. 2). The signal/noise ratio is particularly bad along the trace of the fracture where the T_2 values was accidentally lowered by the introduction of some unidentified substance during sample preparation.

Fluid saturation calculation. For the fluids H_2O and oil, it is assumed that the following relationship is valid

$$M(t=0)_{f,i} = C_i V_i \varphi_i S_{f,i} D_f \quad \dots\dots\dots\dots\dots\dots\dots\dots(2)$$

For the initial and final state of the experiment $CV\varphi$ values were calculated for every pixel as

$$C_i V_i \varphi_i = \frac{M(t=0)_{f,i}}{S_{f,i} D_f} \quad \dots\dots\dots\dots\dots\dots\dots\dots(3)$$

where $M(t=0)_{f,i}$ was taken from the relaxation corrected AW, AO and BO data sets, and D_f was calculated from the chemical composition of the fluid. For the initial state it was assumed that S_O was 88 % for every voxel, while for the final state it was assumed that

$$S_{H2O,i} = \frac{M(t=0)_{H2O,i}}{[M(t=0)_{H2O,i} + M(t=0)_{o,i}]} \quad \dots\dots\dots\dots\dots(4)$$

i.e. S_{D2O} is assumed to be zero. $CV\varphi$ is constant for every voxel during the experiment, except for instrumental drift. A $CV\varphi$-map for the whole experiment was therefore prepared by pixel-wise averaging of the $CV\varphi$-maps for the initial and final states

$$C_{av,i} V_{av,i} \varphi_{av,i} = (C_{init,i} V_{init,i} \varphi_{init,i} + C_{end,i} V_{end,i} \varphi_{end,i})/2 \quad \dots\dots(5)$$

The H_2O and oil saturations for all four experimental steps were then calculated as

$$S_{f,i} = \frac{M(t=0)_{f,i}}{C_{av,i} V_{av,i} \varphi_{av,i} D_f} \quad \dots\dots\dots\dots\dots\dots\dots\dots(6)$$

Finally, the saturation of D_2O was calculated as

$$S_{D2O,i} = 1 - (S_{H2O,i} + S_{o,i}) \quad \dots\dots\dots\dots\dots\dots\dots(7)$$

Maps of S_{H2O}, S_{D2O} and S_o prepared by this procedure are presented in Fig. 2.

Numerical Simulations

The immiscible flooding experiment has been simulated by means of the ECLIPSE reservoir simulator.[15] Modelling assumptions imposed are:

- The plug is homogeneous.
- The cylindrical core plug contains a single vertical fracture plane through the axis.
- The initial saturation distribution is uniform (12% D_2O and 88% oil).
- The flow pattern in the plug is symmetric with respect to the fracture plane and a plane perpendicular to the fracture plane through the plug axis.

Grid. The above assumptions dictate that only one quarter of the plug is considered. This quarter plug section and its bounding inlet and outlet chambers are modelled by means of a 3D Cartesian grid with with $(n_x, n_y, n_z) = (62, 25, 16)$, see **Table 3**. The inlet and outlet chambers are modelled by the grid planes $i = 1$ and $i = n_x$, respectively. The core plug thus contains $60*25*16 = 24000$ grid cells.

Rock Properties. Plug porosity and permeabilities have been determined as described previously in Olsen *et al.*[13] It turned out that the fracture contained two blockages located 3.16 cm and 5.51 cm from the inlet, respectively. The rock properties are shown together with plug dimensions and fluid properties in **Table 4**.

Saturation Functions. Capillary pressure and relative permeabilities have not been measured for this core plug. Functions determined for another but similar plug, M16H, have been used in the present simulation, conf. Figs. 8 and 9 in Bech *et al.*[12] For the fracture linear relative permeabilities and zero capillary pressure were used.

Operating Conditions. From time zero, H_2O-brine was injected at a constant rate of 150 ml/hr. In the simulations, the injected water (H_2O) was doped with a passive tracer in order to permit a distinction between injection water and formation water (D_2O). In order to create a uniform inlet velocity the

water injection was carried out through n_y wells completed in each of the n_z layers as described in Olsen et al.[13]

Results and Discussion

Recovery is up to 75% of the oil original in place (OOIP) for the imbibition experiment, **Fig. 1**. A total of 4-5 pore volumes are injected before production ceases, because a large part of the water flow is confined to the fracture. The 2D NMR measurements show how the injection water (H_2O-brine) traverses the sample, **Fig. 2**. A regular injection water front travels from the inlet end towards the outlet end, in combination with capillary uptake of injection water from the fracture. Moreover it is evident from the NMR images that the connate water (D_2O-brine) is mobilized and travels ahead of the injection water. The connate water is piled up as a bank and reaches a saturation up to 50%. Evidence of the formation water being swept in front of the injection water is recorded in the field.[16]

The bank effect of the connate water limits the contact between the injection water and the oil. This could have great impact on chemical EOR processes in combination with water injection.

Modeling Results. Reservoir simulation of the imbibition experiment provides a detailed picture of the displacement.

Flow Patterns. Several observations can be made from the oil and water flow patterns calculated at different points of time:

- Oil is produced by counter-current flow to the inlet chamber.
- Oil is produced by counter-current flow to the fracture.
- Oil is produced to the outlet chamber by:
  - Co-current flow in the very beginning and at later times.
  - A mixture of co-current and more or less counter-current flow at intermediate times. During this period water imbibes from the outlet chamber back into the plug.

Oil and water flow patterns after injection of 1.49 pore volumes (PV) are shown in **Fig. 3**. At this time oil is produced to the outlet chamber by a mixture of co-current and counter-current flow.

Production Pattern. The contributions to the cumulative production of oil are given in **Fig. 4**. The results show that about 70% more oil is produced to the fracture by imbibition, than by flooding to the outlet chamber.

Saturation Distributions. The measured and simulated saturation distributions are illustrated by axial and radial saturation profiles. The axial profiles are positioned at 1.17 cm from the fracture plane, and the radial profiles are positioned at a distance of 3.23 cm from the sample inlet. In **Fig. 5** are shown the simulated axial saturation distributions of total water ($H_2O + D_2O$), injection water (H_2O) and formation water (D_2O) after injection of 1.49 PV. It is seen that the D_2O is mobilized and travels as a bank in front of the injected H_2O. The simulated radial profiles in **Fig. 6** show that the water

imbibing from the fracture has a similar effect on the D_2O. This supports the NMR pictures, Fig. 2.

Comparison to Measurements. Measured and calculated oil saturation after injection of 1.49 PV are compared in **Figs. 7** and **8**. Saturation trends and levels compare relatively well.

Measured and calculated H_2O and D_2O saturation distributions are compared in **Figs. 9 – 12**. Again, the measured and calculated distributions have the same shape and level, but large deviations exist.

Possible reasons for the discrepancies are:

- Judging from the NMR images the plug is obviously not homogeneous. This affects the fluid distributions.
- The assumed uniform initial saturation distribution (12% D_2O and 88% oil) deviates from the true initial state.
- From the NMR images is also seen that the fracture is not formed as a regular vertical slab of constant thickness with two blockages.
- The input relative permeabilities are determined for co-current flow and may not represent the complex displacement of both co- and counter-current flow.
- The saturation functions used are not those of the actual plug.
- The water viscosity used is that of H_2O. The viscosity of D_2O is 23% larger.

Conclusions

An imbibition process in a chalk plug sample with an axial fracture plane is visualized by a 2D NMR chemical shift imaging technique.

A D_2O-H_2O-brine system is used to separate connate water and injection water.

The imbibition process is a combination of front displacement and capillary uptake from the fracture plane.

Experimental results show that the connate water is mobilized and travels as a bank in head of the water injection front. Numerical modeling supports the evidence of connate water mobilization.

The connate water saturation increases in the bank as the sample is being swept.

The effect of connate water mobilization may have negative influence on chemical EOR processes connected to water injection.

Oil is produced by a mixture of co-current and counter-current flow.

Acknowledgments

Nomenclature

a	=	fracture aperture, µm
C	=	compressibility, bar^{-1}
		NMR machine response constant for distilled water, SISCO units
d	=	plug diameter, cm
D	=	NMR proton density relative to distilled water
E	=	signal noise level
k	=	absolute permeability, mD
L	=	length of core sample, cm
$M(t)$	=	NMR magnetization at time t, SISCO units
n	=	number of grid cells
S	=	fluid saturation, fraction
T_1	=	spin-lattice constant, ms
T_2	=	spin-spin constant, ms
T_2^*	=	NMR apparent spin-spin time constant, ms
t	=	time, min
t_e	=	echo time, ms
t_r	=	repetition time, ms
V	=	volume of NMR voxel
x	=	axial coordinate, cm
y	=	lateral coordinate, cm
z	=	vertical coordinate, cm
φ	=	porosity, fraction

Subscripts

av	=	average
$blck1$	=	fracture blockage no. 1
$blck2$	=	fracture blockage no. 2
$D2O$	=	deuterium oxide
end	=	final state of experiment
f	=	fluid, fracture
$H2O$	=	light water
i	=	x-direction coordinate index
$init$	=	initial state of experiment
m	=	matrix
min	=	minimum
o	=	oil
$plug$	=	core plug
$rock$	=	matrix rock
x	=	refers to x-direction
y	=	refers to y-direction
z	=	refers to z-direction
w	=	water

References

1. Chen, S., Yao, X., Qiao, J., Watson, A.T.: "MRI Investigation of Fractures and Multiphase Flow in Fractured Media," *AICHE J.* (1996) **42**, 3 820.

2. Kumar, A.T.A., Majors, P., Rossen, W.: "Measurement of Aperture and Multiphase Flow in Fractures With NMR Imaging," *SPE Formation Evaluation*, (June 1997) 101.

3. Tiab.D., Donaldson. E.C.: *Petrophysics – Theory and Practice of Measuring Reservoir Rock and Fluid Properties,* Gulf Publishing Company, Texas, (1996).

4. Horsfield, M.A., Hall, C., and Hall, L.D.: "Two-Species Chemical-Shift Imaging Using Prior Knowledge and Estimation Theory. Application to Rock Cores", *J. Mag. Res.(1990) 87, 319.*

5. Fordham, E.J., Hall, L.D., Ramakrishnan, T.S., Sharpe, M.R., Hall C.: "Saturation Gradients in Drainage of Porous Media: NMR Imaging Measurements", AIChE Journal, (1993) **39**, No. 9

6. Edelstein, W.A., Vinegar, H.J., Tutunjian, P.N., Roemer, P.B and Mueller, O.M.: "NMR Imaging for Core Analysis," paper SPE 18272 presented at the 1988 Annual Technical Conference and Exhibition, Houston, October 2-5

7. Chen, S., Qin, F., Kim, K and Watson, A.T.: "NMR Imaging of Multiphase Flow in Porous Media," *AIChE Journal* (1993) 39, 925.

8. Kulkarni, R., Watson, A.T.: "Robust Technique for Quantification of NMR Imaging Data", AIChE Journal (1997) 43, No. 98

9. Chen, S., Qin, F., Watson, A.T.: "Determining Fluid Saturations during Multiphase Flow Experiments by NMR Imaging Techniques", AIChE Journal (1994) 40, No. 7.

10. Kim, K., Chen, S., Qin, F. and Watson, A.T.: "Use of NMR Imaging for Determining Fluid Saturation Distributions During Multiphase Displacement in Porous Media," paper SCA 9219 (1992).

11. Kenyon, W.E., Day, P.I., Straley, C. and Willemsen, J.F.: "A Three Part Study of NMR Longitudinal Relaxation Properties of Water-Saturated Sandstones," *SPE Formation Evaluation*, (September 1988) 622.

12. Bech, N., Olsen., D., and Nielsen, C.M.: "Determination of oil/water saturation functions of chalk core plugs from flooding experiments," *SPE Reservoir Eval. and Eng. (2000) 3, 50.*

13. Olsen, D., Nielsen, C.M., and Bech, N.: "Variation in Fracture Permeability in Chalk Core Plugs", paper SPE 60302 presented at the 2000 SPE Rocky Mountain Regional/Low Permeability Reservoirs Symposium, Denver, Colorado, March 12-15, 2000.

14. Olsen, D., Topp, S., Steensgaard, A., Nørgaard, J.V., and Reffstrup, J.: "Quantitative 1D Saturation Profiles on Chalk by NMR", *Mag. Res. Imag. (1996) 14, 847.*

15. *ECLIPSE 100*, 99A Release, Intera Information Technologies Ltd., Highlands Farm, Henley-on-Thames, Oxfordshire, U.K.

16. Ovens, J.E.V., Larsen, F.P., Cowie, D.R.: "Making Sense of Water Injection Fractures in The Dan Field," *SPE Reservoir and Engineering (1998), 1,6,556.*

TABLE 1 – Fluid Data @ 20°c		
Fluid	Density (g/ml)	Viscosity (cp)
D_2O-brine	1.148	1.38
H_2O-brine	1.045	1.12
n-decane	0.730	0.92

The D_2O-brine viscosity is calculated, by multiplying the H_2O-brine viscosity with the viscosity ratio for D_2O/H_2O = 1.23 @ 25 °C.

TABLE 2 – NMR data sets					
	Image size (cm) [1]	Image size (pixels)	No of t_e values [2]	Repeti-tion time t_r (ms)	Acq. Time (min)
Type AW Axial images	9 x 5	512 x 32	3	2200	7.2
Type AO Axial images	9 x 5	512 x 32	3	10000	32
Type BO Axial images	9 x 5	512 x 32	3	5100	16.5

Note 1. All images have a slice thickness of 0.6 cm.
Note 2. Minimum t_e for all images was 7.1 ms.

TABLE 3 - Plug M16I Simulation Grid					
n_x	=	62	Δx	=	0.1175	cm
n_y	=	25	Δy_1	=	0.0025	cm
			Δy_2	=	0.0036	cm
			Δy_3	=	0.0053	cm
			Δy_4	=	0.0077	cm
			Δy_5	=	0.0113	cm
			Δy_6	=	0.0164	cm
			Δy_7	=	0.0240	cm
			Δy_8	=	0.0349	cm
			Δy_9	=	0.0509	cm
			Δy_{10}	=	0.0742	cm
			Δy_{11-25}	=	0.1108	cm
n_z	=	16	Δz	=	0.118125	cm

TABLE 4 - Dimensions and Properties of Core Plug M16I					
Dimensions:			Rock properties:		
L_{plug}	=	7.05	cm	φ_m	=	0.318
d_{plug}	=	3.78	cm	φ_f	=	1.
a	=	0.005	cm	k_m	=	1.94	mD
				k_f	=	27882	mD
Fluid properties:				C_{rock}	=	1.76 E-3	1/bar
C_w	=	4.48 E-5	1/bar	x_{blck1}	=	3.16	cm
C_o	=	1.16 E-4	1/bar	x_{blck2}	=	5.51	cm
				k_{blck1}	=	1464	mD
				k_{blck2}	=	891	mD
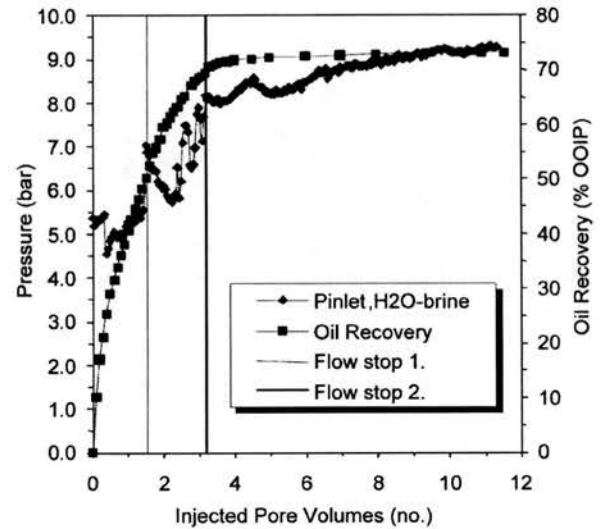
Fig. 1 - Production data. Measured inlet pressure and oil recovery.

Cumulative injected H₂O in pore volumes:

| PV = 0 | PV = 1.49 | PV = 3.04 | PV = 11.3 |

Normal water, H₂O, black: S_{H2O}=0 %, white: S_{H2O}=100 %.

Heavy water, D₂O, black: S_{D2O}=0 %, white: S_{D2O}=50 %.

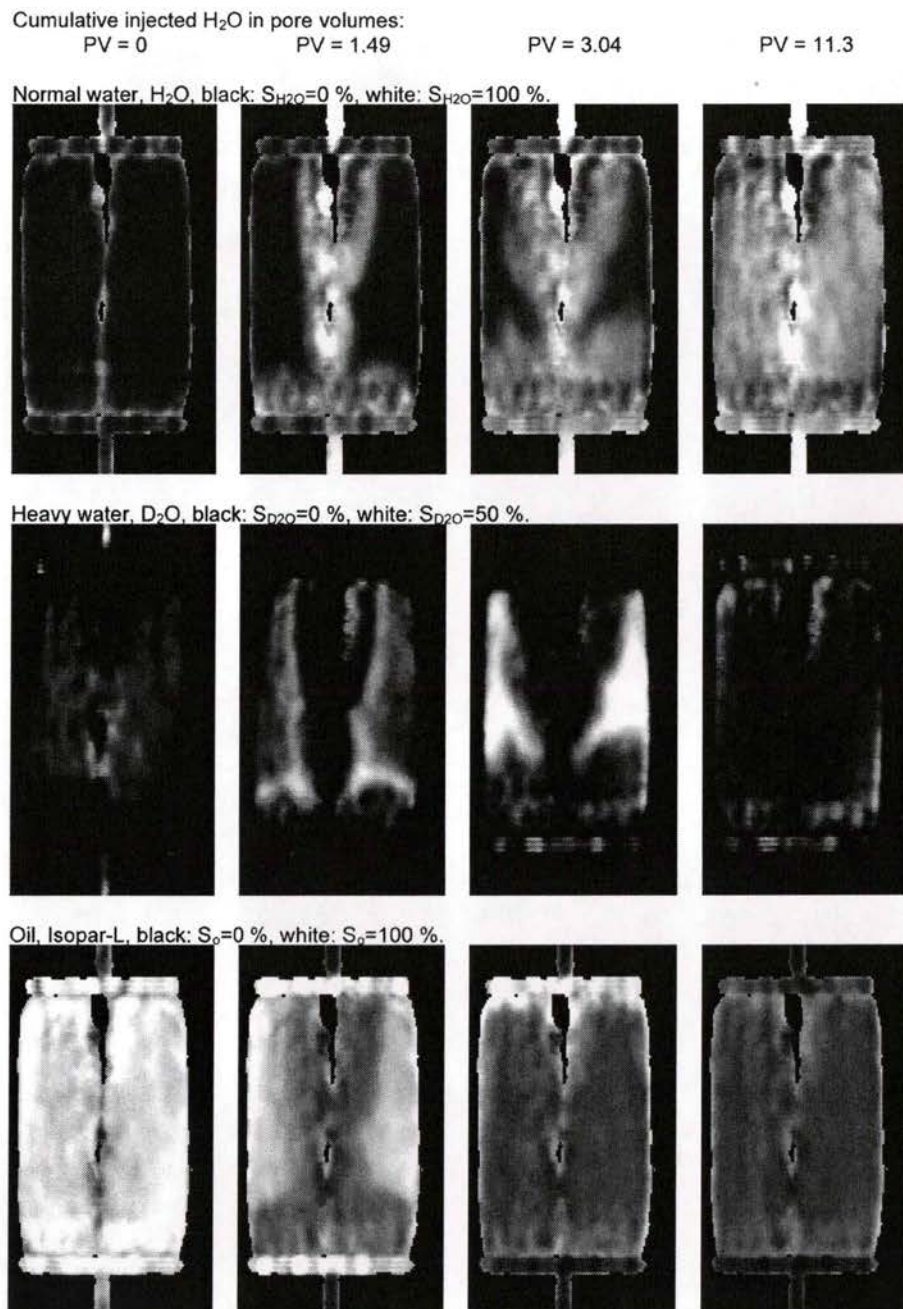Oil, Isopar-L, black: S_o=0 %, white: S_o=100 %.

Fig. 2 - Saturation model showing progression of the flooding experiment. The images represent an axial slice through the sample perpendicular to the fracture. The trace of the fracture is vertical in the centre of the sample. The flow is from the bottom towards the top of the images. Field of view is 9 x 5 cm. Slice thickness is 0.6 cm. Fluid saturations are represented by a linear grey scale as indicated above each fluid cartoon.
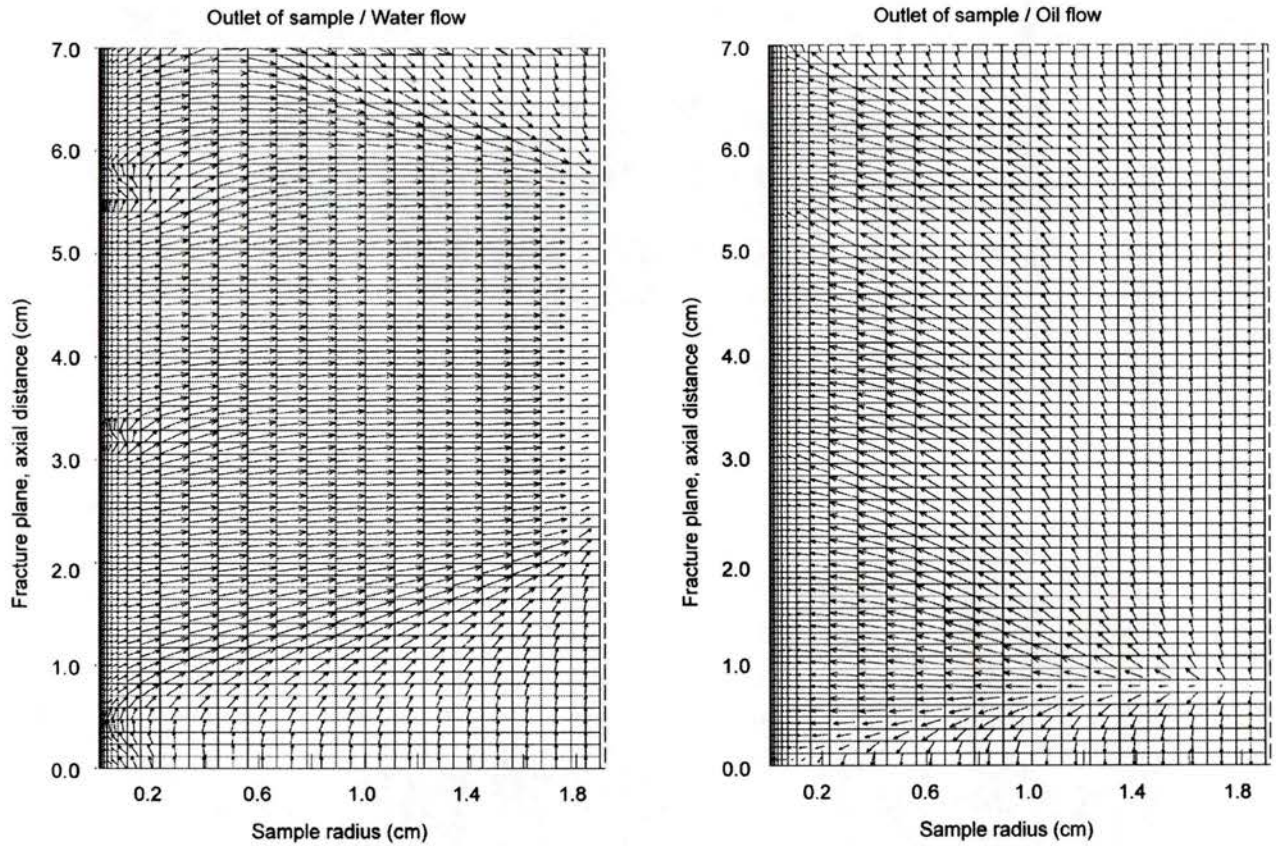
Fig. 3 – Simulated water and oil flow patterns after injection of 1.49 pore volumes.
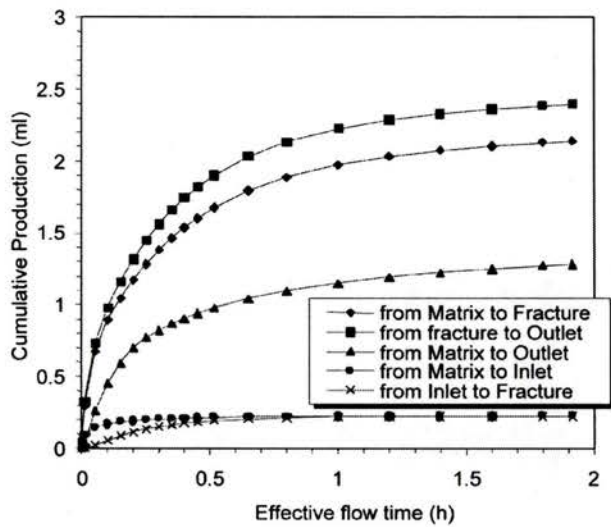
Fig. 4 – Simulated mode of oil production from sample.
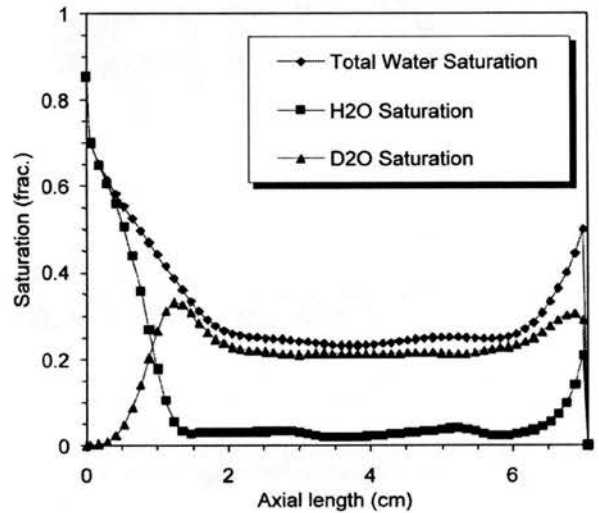
Fig. 5 – Simulated axial water saturation after injection of 1.49 pore volumes.
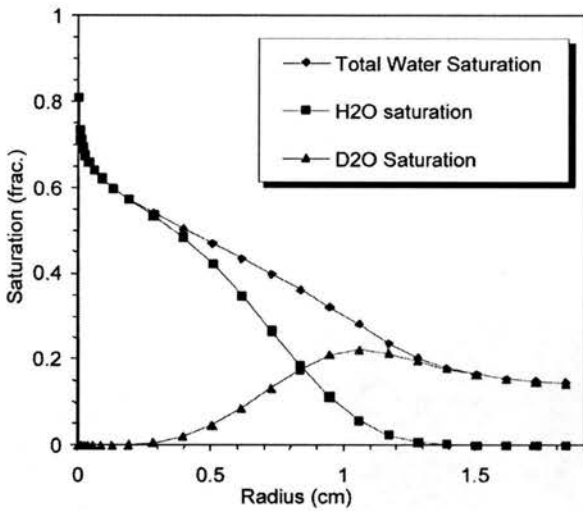
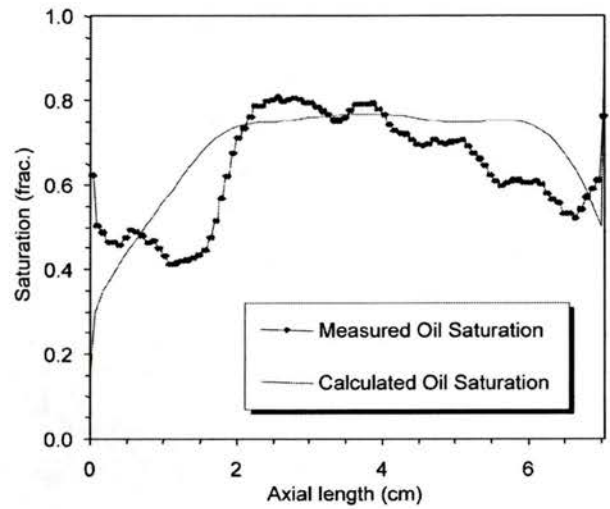Fig. 6 – Simulated radial water saturation after injection of 1.49 pore volumes.

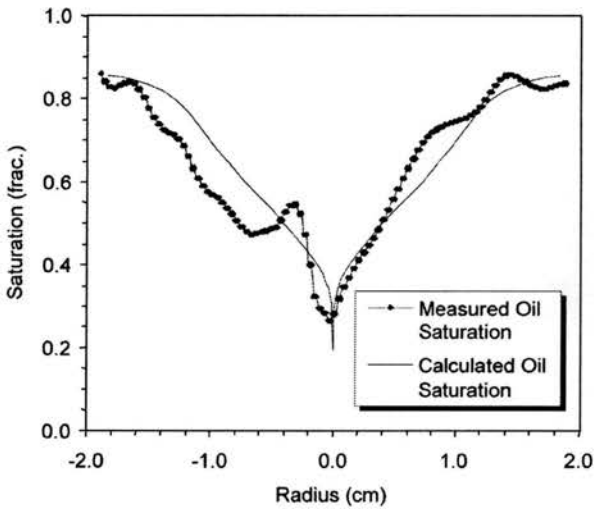Fig. 7 – Axial oil saturation after injection of 1.49 pore volumes.

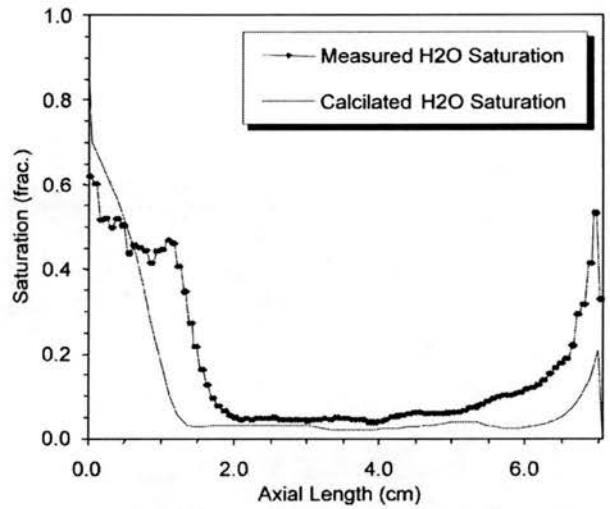Fig. 8 – Radial oil saturation after injection of 1.49 pore volumes.

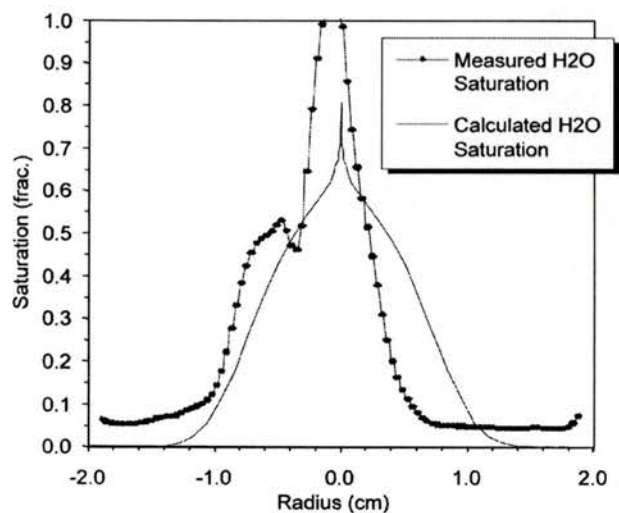Fig. 9 – Axial H₂O saturation after injection of 1.49 pore volumes.

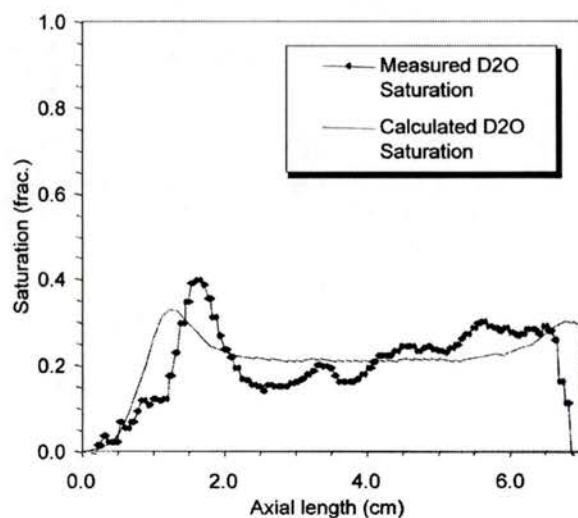Fig. 10 – Radial H_2O saturation after injection of 1.49 pore volumes.

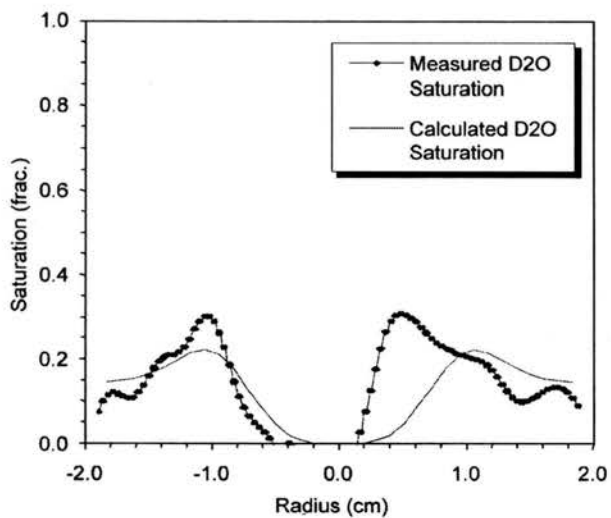Fig. 11 - Axial D_2O saturation after injection of 1.49 pore volumes.

Fig. 12 - Radial D_2O saturation after injection of 1.49 pore volumes.

Appendix C

Olsen, Nielsen & Bech, *SPE paper 60302, presented at the SPE Rocky Mountain Regional/Low Permeability Reservoirs Symposium 12-15 March 2000, Denver, Colorado, 13 pp, 2000.*

SPE 60302

Variation in Fracture Permeability in Chalk Core Plugs

D. Olsen, SPE, Geological Survey of Denmark and Greenland; C.M. Nielsen, Geological Survey of Denmark and Greenland; N. Bech, SPE, Geological Survey of Denmark and Greenland

Abstract

A miscible displacement experiment where D_2O brine was displaced by H_2O brine was conducted on a North Sea chalk sample with an induced fracture. The experiment was monitored by a 2D NMR technique. Differential pressure and production of D_2O were logged.

The displacement process was a combination of a piston-like displacement proceeding from the inlet end plane, and a displacement proceeding from the fracture into the matrix. NMR images show large axial variations in the amount of fluid transport across the fracture-matrix boundaries, indicating the presence of a significant permeability variation along the fracture.

The variation in fracture and matrix permeabilities are determined numerically by matching measured and calculated pressure drops, H_2O/D_2O concentration profiles and cumulative production. An ECLIPSE model with a fracture containing two partial blockages closely simulates the concentration profiles and the production. Calculated results indicate that the permeability at the blockages is below one tenth of the fracture permeability. The pressure drop across the plug increases with time indicating that the degree of fracture blockage is growing with time.

Introduction

Flow in fractures, whether naturally occurring or artificial, is an important mechanism in the production of many low permeability hydrocarbon reservoirs[1,2,3]. In modeling fracture flow it is important to know the permeability of the fracture. The present work presents an experimental study of a core plug with an induced fracture where the fracture permeability has a large variation along the fracture. The study uses a miscible fluid system H_2O / D_2O to enable determination of permeability without unwanted effects arising from relative permeability and capillary pressure. The experiment is monitored by Nuclear Magnetic Resonance (NMR) imaging.

A spin echo NMR sequence was used to acquire the NMR images. Other workers have used relaxation weighted NMR sequences. Chen et al.[4] used inversion recovery to discriminate between signal from either the matrix or the fracture. Whereas Kumar et al.[5] used a spin-spin relaxation technique to suppress the matrix signal, which enabled them to calculate a spatial aperture distribution.

The absolute permeabilities of the plug matrix and fracture are determined by matching calculated and measured H_2O concentration profiles, total pressure drop and cumulative D_2O production.

Experiment description and methods

The miscible displacement of D_2O with H_2O is monitored with a 2D NMR imaging technique. At the resonance frequency used herein no NMR signal will be acquired from the D_2O phase, whereas the protons in the H_2O phase will induce signal. The fluids were doped with $Ni(NO_3)_2$ to achieve a fast NMR data acquisition. An experimental schedule with intermittent flow was used, where high quality NMR data were acquired during periods without flow, while data of lower quality were acquired during the flow periods.

Sample Material. The rock material used is a chalk sample named M16I of Maastrichtian age from the Dan field in the Danish sector of the North Sea. The sample has good NMR characteristics, Table 1. It is homogeneous, except for minor hairlines, minor trace fossils, and a faint bedding plane. Prior to the flooding experiment the sample was cleaned by Soxhlet extraction with methanol and toluene. An artificial fracture was mechanically induced in the axial direction following the bedding plane, dividing the sample into two parts almost equal in size. A Brazilian test[6] like apparatus was used. A diametrical compressive stress field directed through the visible layering and along the length of the sample supported the failure to occur along the bedding plane. The sample was dry when fractured. Before reassembling the sample the fracture aperture

was adjusted by applying a thin layer of quartz grains onto the fracture plane. The size of the quartz grains is in the range of 63 – 75 μm. The sample was initially saturated with a D_2O-brine. The sample is strongly water wet. Basic parameters for the sample are given in Table 1.

Fluid Data. The fluid system used for the miscible displacement experiment is D_2O–brine and H_2O-brine. The salinity of the brines is 0.17 M NaCl. For NMR purpose the fluids were doped with $5*10^{-3}$ M $Ni(NO_3)_2$. The D_2O used was 99.9 % in purity but to allow proper shimming of the static magnetic field of the NMR scanner it was adjusted to 99.5 % with H_2O. In order to avoid any free gas phase both brines were degassed before use. The density of D_2O-brine and H_2O-brine at 20°C was 1.109 g/ml and 1.002 g/ml, respectively. The density was measured with a PAAR digital Density meter DMA 35. The viscosity ratio for the D_2O / H_2O brine was taken as the viscosity ratio for D_2O / H_2O @ 25 °C equal to 1.23[7].

Miscible flooding experiment. Initially the fractured sample is fully saturated with D_2O-brine. It is placed in a non-magnetic Hassler type coreholder allowing for NMR measurements. N_2 gas is used as confining media. H_2O-brine is injected at constant rate displacing the D_2O phase while the injection pressure is recorded, **Fig. 1**. The production of D_2O-brine is determined as the change in density of the produced brine as function of number of injected pore volumes, **Fig. 2**. During the intervals of injection fast NMR measurements were acquired to follow the progressive displacement front, **Figs. 4 and 5**. At three times during the experiment the injection was stopped and high quality quantitative 2D NMR measurements were acquired, **Fig. 3**. During one of the intervals of no flow a duplicate acquisition shows that the displacement front was virtually unchanged in the time interval of 16 minutes between the two acquisitions and at the scale of the image resolution.

NMR Hardware. A 4.7 T SISCO experimental NMR scanner was used for the NMR work. It was equipped with a 13 cm diameter insert gradient set, capable of producing magnetic gradient up to 100 mT/m along any of three orthogonal directions. Gradient rise rate was $2.7*10^5$ mT/m*s. A Radio Frequency coil of slotted tube resonator design with good signal homogeneity until a maximum length of 9 cm was used.

NMR Pulse sequence. An ordinary 2D spin echo pulse sequence was used. The NMR signals that were acquired came from only one phase, H_2O, and separation of signals with different chemical shift was therefore not necessary.

NMR Data sets. Three types of image data were acquired during the experiment, termed Type A, Type B and Type C, cf. Table 2.

Axial images Type A. Five data sets of axial images were acquired during the experiment, Fig. 3, where a technique of arrayed acquisition was used. In this technique a number of images corresponding to an array of t_e values are acquired simultaneously, allowing correction for signal relaxation [8]. The images in Fig. 3 are M0 maps of signal intensity at t_e equal to zero. A drawback of this method is that is relatively slow. In the present work it required 26 minutes to obtain a data set of reasonable resolution. This circumstance required the fluid flow to be stopped during data acquisition, which was done at three instances during the experiment. The remaining two Type A data sets were acquired before the start and after the end of the flooding. A single-exponential model was used for relaxation correction[9].

Axial images Type B. Eight images were acquired during the experiment as images using a single t_e value, Fig. 4. This type of images is termed "single-shot images" as opposed to the arrayed-t_e images. The benefit compared to the arrayed-t_e images is a faster acquisition. The acquisition time for the single-shot images was reduced by a factor of forty to 40 seconds, allowing tracking of the displacement while the flooding was in progress. The cost of this comparatively fast data acquisition was the inability to correct for signal relaxation, a 60 % saturation of the NMR signal, and a reduction in spatial resolution. Therefore, the Type B images are strictly speaking not quantitative. Comparison with the quantitative Type A maps, however, reveals only minor differences, which can mainly be attributed to the different spatial resolution. Compare for example the map PV=1.62 of Fig. 3 and the image PV=1.59 of Fig. 4. Because the Type B images give a much better time resolution of the displacement process, it was decided to use them for the ECLIPSE simulations instead of the Type A images.

Transaxial images Type C. A total of 12 transaxial images were acquired during the experiment using the "single-shot" technique, Fig. 5. They were acquired while the flooding was in progress. The transaxial images were acquired at four places along the sample length to give some information about the fluid flow outside the axial image plane of the Type A and B images. Like the Type B images, the Type C images were not corrected for relaxation.

Image description. Figs. 3 and 4 show how the H_2O gradually enters the sample until it is completely flooded. Part of the flooding takes place as a piston-like displacement progressing from the inlet end, and part of it occurs from the fracture. The latter displacement is much more irregular than expected, and the displacement front takes the shape of a peapod. At two positions along the fracture the H_2O is forced into the matrix of the sample. This is interpreted to be caused by partial blockages in the fracture, where the fracture flow is forced into the matrix of the sample. Along other parts of the fracture little H_2O is forced into the matrix, e.g. close to the outlet and between the two blockages. These parts are interpreted to represent fracture segments with unobstructed flow. Fracture segments with intermediate characteristics appear to exist close to the inlet end, but for the present work a simplified model consisting of a fracture with two partial blockages is adopted.

Parameter Estimation Technique

The miscible flooding experiment is simulated by means of the ECLIPSE simulator[10] and the matrix and fracture permeabilities of the plug are adjusted so that calculated and measured H_2O/D_2O concentration profiles, total pressure drop and cumulative D_2O production agree.

A model with a vertical fracture along the sample axis is used. The fracture is assumed to have constant aperture, and width equal to the sample diameter. It is further assumed to contain two blockages of reduced permeability covering the whole sample width. The two blockages can be modelled by reducing the permeabilities in the affected grid cells.

The problem is thus formulated with four unknowns:

- The matrix permeability, k_m
- The fracture permeability, k_f
- The two fracture blockage permeabilities, k_{blck1} and k_{blck2}

The concentration profiles, which are matched, are taken along three lines as indicated in **Fig. 6**. Profile 1 is an axial profile at a distance of about 0.6 R_{plug} from the axis. Profile 2 is chosen perpendicular to the axis at a location close to that of the second blockage. Profile 3 is also chosen perpendicular to the axis but at a location close to that of the first blockage.

The four permeabilities are determined so that they minimise the following least squares objective function

$$J(k) = \sum_{i=1}^{n_x} \left(C1_{H_2O}^C(x_i) - C1_{H_2O}^m(x_i) \right)^2 F_{w1}^2 +$$

$$\sum_{j=1}^{n_y} \left(C2_{H_2O}^C(y_j) - C2_{H_2O}^m(y_j) \right)^2 F_{w2}^2 +$$

$$\sum_{j=1}^{n_y} \left(C3_{H_2O}^C(y_j) - C3_{H_2O}^m(y_j) \right)^2 F_{w3}^2 +$$

$$\left(\Delta p_T^C - \Delta p_T^m \right)^2 F_{w4}^2 + \left(Q_{D_2O}^C - Q_{D_2O}^m \right)^2 F_{w5}^2 \quad \dots\dots\dots (1)$$

The squared residuals are scaled by means of weight factors, F_w to make their contribution to the objective function similar in size. The minimization is carried out by means of the least-square solver MI0L2[11]. The extraction of results from the ECLIPSE output file is performed by means of software developed by Frandsen[12].

Test of Parameter Estimation Technique.

The parameter estimation technique has been tested on a numerically defined fractured core plug, i.e. a core plug with prescribed permeabilities. The cylindrical core plug contains a single fracture plane through the axis. The plug is saturated with water and at time zero water containing a tracer is injected at the inlet at a fixed rate. The tracer distribution, total pressure drop and cumulative D_2O production calculated after injection of 4.9 pore volumes

are considered measured data for this synthetic case. The concentration profiles, which are matched, are taken along three lines as described above. The dimensions and properties of the synthetic plug and the water are given in Table 3.

The flow pattern in the plug is symmetric with respect to the fracture plane and a plane perpendicular to the fracture plane through the plug axis. Consequently, only one quarter of the plug is considered. The plug and its bounding inlet and outlet chambers are modelled by means of a 3 dimensional Cartesian grid with $n_x = 50$, $n_y = 14$ and $n_z = 8$. The inlet and outlet chambers are modelled by the grid planes $i = 1$ and $i = n_x$, respectively. The core plug thus contains 48*14*8 grid cells. The two fracture blockages are located in the grid planes $(23,1,k)$ and $(39,1,k)$, respectively where $k = 1$, n_z. The grid cell dimensions and the initial and operating conditions are given in Table 4.

The ECLIPSE model described above was run with the synthetic core plug data until 4.9 pore volumes had been injected. Tracer concentration profiles were recorded along the following three lines:

1. $(i, j, k) = (\ i, 12, 1)$, $i = 1, n_x$
2. $(i, j, k) = (22,\ j, 1)$, $j = 1, n_y$
3. $(i, j, k) = (37,\ j, 1)$, $j = 1, n_y$

The three profiles are shown in **Figs. 7 - 9**. Note the reduced scale in Fig. 9. The radial distribution of the H_2O concentration Profile 3 is close to being uniform equal to one because the axially advancing H_2O front has almost passed the axial location of Profile 3 which is 3.16 cm (cf. Fig. 6). One might expect the radial concentration distributions to be horizontal for large values of the lateral coordinate, y where the influence of the blockages is not felt. The reason why they are not is that the injected water is not distributed equally over the inlet cross section. I.e. the inlet velocity is not uniform over the cross section. However, the variation is small.

The matrix and fracture permeabilities of the plug are adjusted so that calculated and measured H_2O/D_2O concentration profiles, total pressure drop and cumulative D_2O production agree. The following initial guesses were applied:

- Matrix permeability, k_m: 1. mD
- Fracture permeability, k_f: 3000. mD
- Fracture blockage 1 permeability, k_{blck1}:   300. mD
- Fracture blockage 2 permeability, k_{blck2}:   300. mD

The permeabilities obtained from the optimization are equal to the values specified for the synthetic core plug. This demonstrates that the procedure for calculating these permeabilities from total concentration profiles, total pressure drop and cumulative D_2O production is valid for ideal synthetic data. The matching of the concentration profiles is shown in Figs. 7 - 9. Also shown are the calculated profiles corresponding to the initial guess.

Results

The measured inlet pressure and production of D_2O-brine is shown in **Figs. 1, 2** and **10** for sample M16I. The injection rate was 100 ml/h in the first flood interval and then raised to 150 ml/h in the subsequent intervals. During the intervals of constant rate injection the measured inlet pressure gradually increases. The increase in inlet pressure is considered to be the effect of blockage growth in the fracture. The production of D_2O-brine is determined from the density difference between D_2O-brine and H_2O-brine. It is seen from Fig. 2 that the fracture is flooded almost instantaneously, whereas almost 15 pore volumes are flooded before a significantly H_2O-brine breakthrough occurs from the matrix.

Results for Core Plug M16I. The dimensions and properties of plug M16I are given in Table 5. The distances from the inlet to the two blockages are measured from Fig. 4. It is assumed that the fracture blockages are line blockages of length one plug diameter.

The M16I permeabilities are determined by history matching the total pressure drop, the cumulative D_2O production and three concentration profiles:

- Profile 1 is recorded along the plug at a radial distance of 1.12 cm from the plug axis.
- Profile 2 is recorded along the plug radius at a distance of 5.36 cm from the plug inlet.
- Profile 3 is recorded along the plug radius at a distance of 3.21 cm from the plug inlet.

Each of the three measured signal intensity profiles is converted to normalized H_2O concentration profiles as follows, **Figs. 11-13**:

- A maximum level is determined
- All values corresponding to pixels closer to the inlet (in case of the axial profile) or the fracture (in case of the radial profiles) are put equal to the maximum value. This is done in order to avoid unnecessary trouble during the optimization calculation arizing from the fact that the simulated concentrations can never increase in the positive coordinate directions.
- Finally, all values are normalized so that the maximum values are equal to one.

The profiles which have been matched were measured after injection of 4.9 pore volumes.

Simulation model. As in case of the synthetic plug only one water phase is considered and the light water is characterised by a tracer. Also, only one quarter of the core plug is considered and the plug and the inlet and outlet chambers are modelled by means of a 3 dimensional Cartesian grid. Initial calculations performed with the grid used to model the synthetic core plug described above showed that the radial discre-

tization was too coarse to capture the measured concentration profiles.

Therefore a new more detailed grid was set-up with $(n_x, n_y, n_z) = (62, 25, 16)$, see Table 6. The inlet and outlet chambers are modelled by the grid planes $i = 1$ and $i = n_x$, respectively. The core plug thus contains $60*25*16 = 24000$ grid cells.

Initial and operating conditions are given in Table 7. The flow rates imposed in the simulation differ from the experimental flow rates because the 3D Cartesian cross section of the plug in the simulation model is a little different from the true cross section of the cylindrical core plug. In order to obtain the same inlet flow velocities in simulation and experiment the simulation flow rate is modified (cf. Eqs. 4-5). As seen in Fig. 1 the flooding was stopped for certain time intervals during the experiment. During these periods with no injection the flow pattern in the plug is considered stagnant and these intervals are not modelled.

In preliminary calculations one injection well was placed in cell $(i, j, k) = (1, 1, 1)$. It turned out, however that the velocity of the water injected into the core plug in this way was very non-uniform over the plug cross section. In order to create a more uniform inlet velocity the water injection was carried out through n_y wells completed in each of the n_z layers. The flow rate injected into each well was adjusted as follows to yield a uniform inlet velocity:

$$q_{inj.j} = f_j q_{ECL} \dots\dots\dots\dots(2)$$

where

$$f_j = \frac{\Delta y_j n_{z\,j}}{\sum_{j=1}^{n_y} \Delta y_j n_{z\,j}} \dots\dots\dots\dots(3)$$

$$q_{ECL} = A_{rat} q_{exp} \dots\dots\dots\dots(4)$$

$$A_{rat} = \frac{A_{cross}}{A_{plug}} \dots\dots\dots\dots(5)$$

The following values apply:

$$A_{plug} = 2.8055 \text{ cm}^2 \dots\dots\dots\dots(6)$$

$$A_{cross} = 2.8261 \text{ cm}^2 \dots\dots\dots\dots(7)$$

$$A_{rat} = 1.00732 \dots\dots\dots\dots(8)$$

The flow rates injected into each of the n_y wells are given in Table 8. Note that only one quarter of the plug is modeled.

History matching the core plug M16I permeabilities. The matrix and fracture permeabilities of the plug are adjusted so that calculated and measured concentration profiles, total pressure drop and cumulative D_2O production agree. There is one problem, however: The pressure drop across the core plug increases during periods with constant flow rate. It is not clear

why this happens. It could be due to migration of fines that are deposited at the blockage locations. The effect would be to increase the resistance to flow. Any non-Darcy effect caused by the relative high flow rate through the fracture was checked by an additional flow experiment. The flow rate was gradually increased from no flow to a flow rate of 175 ml/h. **Fig 14** shows how the measured pressure drop varies linearly with the injection rate. In the present calculation we use the pressure drop $\Delta p_T = 1.03$ bar measured after injection of 4.9 pore volumes.

The initial guesses and calculated results are given in Table 9. It is seen that the variation of the permeability in the fracture is very large ranging from approximately from 900 mD at the largest blockage to 28000 mD in the undisturbed fracture. The matrix permeability is estimated to about 2 mD a figure which has been confirmed by independent measurements. The matches to the measured H_2O concentration profiles, total pressure drop and cumulative D_2O production are shown in Figs. 11 – 13 and Table 10. It is seen that the calculated parameters are pretty close to the measured data.

Discussion

In the simulation it has been assumed that the fracture is vertical and aligned along the plug axis, that the width is constant and the height equal to the plug diameter. Figs. 4and 5 show, however, that this is not exactly the case. The centre of the fracture is not everywhere on the plug axis (Fig. 4) and the fracture does not everywhere extend over the entire plug diameter (Fig. 5). The blockages of the model occupy the fracture in the whole sample width. This is justified by the transaxial images of Fig. 5, which shows a fairly even progression of the displacement front from the fracture. Close to the outlet the situation is more complicated, but this is not included in the model. The assumptions do appear to be reasonable considering the relatively good match between measurements and calculations.

Due to the existence of the two blockages the variation of the fracture permeability is very large. Moreover, the pressure drop across the plug increases with time indicating that the degree of fracture blockage is growing with time. If we assume that the increase in pressure drop over the core plug is due to fines deposition at the two blockage locations and that the ratio k_{blck1}/k_{blck2} remains fixed then it is possible to compute the increasing resistance to flow caused by the blockages. The result is given in **Fig. 15**. It is seen that the blockage resistance growths by a factor of almost 5. compared to the initial value. The initial values of the fracture blockages are estimated to $k_{blck1} = 3455$. and $k_{blck2} = 2103$. **Fig. 15** also shows that the growth in the blockage resistance increases with flow rate which is 100 ml/hr for $t < 24$ min and 150 ml/hr elsewhere.

In the above calculation of the blockage resistances no account is taken for the viscosity ratio being 1.23 times greater than unity for the displacement process. The effect of neglecting the higher viscosity of the D_2O is to reduce the calculated permeabilities. With the assumption of piston-like displacement the viscosity could be modelled with an effective viscosity as being the average of the two viscosities weighted with saturation as proposed by Lenormand et al.[13] for modelling flow in micromodels. Calculations show that by doing so the computed permeabilities are simply increased by the ratio between the new average viscosity and old H_2O viscosity. In other words, the permeabilities to H_2O are unchanged.

Conclusions

The miscible displacement of D_2O with H_2O in a plug sample with a single axial fracture plane has been visualized by a 2D NMRI technique and modelled by a reservoir simulator.

The artificially induced fracture contained two blockages which forced the fracture flow into the matrix. The matrix and fracture permeabilities of the plug were determined by matching calculated and measured H_2O concentration profiles, total pressure drop and cumulative D_2O production.

The permeability of the blockages is below one tenth of the fracture permeability.

The measured pressure drop across the plug increases with time indicating that the degree of fracture blockage is growing with time. It is suggested that the increase is due to fines deposition and the resulting increase in blockage resistance is calculated.

Acknowledgments

Nomenclature

A	=	flow area, cm^2
a	=	fracture aperture, µm
$Arat$	=	area ratio
C	=	compressibility, bar^{-1}
$C1$	=	H_2O concentration Profile 1
$C2$	=	H_2O concentration Profile 2
$C3$	=	H_2O concentration Profile 3
D	=	plug diameter, cm
f	=	geometrical ratio
F_w	=	weight factor
J	=	objective function
k	=	absolute permeability, mD
L	=	length of core sample, cm
n	=	number of grid cells
p	=	pressure, bar
q	=	flow rate, ml/h
Q	=	cumulative flow, ml
R	=	plug radius, cm
T_1	=	spin-lattice constant, ms
T_2	=	spin-spin constant, ms
t	=	time, min
t_e	=	echo time, ms

x	=	axial coordinate, cm
y	=	lateral coordinate, cm
z	=	vertical coordinate, cm
φ	=	porosity, fraction
μ	=	viscosity, cp
ρ	=	density, g/cm^3

Subscripts

|		
$blck1$	=	fracture blockage no. 1
$blck2$	=	fracture blockage no. 2
$cross$	=	cross section
D_2O	=	deuterium
ECL	=	ECLIPSE
exp	=	experiment
f	=	fracture
H_2O	=	light water
i	=	x-direction coordinate index
inj	=	injection
j	=	y-direction coordinate index
k	=	z-direction coordinate index
m	=	matrix
$plug$	=	core plug
$rock$	=	matrix rock
T	=	total
x	=	refers to x-direction
y	=	refers to y-direction
z	=	refers to z-direction
w	=	water

Superscripts

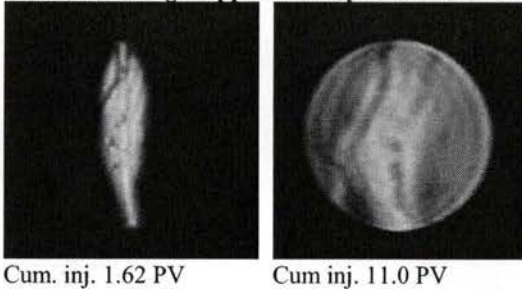|		
C	=	calculated
m	=	measured

References

1. Firoozabadi, A.: "Production performance of fractured reservoirs and basic recovery mechanisms," *SCA workshop Hamburg, Germany, October 13-14, 1998.*
2. Fritsen, A., and Corrigan, T.: "Establishment of a geological fracture model for dual porosity simulations on the Ekofisk field," In: Buller, Berg, Hjelmeland, Kleppe, Torsæter, and Aasen (eds.): *North Sea Oil and Gas Reservoirs II*, Graham & Trotman, 1990, 173.
3. Ovens, J.E.V., Larsen, F.P., and Cowie, D.R.: "Making sense of water injection Fractures in the Dan field," *SPE Reservoir Evaluation and Engineering (1998), 1,6, 556.*
4. Chen, S., Yao, X., Qiao, J., Watson, A.T.: "MRI Investigation of Fractures and Multiphase Flow in Fractured Media," *AICHE J. (1996) 42, 3 820.*
5. Kumar, A.T.A., Majors, P., Rossen, W.: "Measurement of Aperture and Multiphase Flow in Fractures With NMR Imaging," *SPE Formation Evaluation, (June 1997) 101.*
6. Tiab, D., Donaldson, E.C.: *Petrophysics – Theory and Practice of Measuring Reservoir Rock and Fluid Transporet Properties,* Gulf Publishing Company, Texas, (1996).
7. *THE MERCK INDEX,* Merck & Co., Inc., Rahway, N.J., USA, 9. Ed. (1976).
8. Edelstein, W.A., Vinegar, H.J., Tutunjian, P.N., Roemer, P.B, and Mueller, O.M.: "NMR imaging for core analysis," paper SPE 18272 presented at the 1988 SPE Annual Technical Conference and Exhibition, Houston, Texas, October 2-5, 1988.
9. Bech, N., Olsen., D., and Nielsen, C.M.: "Determination of oil/water saturation functions of chalk core plugs from flooding experiments," *SPE Reservoir Evaluation and Engineering (2000), 3.*
10. *ECLIPSE 100,* 95A Release, Intera Information Technologies Ltd., Highlands Farm, Henley-on-Thames, Oxfordshire, U.K.
11. Madsen, K., Hegelund, P., Hansen, P.C.: "Non-gradient Subroutines for Non-Linear Optimization," Report Ni-91-05, Institute for Numerical Analysis, Technical University of Denmark, June 1991.
12. Frandsen, P.E.: "SIMPE - Small Interface Module for Parameter Estimation," Geological Survey of Denmark and Greenland Report (1998) 61.
13. Lenormand, R., Touboul, E., Zarcone, C.: "Numerical models and experiments on immiscible displacements in porous media," *J. Fluid Mech. (1988) 189, 165.*
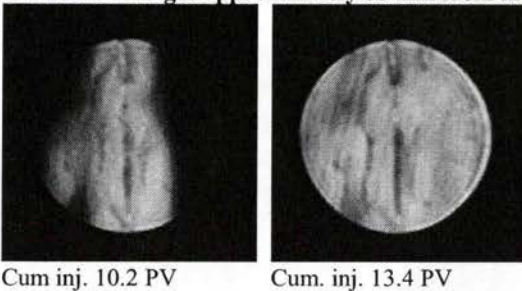
Transaxial images approximately 8 mm from inlet end.

Cum. inj. 0.27 PV   Cum. inj. 0.79 PV   Cum. inj. 1.46 PV   Cum. inj. 12.6 PV
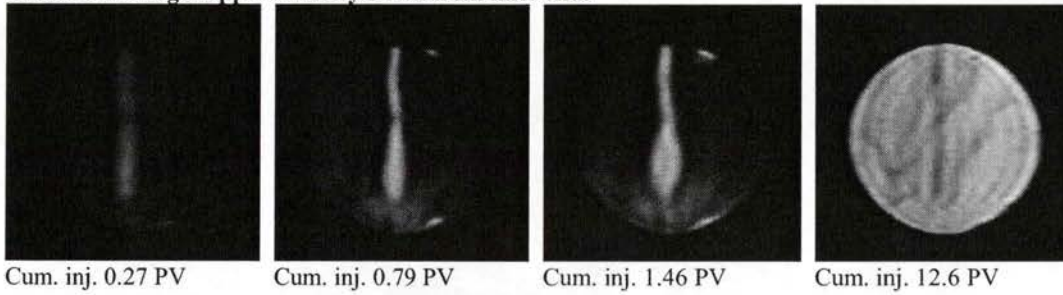
Transaxial images approximately 35 from inlet end.

Cum. inj. 1.62 PV   Cum inj. 11.0 PV

Transaxial images approximately 55 mm from inlet end.

Cum inj. 10.2 PV   Cum. inj. 13.4 PV

Transaxial image approximately 64 mm form inlet end.

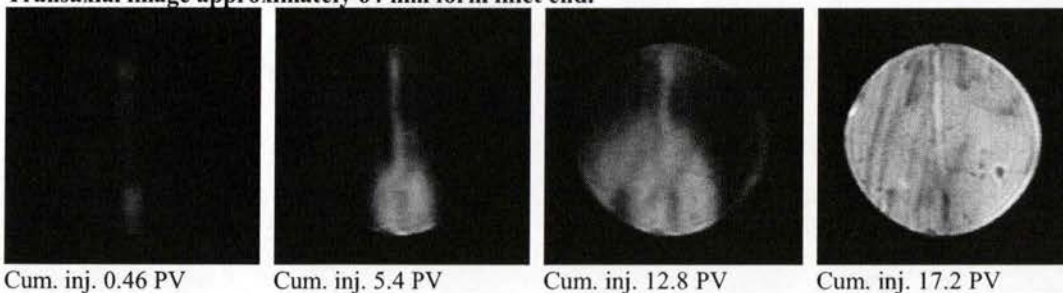Cum. inj. 0.46 PV   Cum. inj. 5.4 PV   Cum. inj. 12.8 PV   Cum. inj. 17.2 PV

Fig. 5. Type C NMR images showing progression of the flooding experiment. The images represents transaxial slices through the sample at four different positions along the sample length. The trace of the fracture is vertical through the sample centre. Flow is perpendicular to the image slices. Field of view is 5 x 5 cm. Slice thickness 0.45 cm. Signal intensities are represented by a linear grey scale with black=0 and white=0.020. Signal intensities are in arbitrary SISCO magnetisation units.
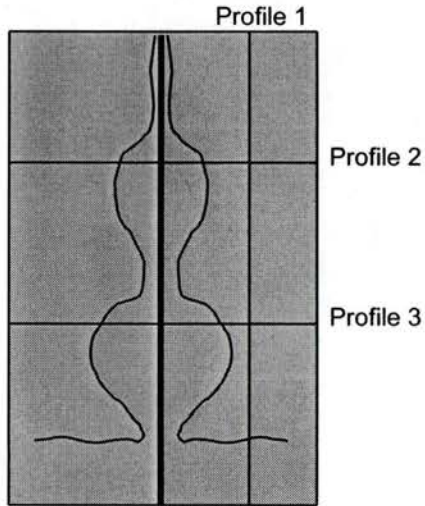
Fig. 6. H₂O/D₂O displacement experiment concentration distribution.
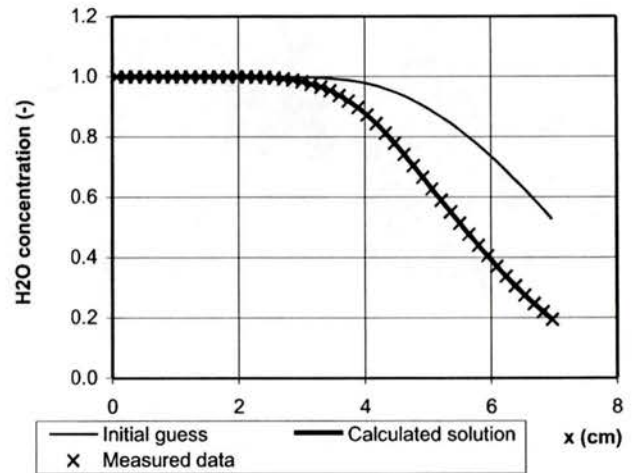

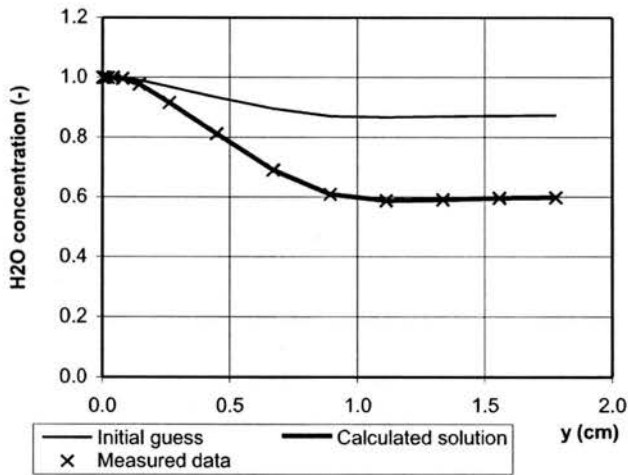Fig. 7. Synthetic core plug H₂O concentration, Profile 1.

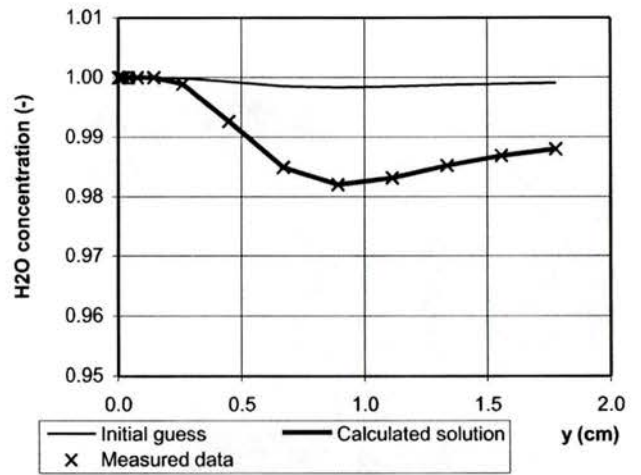Fig. 8. Synthetic core plug H₂O concentration, Profile 2.

Fig. 9. Synthetic core plug H₂O concentration, Profile 3.

TABLE 1 - Sample Parameters	
Sample id.	M16I
L	7.05 cm
D	3.78 cm
φ	0.318
k	2.0 mD
Estimated a	50 µm
NMR parameters of pore fluid H_2O @ 4.7 T:	
NMR linewidth	110 hz
T_1	259 ms
T_2	6 ms

TABLE 2 - NMR data sets					
	Image size (cm) [1]	Image size (voxel)	No. of t_e values [2]	Repetition time t_r (ms)	Acq. time (min)
Type A axial images	9 x 5	512 x 64	5	1200	26
Type B axial images	9 x 5	512 x 32	1	300	0.6
Type C transaxial images	5 x 5	512 x 32 [1]	1	300	0.6 [3]

Note 1. All images have a slice thickness of 0.45 cm.
Note 2. Minimum t_e for all images was 3.69 ms.
Note 3. The images at PV's 0.27 and 0.46 only had 512 x 16 voxels resulting in acq. time 0.3 min, while the images at PV's 1.62, 10.2, 13.4 and 17.2 had 512 x 64 voxels resulting in acq. time 1.2 min.
Note 2. Minimum t_e for all images was 3.69 ms.

TABLE 3 - Dimensions and Properties of Synthetic Core Plug	
Dimensions:	k_m = 1.5 mD
L_{plug} = 7.05 cm	k_f = 6000. mD
D_{plug} = 3.78 cm	k_{blck1} = 600. mD
a = 0.005 cm	k_{blck2} = 600. mD
Rock properties:	C_{rock} = 4.48_{10}-5 1/bar
x_{blck1} = 3.16 cm	Water properties:
x_{blck2} = 5.51 cm	C_w = 4.48_{10}-5 1/bar
φ_m = 0.318	ρ_w = 1.002 g/cm^3
φ_f = 1.	μ_w = 1.12 cp

TABLE 4 - Synthetic Plug Simulation Model		
Simulation Grid:		
n_x = 50	Δx	= 0.146875 cm
n_y = 14	Δy_1	= 0.0050 cm
	Δy_2	= 0.0088 cm
	Δy_3	= 0.0155 cm
	Δy_4	= 0.0273 cm
	Δy_5	= 0.0481 cm
	Δy_6	= 0.0847 cm
	Δy_7	= 0.1494 cm
	Δy_{8-14}	= 0.2216 cm
n_z = 8	Δz	= 0.23625 cm
Initial Conditions:		
Pressure: 1 bar everywhere		
Tracer concentration: One in inlet chamber and zero elsewhere		
Wells and Operating Conditions:		
Injector:	Producer:	
Location: Cell (1,1,1)	Location: Cell (50,1,1)	
Injection rate: 19.26 ml/hr	Bottom hole pressure: 0.95 bar	

TABLE 5 - Dimensions and Properties of Core Plug M16I	
Dimensions:	φ_m = 0.318
L_{plug} = 7.05 cm	φ_f = 1.
D_{plug} = 3.78 cm	C_{rock} = 4.48_{10}-5 1/bar
a = 0.005 cm	Water properties:
Rock properties:	C_w = 4.48_{10}-5 1/bar
x_{blck1} = 3.16 cm	ρ_w = 1.002 g/cm^3
x_{blck2} = 5.51 cm	μ_w = 1.12 cp

TABLE 6 - Plug M16I Simulation Grid		
n_x = 62	Δx	= 0.1175 cm
n_y = 25	Δy_1	= 0.0025 cm
	Δy_2	= 0.0036 cm
	Δy_3	= 0.0053 cm
	Δy_4	= 0.0077 cm
	Δy_5	= 0.0113 cm
	Δy_6	= 0.0164 cm
	Δy_7	= 0.0240 cm
	Δy_8	= 0.0349 cm
	Δy_9	= 0.0509 cm
	Δy_{10}	= 0.0742 cm
	Δy_{11-25}	= 0.1108 cm
n_z = 16	Δz	= 0.118125 cm

TABLE 7 - Plug M16I Initial and Operating Conditions				
Initial Conditions				
Pressure: 1 bar everywhere				
Tracer concentration: One in inlet chamber and zero elsewhere				
Wells and Operating Conditions:				
Injector:			Producer:	
Location: Cell (1,1,1)			Location: Cell (50,1,1)	
Time interval (min.)	Exp. flow rate (ml/hr)	ECLIPSE flow rate (ml/hr)		
0. – 24.	100.	100.7		
24. - 57.	150.	151.1	Bottom hole pressure: 0.95 bar	

TABLE 9 - M16I Permeabilities				
	k_m (mD)	k_f (mD)	k_{blck1} (mD)	k_{blck2} (mD)
Initial guess	1.5	6000.	600.	600.
Result	1.94	27882.	1464.	891.

TABLE 10 - M16I Cumulative D_2O Production and Total Pressure Drop		
	Total pressure drop (bar)	Cumulative D_2O production (ml)
Measured	1.03	11.30
Calculated	1.03	12.03

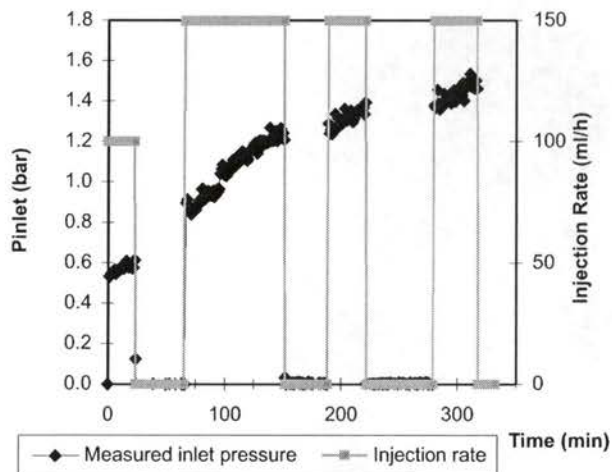| TABLE 8 - Plug M16I Injection Flow Rates			
		$q_{exp} = 100.$ $q_{ECL} = 100.7$	$q_{exp} = 150.$ $q_{ECL} = 151.1$
j	f_j	$q_{inj,j}$ (ml/hr)	$q_{inj,j}$ (ml/hr)
1	0.04210	0.04210	0.06316
2	0.06063	0.06063	0.09095
3	0.08926	0.08926	0.13389
4	0.12968	0.12968	0.19452
5	0.19031	0.19031	0.28547
6	0.27621	0.27621	0.41431
7	0.40420	0.40420	0.60630
8	0.58778	0.58778	0.88167
9	0.85725	0.85725	1.28587
10	1.24966	1.24966	1.87449
11	1.81891	1.81891	2.72837
12	1.86607	1.86607	2.79911
13	1.74944	1.74944	2.62416
14	1.74944	1.74944	2.62416
15	1.74944	1.74944	2.62416
16	1.63281	1.63281	2.44922
17	1.63281	1.63281	2.44922
18	1.51618	1.51618	2.27427
19	1.51618	1.51618	2.27427
20	1.39955	1.39955	2.09933
21	1.28292	1.28292	1.92439
22	1.16629	1.16629	1.74944
23	0.93304	0.93304	1.39955
24	0.81641	0.81641	1.22461
25	0.46652	0.46652	0.69978
Summa	1.00000	25.18311	37.77467

Fig. 1. M16I miscible displacement experiment. Inlet pressure vs. time.
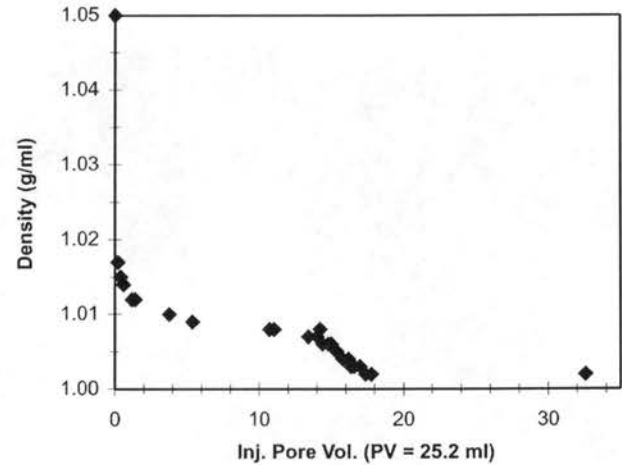
Fig. 2. M16I miscible displacement experiment. Density of produced fluid vs. volume of injected fluid.
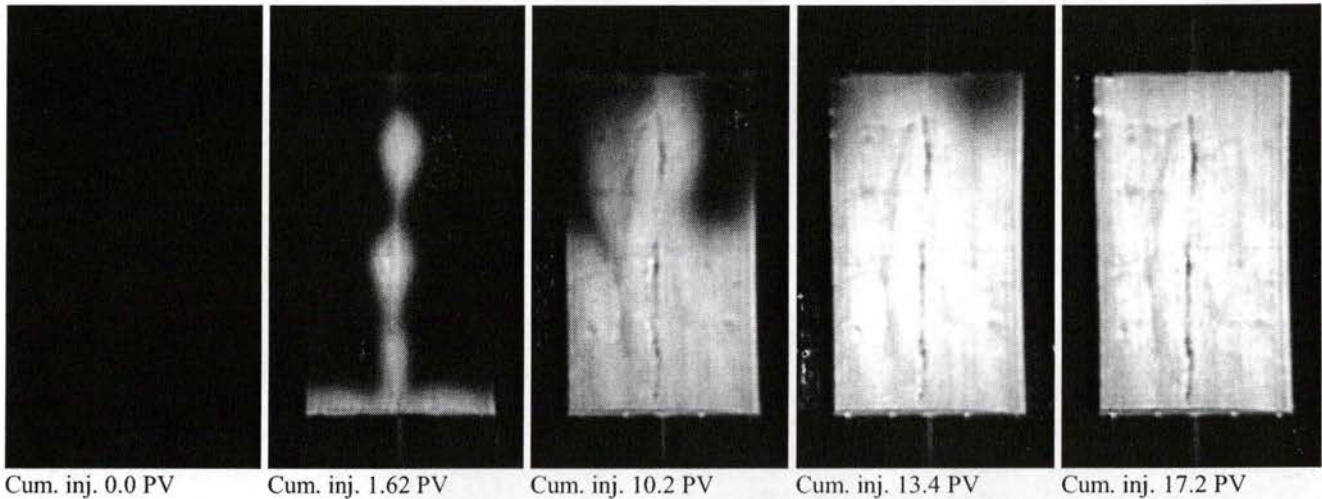

Cum. inj. 0.0 PV   Cum. inj. 1.62 PV   Cum. inj. 10.2 PV   Cum. inj. 13.4 PV   Cum. inj. 17.2 PV

Fig. 3. Type A NMR M0 maps showing progression of the flooding experiment. The maps represents an axial slice through the sample perpendicular to the fracture. The trace of the fracture is vertical in the centre of the sample. The flow is from the bottom towards the top of the images. Fluid in the inlet and outlet fittings are visible respectively at the bottom and top of the maps. The images are labelled by the amount of fluid in pore volumes (PV) that was injected at the time of data acquisition. Field of view is 9 x 5 cm. Slice thickness 0.45 cm. Signal intensities are represented by a linear grey scale with black=0 and white=0.060. Signal intensities are in arbitrary SISCO magnetisation units.

Cum. inj. 0.0 PV   Cum. inj. 1.06 PV   Cum. inj. 1.59 PV   Cum. inj. 4.9 PV

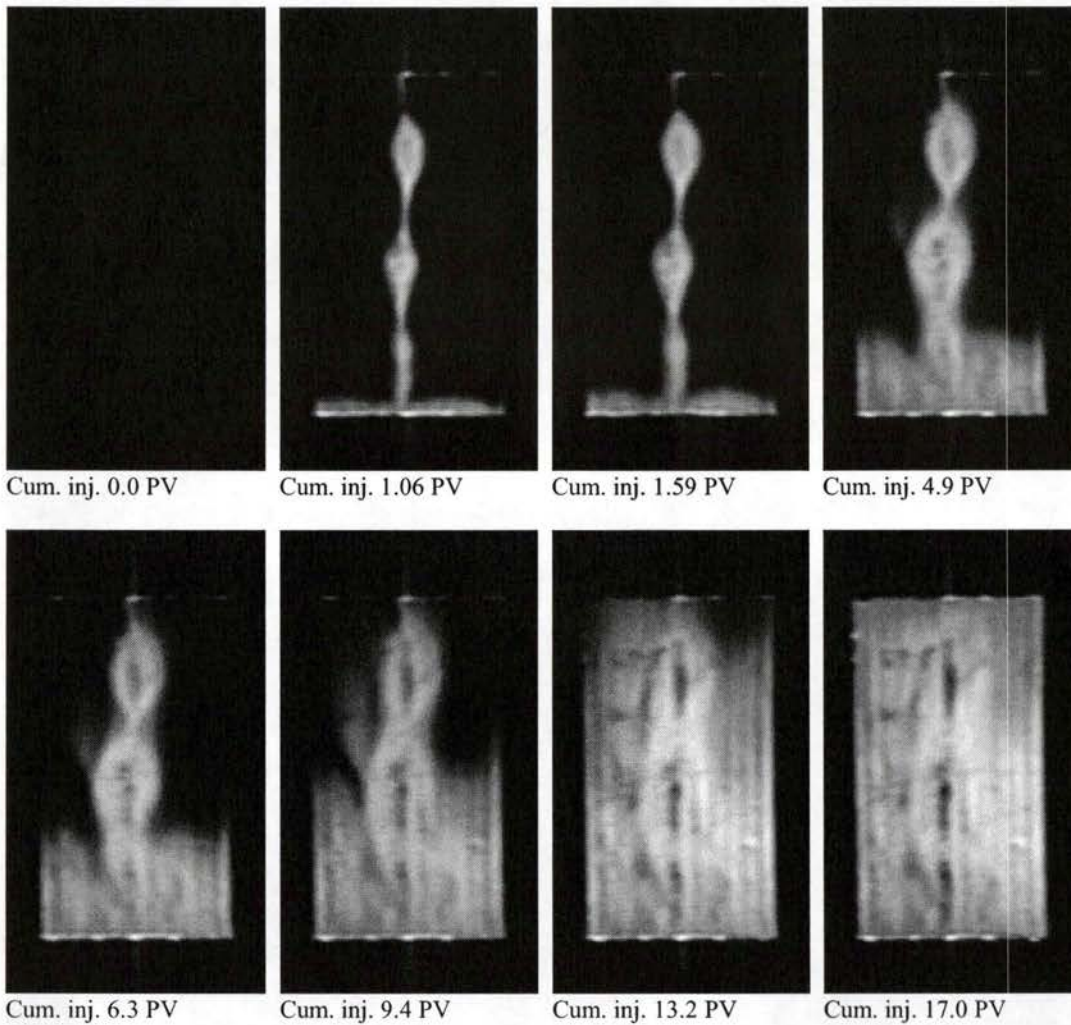Cum. inj. 6.3 PV   Cum. inj. 9.4 PV   Cum. inj. 13.2 PV   Cum. inj. 17.0 PV

Fig. 4. Type B NMR images showing progression of the flooding experiment. The images represent an axial slice through the sample perpendicular to the fracture. The trace of the fracture is vertical in the centre of the sample. The flow is from the bottom towards the top of the images. Fluid in the inlet and outlet fittings are visible respectively at the bottom and top of the images. Field of view is 9 x 5 cm. Slice thickness 0.45 cm. Signal intensities are represented by a linear grey scale with black=0 and white=0.035. Signal intensities are in arbitrary SISCO magnetisation units.
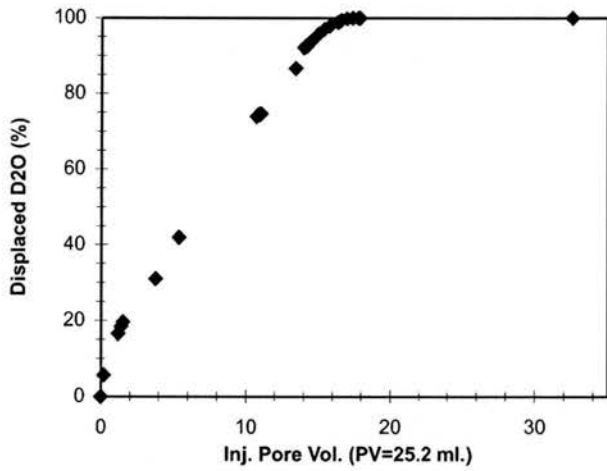
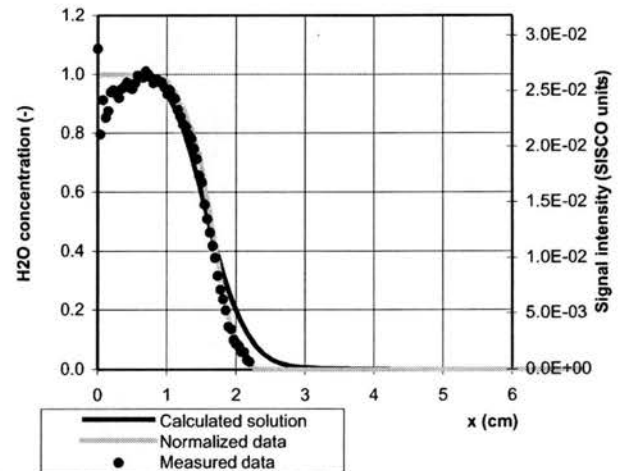Fig. 10. M16I miscible displacement experiment. Fraction of D_2O in production vs. volume of injected fluid.
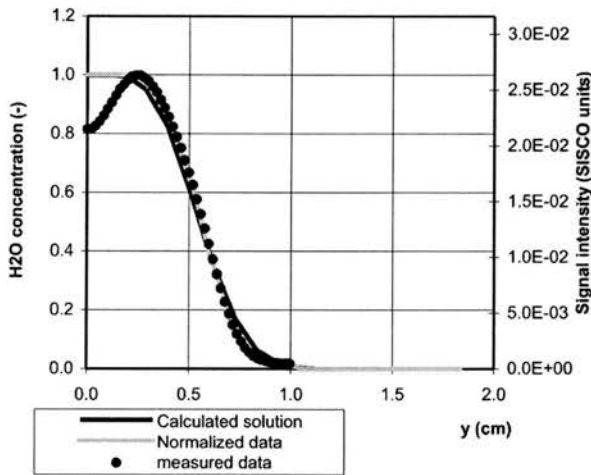

Fig. 11. Plug M16I H_2O concentration, Profile 1.

Fig. 12. Plug M16I H_2O concentration, Profile 2.
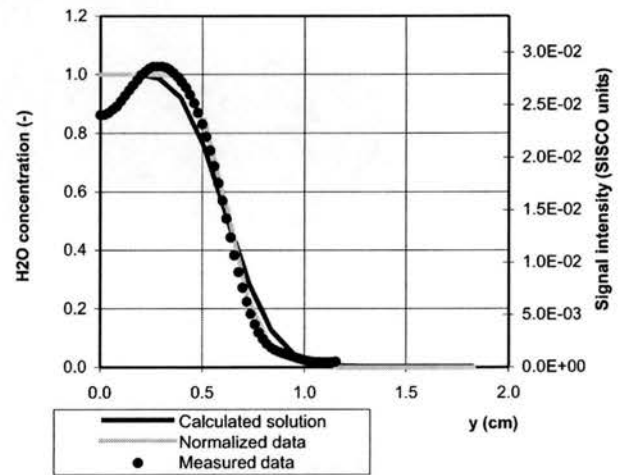

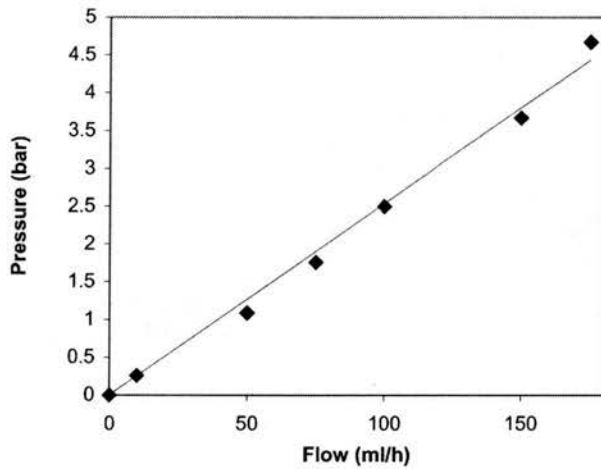Fig. 13. Plug M16I H_2O concentration, Profile 3.

Fig. 14. M16I additional flow experiment to check relationship between pressure and flow rate.
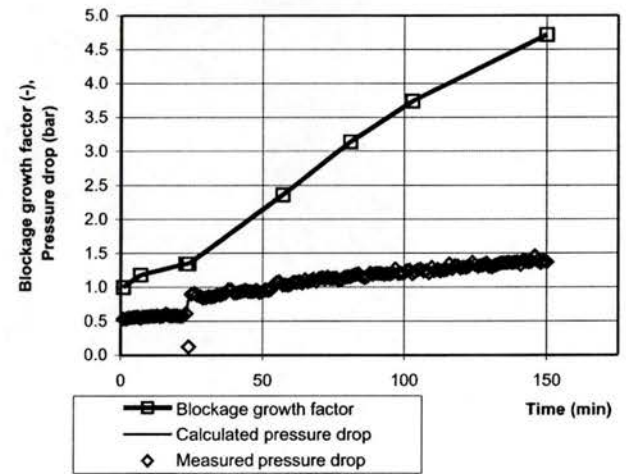

Fig. 15. Growth in fracture blockage with time.

Appendix D

Flow in Fractured Chalk. COWI report 42039/D1+D2, October 1999.

EFP-98: 1313/98-0008

FLOW IN FRACTURED CHALK

PART I:

Study of Waterflooding of a Fractured System using Small-scale Simulation Models

PART II:

Up-scaling of Shape Factors

October 1999

Table of Contents

Part I

Study of Waterflooding of a Fractured System
using Small-scale Simulation Models

Appendices

PART II

Up-scaling of Shape Factors

PART I

EFP-98: 1313/98-0008

STUDY OF WATERFLOODING OF A FRACTURED SYSTEM USING SMALL-SCALE SIMULATION MODELS

Description of Double Continuum Formulation
for Specific Fracture Trajectory

October 1999

1   INTRODUCTION

Displacement mechanisms when waterflooding a low permeable fractured system are studied using small-scale 2D simulation models (30×30 cm). The models are constructed using the single continuum formulation i.e. discrete models. The exchange of fluids in a matrix-fractured system is controlled by a combination of forces: Capillary forces, gravity forces and viscous forces. The model dimensions and flow conditions are set-up so that capillary forces will dominate the waterflooding. Three idealised fracture configurations are examined.

The single continuum small-scale models are translated to a double continuum formulation (dual permeability). In order to describe a specific fracture trajectory using the double continuum formulation it is necessary evaluate the matrix and fracture properties: Porosity, shape factor and permeability factors. The derivation of the correct double continuum matrix and fracture properties to describe a specific fracture trajectory is presented.

All simulations have been run using the COSI reservoir simulator.

2 SINGLE CONTINUUM MODELS

The simulation models are 2D models with the dimensions: 30×30 cm consisting of 418 to 513 grid blocks depending on the fracture configuration. In all models the low permeable matrix is surrounded by a 5 mm wide fracture. Initially the model is filled with oil and connate water. Water is injected at the bottom while oil and water are produced from the top-centre of the models as shown in figure 2-1. A constant pressure drop of 1 psi, corresponding to 1 psi/ft, is applied over the model at all times. Physical properties of the single continuum models are summarised in table 2-1.
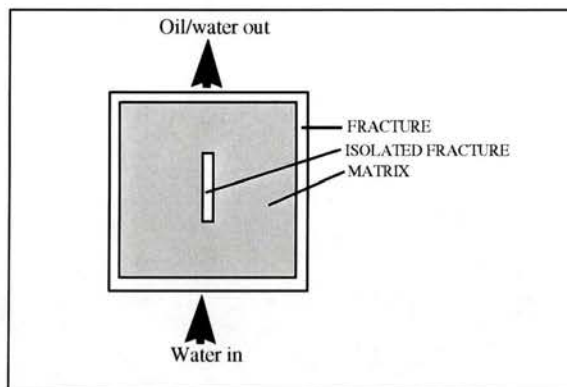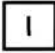

Figure 2-1 Example of fracture model.

	Porosity [%]	Abs. Perm. [md]	Swc [%]	Sor [%]	Relative Permeability	Capillary Pressure [psi]
MATRIX	40	5	5	30		
FRACTURE	50	1000	0	0		Pc=0

Table 2-1 Physical properties of the single continuum matrix and fracture gridblocks.

COWI

Step functions are used to describe the relative permeability in the fracture grid cells in order avoid numerical dispersion. This step function also gives a better visual representation of the propagating waterfront in the fractures. It would have been more correct to describe the fracture relative permeability using straight line functions for flow in all directions except for flow in the positive z-direction (upwards) where step functions must be applied to ensure vertical segregation. However, at present directional relative permeability curves are not implemented in the reservoir simulator. In order to check the effect of having straight line or step function relative permeability in the fracture, additional simulations were run using only straight line functions. The difference in the results was negligible.

Three basic fracture configurations have been studied with three different types of internal fractures:

I.   Isolated Fracture   :

II.   Connected Fracture :

III.   Horizontal Fracture :

The grid used in the Isolated Fracture simulation model is shown below in figure 2-2. A fine grid is applied near the fractures and at the end of the isolated fracture.
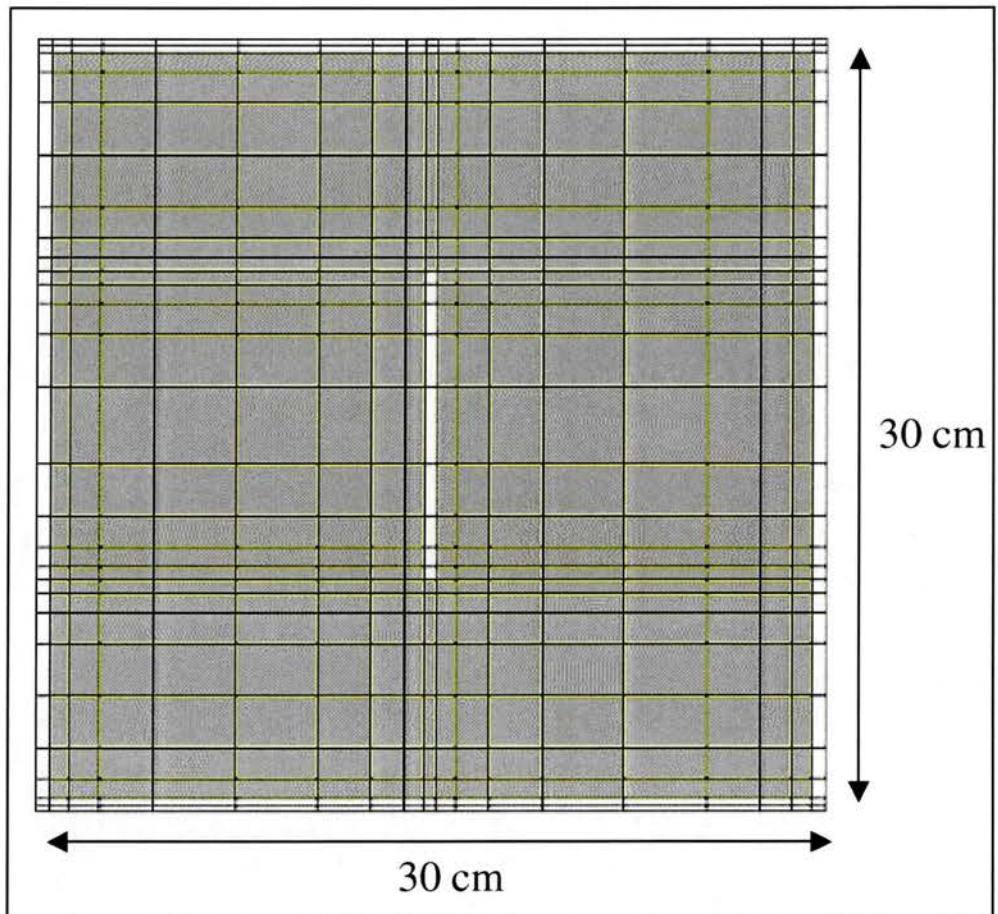

Figure 2-2 Grid used for Isolated Fracture model.

3   WATERFLOODING RESULTS

Development of the oil saturation in the three simulation models during water flooding are presented in appendix A, B and C. In all cases the water enters the surrounding fracture and displaces the oil by a piston like displacement. As the water gets in contact with the matrix it advances into the matrix due to capillary imbibition. The water front in the matrix is smeared out and progresses faster than the oil water contact in the surrounding fracture.

The internal fractures are not immediately flooded even though the water saturation in the surrounding matrix increases beyond the connate water saturation. In the Connected (II) and the Horizontal (III) Fracture cases, the oil still remains in the internal fracture after water has passed in the surrounding fracture.

Mechanism

The mechanism for the water flood can be explained by considering the capillary pressure:

$$P_c = P_o - P_w \tag{1}$$

Fracture: $P_c^{fr} = 0$, so

$$P_o^{fr} = P_w^{fr} = P^{fr} \tag{2}$$

Matrix: $P_c^{ma} = P_c(S_w^{ma})$, (Imbibition curve, figure 3-1).
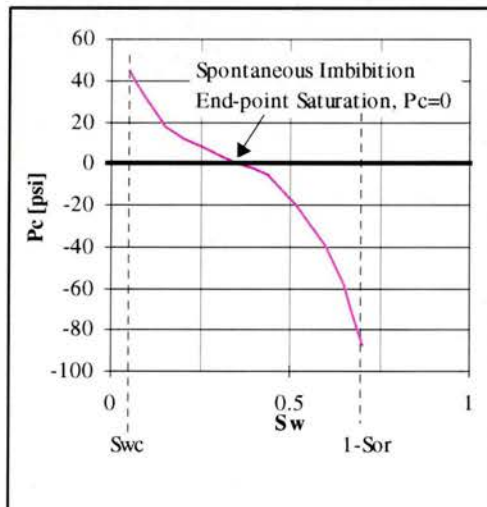

Figure 3-1   Matrix capillary pressure Imbibition curve.

COWI

By rearranging equation (1) the matrix water pressure can be expressed,

$$P_w^{ma} = P_o^{ma} - P_c(S_w^{ma}) \tag{3}$$

Initially there is no water present in the fractures and pressure equilibrium exists over the matrix-fracture interfaces:

$$P_o^{fr} = P_o^{ma} \tag{4}$$

By considering equation (2) to (4) and figure 3-1 we get that,

$$P_w^{ma} < P_w^{fr}, \tag{5}$$

during the imbibition process i.e. water will flow from the fracture into the matrix by spontaneous capillary imbibition and displace the oil in the matrix.

No water will flow from the matrix to a fracture since $P_w^{ma} < P_w^{fr}$ as long as $P_c(S_w^{ma}) \geq 0$ (see figure 3-1). This means that the internal fractures will stay oil filled.

As water saturation in the matrix (S_w^{ma}) increases, $P_c(S_w^{ma})$ decreases. If the capillary force is the only force affecting the system $P_c(S_w^{ma})$ will go towards 0 and the water saturation will go towards the spontaneous imbibition end-point saturation shown on figure 3-1 (In this specific case the imbibition end point saturation, $S_w^{ma} = 0.35$).

When $P_c(S_w^{ma}) = 0$ we have,

$$P_w^{ma} = P_o^{ma} = P^{fr}, \tag{6}$$

thus no more flow will occur leaving the internal fractures still filled with oil.

Since a pressure gradient (1 psi) is applied over the fracture models, water will continue flowing into the matrix due to the viscous force. The saturation in the matrix (S_w^{ma}) will increase beyond the spontaneous imbibition end-point saturation making $P_c(S_w^{ma})$ negative. Water will now be able to enter the internal fractures and displace the oil due to the negative capillary pressure:

$$P_w^{ma} > P_o^{ma} = P_o^{fr} = P_w^{fr}, \tag{7}$$

The resulting end water saturation of the matrix (and thereby the recovery) will depend on the balance between the pressure gradient and the negative capillary pressure with a maximum of $1 - S_{or}$.

4   DOUBLE CONTINUUM FORMULATION

The fracture models are translated to the double continuum formulation using the dual permeability option. The dual permeability option allows matrix to matrix flow between neighbouring cells ensuring capillary continuity. The double continuum models contains 15×15 grid cells of equal size.

In order to describe the specific fracture trajectories in the simulation models using the double continuum formulation, it is necessary evaluate the matrix and fracture properties: Porosity, Matrix fracture exchange (shape factor) and permeability factors.

The derivation of the matrix and fracture properties for a grid cell in the double continuum formulation is described for the matrix fracture configuration in figure 4-1. The figure shows the fracture geometry and the grid cell in the 2D double continuum model. Note that the fracture extends into the neighbouring grid cells above and below.
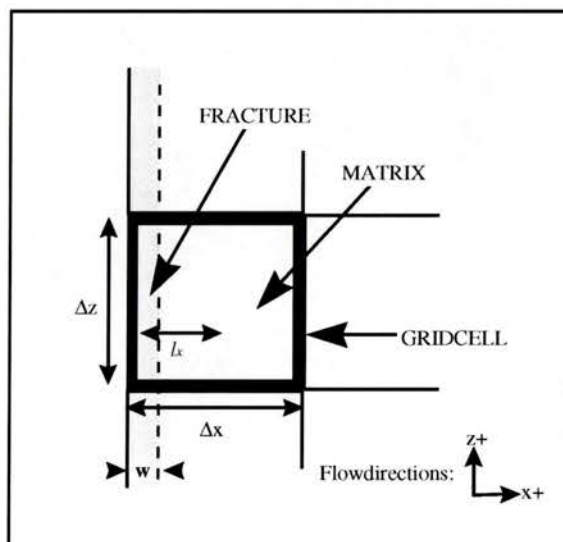

*Figure 4-1 Grid cell dimensions and fracture geometry to
be simulated using a double continuum formulation.*

For the 2D grid cell in figure 4-1 the following input must be calculated:

Porosity
The porosity is calculated from simple volume considerations.

Fracture porosity ($\phi_{fr}{}^d$):

$$\phi_{fr}^d = \frac{V_{fr}\,\phi_{fr}^s}{V_{gridcell}} = \frac{\Delta z w\,\phi_{fr}^s}{\Delta x \Delta z}, \tag{8}$$

where superscript d and s indicate double and single continuum model respectively.

Matrix porosity ($\phi_{ma}{}^d$):

$$\phi_{ma}^d = \frac{V_{ma}\,\phi_{ma}^s}{V_{gridcell}} = \frac{\Delta z(\Delta x - w)\,\phi_{ma}^s}{\Delta x \Delta z}, \tag{9}$$

Shape factor
The shape factor σ is derived by considering Darcy's equation. The fluid exchange between matrix and fracture in the grid cell expressed as volume flow rate q of phase j is, using a finite difference approximation for the pressure gradient:

$$q_j = A \cdot k \cdot \frac{k_{r,j}}{\mu_j} \cdot \frac{\Delta P_j}{l}, \tag{10}$$

where

A :Matrix-fracture flow area, Δz
k :Absolute permeability
$k_{r,j}$:Relative permeability of phase j
μ_j :Viscosity of phase j
ΔP_j :Matrix-fracture pressure difference in phase j
l :Matrix-fracture flow distance, $\Delta x/2$ assuming $w \ll \Delta x$

The Darcy equation (10) with the shape factor σ introduced, as implemented in reservoir simulation, writes:

$$q_j = \sigma \cdot V_{gridcell} \cdot k \cdot \frac{k_{r,j}}{\mu_j} \cdot \Delta P_j \tag{11}$$

From equation (10) and (11) it is possible to derive an explicit expression for the shape factor. For the geometry in figure 4-1 in which matrix-fracture flow is only in the x-direction and l_x is equal to $\Delta x/2$ assuming the fracture aperture $w \ll \Delta x$. The shape factor for the grid cell in figure 4-1 then becomes:
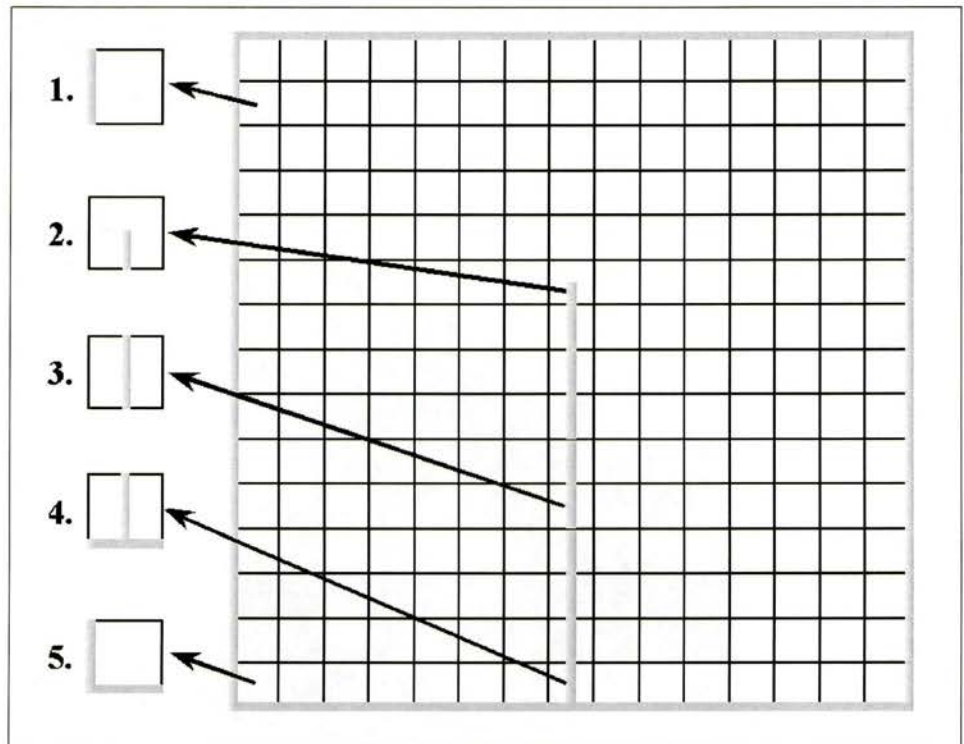
$$\sigma = 2/\Delta x^2 \tag{12}$$

COWI

Permeability Factors[1]

To obtain the correct matrix and fracture flow into neighbouring grid cell, Permeability factors (or transmissibility factors) in the positive x and z directions must be specified for both the fracture and matrix medium in the gridcell. For the example in figure 4-1 permeability factors become:

Fracture: x-permeability factor = 0, i.e. no fracture to fracture
                                                   flow in the x-direction.

$$z\text{-permeability factor} = \frac{A_{fr}}{A_z} = \frac{w}{\Delta x} \qquad (13)$$

where

A_{fr} :Area of the fracture-fracture interface in the
       z-direction
A_z :Area of the total gridcell interface in the
       z-direction.

Matrix: x-permeability factor = 1

$$z\text{-permeability factor} = \frac{A_{ma}}{A_z} = \frac{\Delta x - w}{\Delta x} \qquad (14)$$

where

A_{ma} :Area of the matrix-matrix interface in the
       z direction.

The above example demonstrates how a specific fracture trajectory can be defined in the double continuum formulation. In figure 4-2 the grid for the double continuum model is shown with the Connected Fracture configuration (II) drawn on top. Grid cells containing different fracture geometries have been highlighted and the shape factors and permeability factors for these grid cells are summarised in table 4-1.

---

[1] Multiplier for the permeability on a grid cell interface. Example: A matrix (or fracture) x-permeability factor in grid cell (i , j , k) are multiplied on the grid cell interface permeability between grid cell (i , j , k) and grid cell (i+1, j , k).

*Figure 4-2 Grid from double continuums model showing
grid cells with different fracture geometries.*

Grid Cell Figure 4-2	Shape Factor σ	x-perm. factor		z-perm. factor	
		Fracture	Matrix	Fracture	Matrix
1.	$\dfrac{2}{\Delta x^2}$	0	1	$\dfrac{w}{\Delta z}$	$\dfrac{\Delta z - w}{\Delta z}$
2.	$\dfrac{4}{\Delta x^2}$	0	1	0	1
3.	$\dfrac{8}{\Delta x^2}$	0	1	$\dfrac{w}{\Delta z}$	$\dfrac{\Delta z - w}{\Delta z}$
4.	$\dfrac{8}{\Delta x^2} + \dfrac{2}{\Delta z^2}$	$\dfrac{w}{\Delta x}$	$\dfrac{\Delta x - w}{\Delta x}$	$\dfrac{w}{\Delta z}$	$\dfrac{\Delta z - w}{\Delta z}$
5.	$\dfrac{2}{\Delta x^2} + \dfrac{2}{\Delta z^2}$	$\dfrac{w}{\Delta x}$	$\dfrac{\Delta x - w}{\Delta x}$	$\dfrac{w}{\Delta z}$	$\dfrac{\Delta z - w}{\Delta z}$

Table 4-1 Shape factors and permeability factors for grid cells in figure 4-2

5 COMPARING RESULTS

Simulation results from the single and double continuum models have been compared. Oil production obtained from the simulations of the Isolated (I) and Horizontal (III) Fracture cases are presented in figure 5-1 and 5-2 respectively.
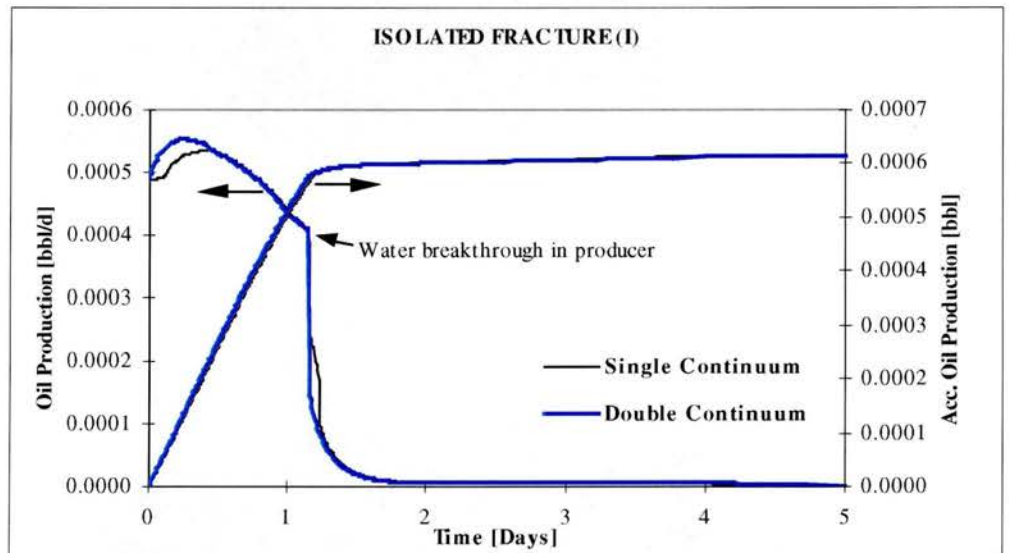

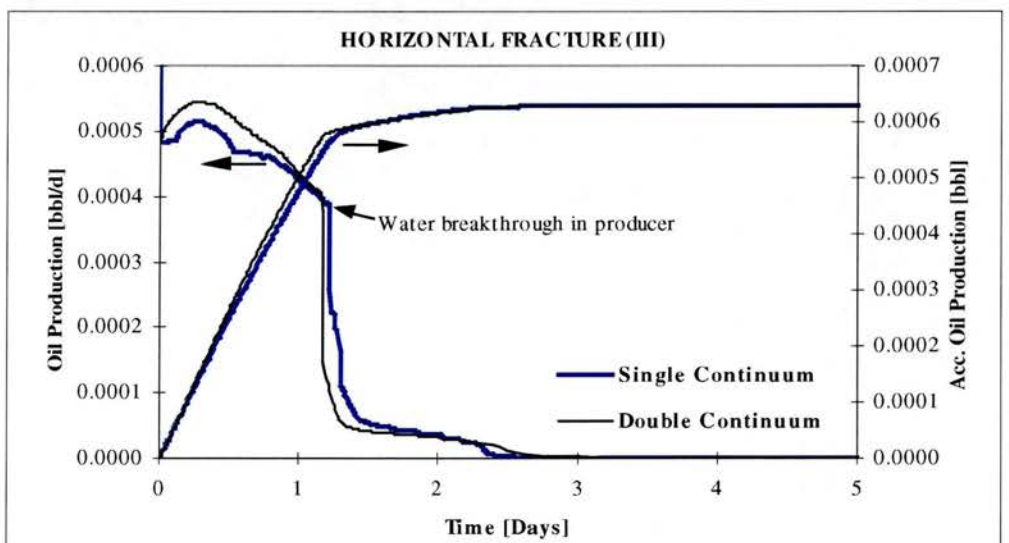*Figure 5-1* Oil production from single and double continuum models of an isolated fracture (I).

Figure 5-2 Oil production from single and double continuum models of a horizontal fracture (III).

COWI

Results for the Connected Fracture (II) case are not presented here since they are very similar to the results seen in the Isolated Fracture case i.e. the same conclusions can be drawn.

There is good agreement between results for the Isolated Fracture. The minor discrepancies observed are due to the differences in the grid cell size in the two cases.

In the Horizontal Fracture (III) case the oil production before water break-through is generally higher in the double continuum model. The reason is that in the single continuum model the horizontal fracture acts as a barrier for the imbibition of the matrix in the top half of the model. No water will imbibe into the matrix above the fracture until the water front in the surrounding fracture has passed the horizontal fracture (see Appendix C). In the double continuum model this is not the case. The horizontal fracture do not hinder the imbibition into the matrix above, since the matrix, when using the dual permeability op-tion, is defined as one connected medium. The dual permeability option there-fore establishes capillary continuity between the upper and the lower matrix blocks however, the differences in the grid cell size also contribute to the dif-ferences.

Despite the differences explained above there is good agreement between the results obtained from the single and double continuum models respectively.

Figure 5-3 below shows the sensitivity of the oil production to the number of grid cells in the double continuum model of the Isolated Fracture (I) case.
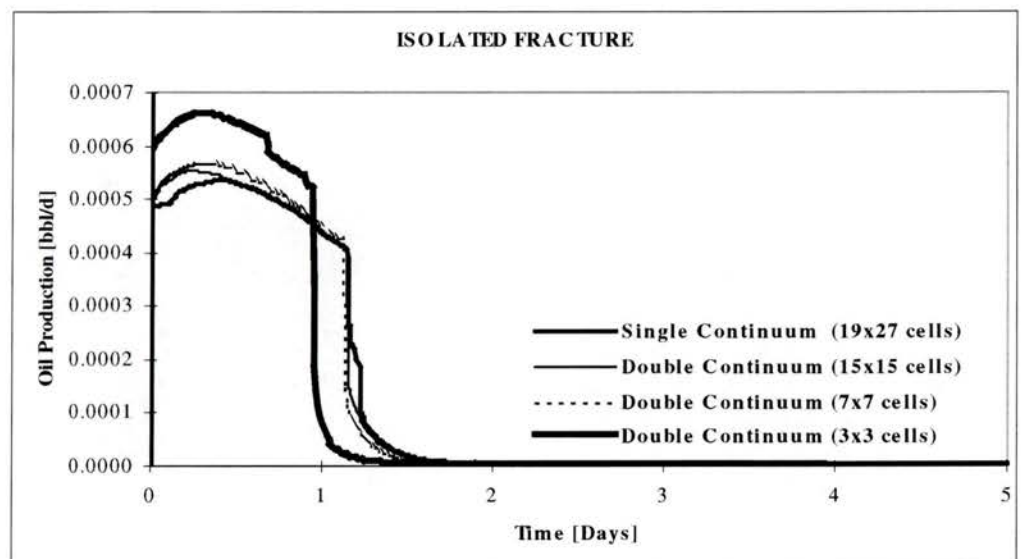

Figure 5-3 Sensitivity of the oil production to the number of gridcells in the double continuum model of the isolated fracture (I).

Using only 7 × 7 grid cells there is still a good agreement with the single con-tinuum model with respect to both the production rate and the time of water breakthrough. In the 3 × 3 cell model the effect of the grid geometry leads to large discrepancies in the oil production.

6   CONCLUSION

The displacement mechanisms of waterflooding a low permeable fractured system have been described in detail using observations from small scale 2D single continuum simulation models. It is shown that internal fractures, even though connected to the main fracture system, are not flooded with water until the water saturation in the surrounding matrix increases above the spontaneous imbibition end point saturation defined by the imbibition capillary pressure curve. In order for this to happen a pressure gradient must be applied over the system.

It have been shown how to derive the correct matrix and fracture properties: Porosity, shape factors and permeability factors, in order to describe a specific fracture trajectory in the double continuum formulation, by translating single continuum fracture models to double continuum models. There is good agreement between the simulation results obtain from the single and double continuum models. It is possible to reduce the number of grid cells by more than a factor 10 in the double continuum models compared to the single continuum models and still model fracture flow, matrix flow and the fracture-matrix interaction correctly.

7   NOMENCLATUR

A	: Area
k	: Absolute permeability
k_r	: Relative permeability
l	: Distance, length
P	: Pressure
q:	: Volume flow rate
S	: Saturation
w	: Fracture width (aperture)
$\Delta x, \Delta z$	: Grid cell dimensions
ϕ	: Porosity
μ	: Viscosity
σ	: Shape factor

Superscript:

d	: Double continuum formulation
fr:	: Fracture
ma	: Matrix
s	: Single continuum formulation

Subscript:

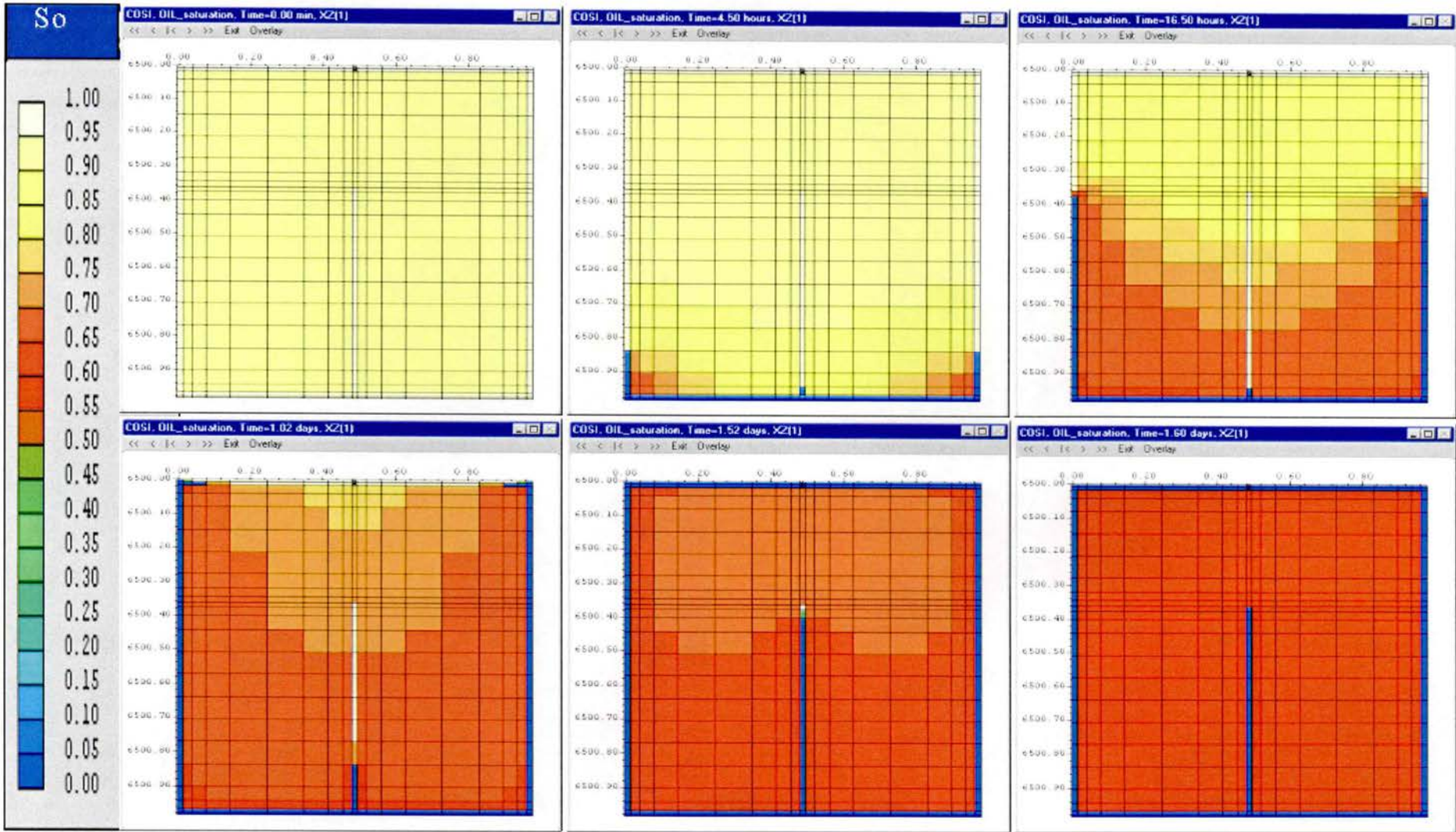|	
c	: Capillary
fr	: Fracture
j	: Fluid phase
ma	: matrix
o	: Oil
w	: water
z, x	: Flow direction

APPENDIX A

Waterflooding
ISOLATED FRACTURE (I)
2D Simulation Model (30 × 30 cm)
Oil Saturation
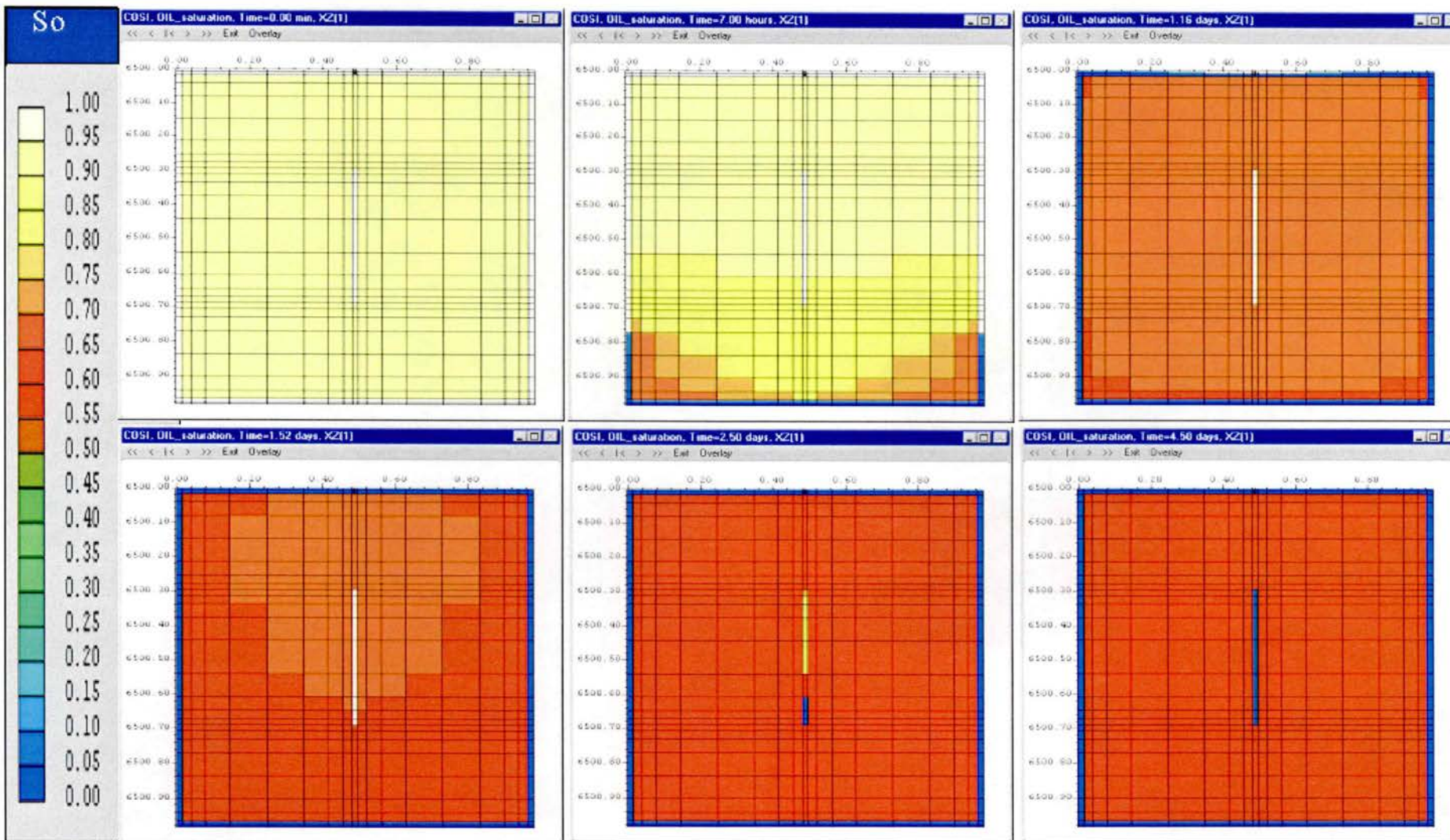
APPENDIX B

Waterflooding
CONNECTED FRACTURE (II)
2D Simulation Model (30 × 30 cm)
Oil Saturation

APPENDIX C

Waterflooding
HORIZONTAL FRACTURE (III)
2D Simulation Model (30 × 30 cm)
Oil Saturation
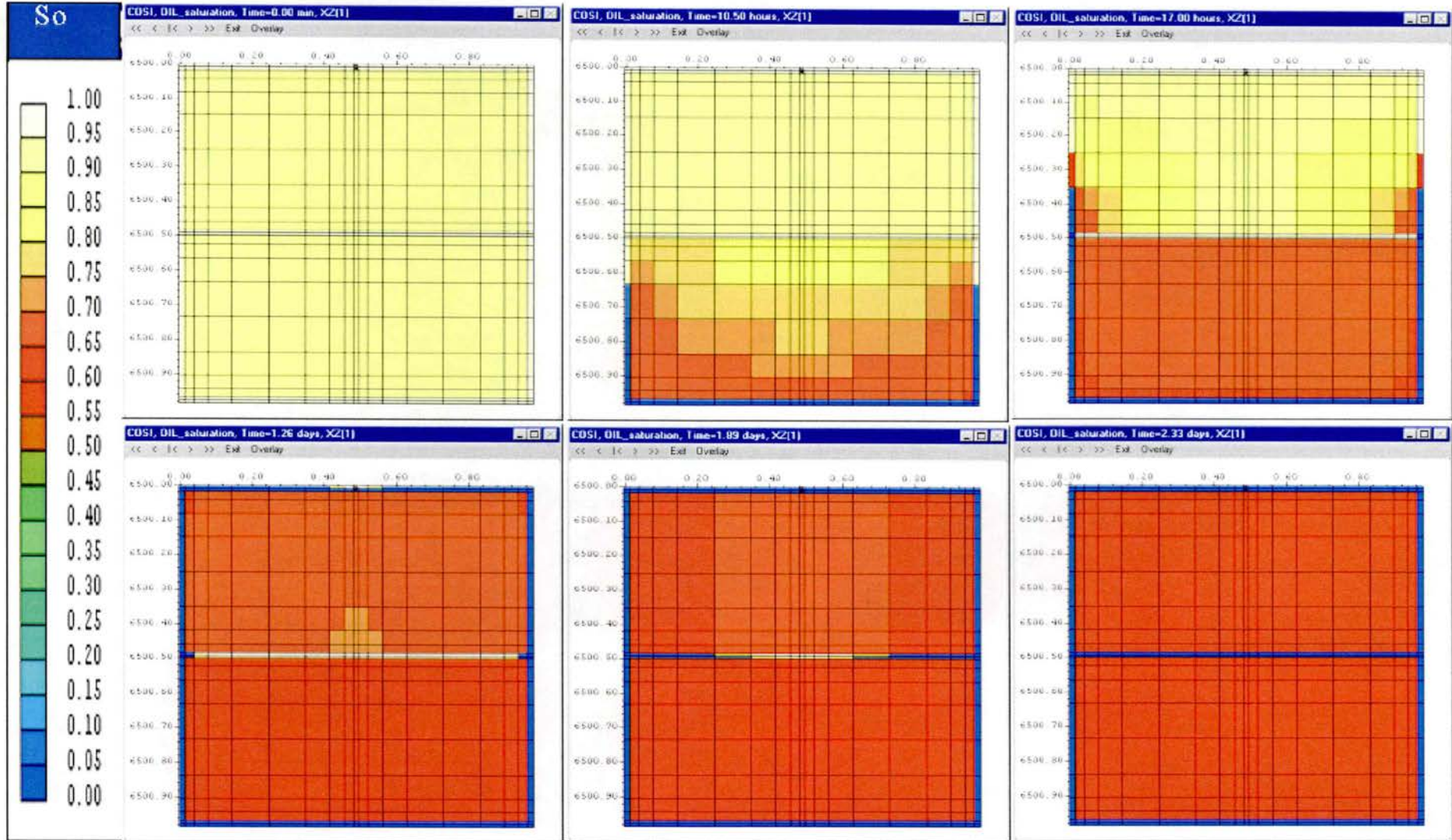
PART II

EFP-98: 1313/98-0008

UP-SCALING OF SHAPE FACTORS

October 1999

1 INTRODUCTION

This section describes a new method for up-scaling of shape factors for arbitrary 2D-fracture patterns.

The shape factor concept introduced in [1, 2] is a convenient notion for the description of the flow rate due to pressure differences between the matrix and the fractures. The shape factor depends only on the geometry of the rock matrix blocks and permeability anisotropy. The shape factor is independent of the flowing phase.

Shape factors are used in reservoir simulation of fractured systems using a double continuum formulation.

The shape factor describes the matrix fracture exchange due to pressure differences between the fracture system and the matrix blocks. For two-phase flow in fractured tight chalk reservoirs large pressure differences usually exist between the matrix and the fractures because of large capillary pressures in the chalk matrix and zero capillary pressure in the fracture system.

As the vast majority of hydrocarbons are situated in the matrix in which the fracture system acts as a transport network for flow towards the wells, the matrix fracture exchange is an important mechanism that must be accounted for when quantifying the resultant flow. A fist step in the description of this mechanism is to be able to calculate effective shape factors for general fracture patterns.

Initially it is shown how the Kazemi [3] shape factor is calculated from Darcy's equation describing the matrix fracture exchange rate for a simple fracture system using a finite difference formulation. The shape factors are then calculated for a number of simple matrix fracture configurations, which can be assembled into a grid to form a general fracture pattern. Then by applying a pressure gradient between the fracture network and the matrix by means of sources and sinks the resulting matrix to fracture flow can be calculated by a single-phase steady state flow solver. The effective shape factor for a general fracture pattern can be calculated from the total matrix to fracture flow, the up-scaled absolute matrix permeability and the average pressures in the matrix and the fracture.

2   CALCULATION OF KAZEMI SHAPE FACTOR

Darcy's equation

The velocity, U_j, of a phase j flowing between two reservoir positions due to pressure differences in the reservoir is given by Darcy's equation:

$$U_j = -\frac{k_{r,j}}{\mu_j} \cdot k_d \cdot \left(\frac{\partial P_j}{\partial d} - \rho_j \cdot g \cdot \frac{\partial z}{\partial d} \right).$$ (1)

Where $k_{r,j}$ is the relative permeability of phase j, and μ_j the viscosity of phase j. The term in the parenthesis is the pressure gradient of phase j in the direction, d, along the line connecting the two reservoir positions including the hydrostatic pressure difference. The absolute permeability in the d-direction is denoted k_d.

The volumetric flow of phase j between the two reservoir positions through an area A is given by

$$q_j = A \cdot U_j$$ (2)

Assumptions

Assumptions for calculation of Kazemi shape factors:
a) *The matrix blocks are of equal size and shape (as shown in figure 2-1).*
b) *The matrix blocks are separated by fractures.*
c) *The fracture volume is negligible compared to the reservoir volume.*
d) *The pressures in all the matrix blocks are equal.*
e) *The pressure in the fracture system is constant.*

With assumption (a) and (c) the number of matrix blocks contained in a reservoir volume V is given by:

$$N^{mb} = \frac{V}{V^{matr}} ,$$ (3)

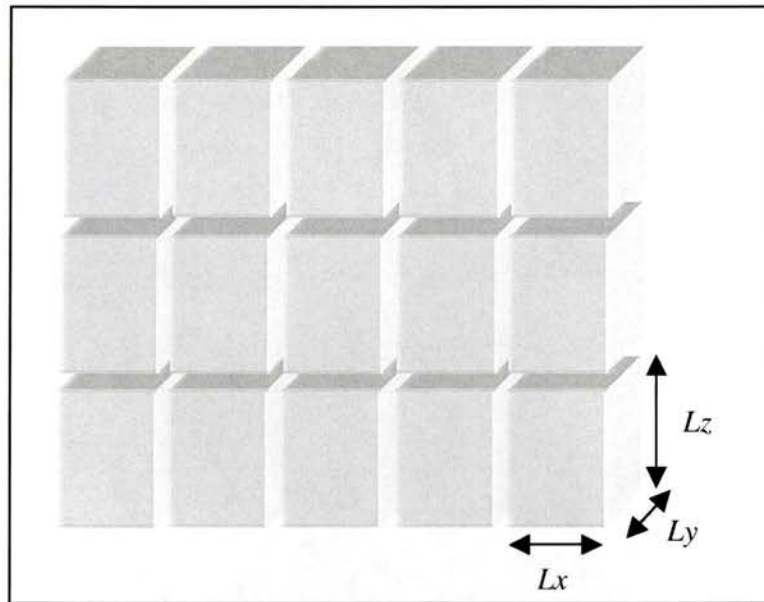in which V^{matr} is the volume of each single matrix block.

Figure 2-1 Equally box shaped matrix blocks.

Single surface

The volume transport of a phase j per unit time, q_j^p, through a surface plane, p, of a single matrix block is given by Darcy's velocity multiplied by the flow area, i.e.

$$q_j^p = A^p \cdot U_j^p = -\frac{k_{r,j}}{\mu_j} \cdot k_d \cdot A^p \cdot \left(\frac{\partial P_j}{\partial d} - \rho_j \cdot g \cdot \frac{\partial z}{\partial d} \right) \tag{4}$$

Single matrix block

Using eq. (4) for all six faces of the matrix block and assuming a linear pressure gradient between the matrix and the fracture the total volume transport from the matrix to the fracture is the sum of the contribution for each surface plane

$$
\begin{aligned}
q_j^{mf} = {} & 2 \cdot \frac{k_{r,j}}{\mu_j} \cdot k_x \cdot \left(L_y \cdot L_z \right) \cdot \frac{P_j^{matr} - P_j^{frac}}{\tfrac{1}{2} L_x} \\
& + 2 \cdot \frac{k_{r,j}}{\mu_j} \cdot k_y \cdot \left(L_x \cdot L_z \right) \cdot \frac{P_j^{matr} - P_j^{frac}}{\tfrac{1}{2} L_y} \\
& + \frac{k_{r,j}}{\mu_j} \cdot k_z \cdot \left(L_x \cdot L_y \right) \cdot \frac{P_j^{matr} - \rho_j \cdot g \cdot \tfrac{1}{2} L_z - P_j^{frac}}{\tfrac{1}{2} L_z} \\
& + \frac{k_{r,j}}{\mu_j} \cdot k_z \cdot \left(L_x \cdot L_y \right) \cdot \frac{P_j^{matr} + \rho_j \cdot g \cdot \tfrac{1}{2} L_z - P_j^{frac}}{\tfrac{1}{2} L_z}
\end{aligned}
\tag{5}
$$

where P_j^{matr} and P_j^{frac} is the pressure of phase j in the centre of the matrix block and in the fracture, respectively. The directional permeabilities in the matrix blocks are denoted k_x, k_y and k_z, and L_x, L_y and L_z are the dimensions of the matrix block.

COWI

From eq. (5) it is seen that the two hydrostatic correction terms cancels out. Introducing the relative mobility $\lambda_j = \dfrac{k_{r,j}}{\mu_j}$ and rearranging eq. (5) using that the matrix block volume is $V^{mb} = L_x \cdot L_y \cdot L_z$ the transport per unit time from a single matrix block can be simplified to

$$q_j^{mf} = \lambda_j \cdot V^{mb} \cdot \left(P_j^{matr} - P_j^{frac}\right) \cdot 4 \cdot \left(\frac{k_x}{L_x^2} + \frac{k_y}{L_y^2} + \frac{k_z}{L_z^2}\right) \tag{6}$$

Total exchange rate Finally, the total transport per unit time from all N^{mb} matrix blocks in the reservoir volume V is

$$q_j^{mf,tot} = \sum_{N^{mb}} q_j^{mf} = \lambda_j \cdot V \cdot \left(P_j^{matr} - P_j^{frac}\right) \cdot 4 \cdot \left(\frac{k_x}{L_x^2} + \frac{k_y}{L_y^2} + \frac{k_z}{L_z^2}\right) \tag{7}$$

Each term in the last parenthesis in eq. (7) refer directly to a certain fracture plane. The term:

$\dfrac{k_x}{L_x^2}$ Originate from exchange with the fractures parallel to the y-z plane,

$\dfrac{k_y}{L_y^2}$ Originate from exchange with the fractures parallel to the x-z plane,

$\dfrac{k_z}{L_z^2}$ Originate from exchange with the fractures parallel to the x-y plane.

Kazemi shape factor For an isotropic medium ($k_x = k_y = k_z = k$) eq. (7) can be simplified to

$$q_j^{mf,tot} = \lambda_j \cdot V \cdot \left(P_j^{matr} - P_j^{frac}\right) \cdot k \cdot \sigma_K \quad , \tag{8}$$

where σ_K is the Kazemi shape factor [3]

$$\sigma_K = 4 \cdot \left(\frac{1}{L_x^2} + \frac{1}{L_y^2} + \frac{1}{L_z^2}\right) \tag{9}$$

3   GENERAL FRACTURE PATTERNS

For general 2D fracture patterns the reservoir area is subdivided into a number of small cells as shown in figure 3-1.
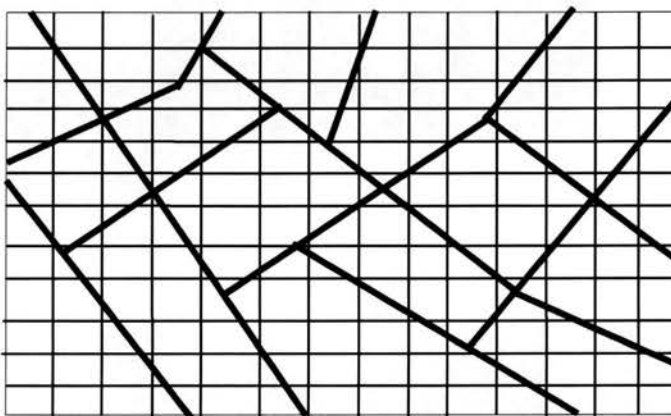

Figure 3-1 General fracture pattern and x,y grid

The basis of the up-scaling procedure to a single effective shape factor, σ_T, for a reservoir area, A, is a fine grid (e.g. $\Delta x, \Delta y$), in which local shape factors, σ_n, are calculated for every grid cell. The effective shape factor is calculated from a 1-phase steady state solution giving the pressure in all the grid cells. A flow from the matrix towards the fractures is accomplished by placing sources in the matrix cells with injection pressures that increases linearly with the distance to the nearest fracture cell. The pressure in the fracture system is kept constant.

The total exchange rate is the sum of the matrix to fracture flow in all grid cells, n, containing fractures

$$q^{mf} = \sum_n \Delta x_n \cdot \Delta y_n \cdot \sqrt{k_{x,n} \cdot k_{y,n}} \cdot \sigma_n \cdot \left(P_n^{matr} - P^{frac} \right) \qquad (10)$$

The effective shape factor, σ_T, is calculated from

$$q^{mf} = A \cdot \sqrt{K_x \cdot K_y} \cdot \sigma_T \cdot \left(\left\langle P^{matr} \right\rangle - P^{frac} \right) \qquad (11)$$

Where A is the reservoir area, and $\overline{K_x}$ and $\overline{K_y}$ is the up-scaled matrix x- and y-permeability, respectively. The average matrix pressure is denoted $\langle P^{matr} \rangle$ and P^{frac} is the fracture pressure.

Local shape factors The local shape factors, σ_n , are calculated assuming a linear pressure gradient from the matrix to the fracture. The local shape factor is calculated as the ratio between the fracture area and the average flow distance from matrix to the fracture in a grid cell.

Three idealised geometric patterns are considered
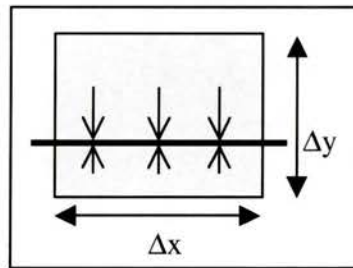
1. Fracture in x-direction.

Figure 3-2 Fracture in x-direction through grid cell

Fracture area: $2 \cdot L \cdot \Delta z = 2 \cdot \Delta x \cdot \Delta z$
Average matrix to fracture flow distance: $h = \frac{1}{4}\Delta y$

Shape factor: $\sigma_n = \dfrac{8}{\Delta y^2} \cdot \dfrac{k_y}{\sqrt{k_x \cdot k_y}}$ (12)

The average flow distance is independent of the position of the horizontal fracture within the grid cell.
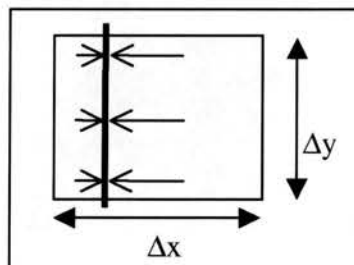
2. Fracture in y-direction.

Figure 3-3 Fracture in y-direction through grid cell

Fracture area: $2 \cdot L \cdot \Delta z = 2 \cdot \Delta y \cdot \Delta z$
Average matrix to fracture flow distance: $h = \frac{1}{4}\Delta x$

Shape factor: $\sigma_n = \dfrac{8}{\Delta x^2} \cdot \dfrac{k_x}{\sqrt{k_x \cdot k_y}}$ (13)

The average flow distance is independent on the position of the vertical fracture within the grid cell.
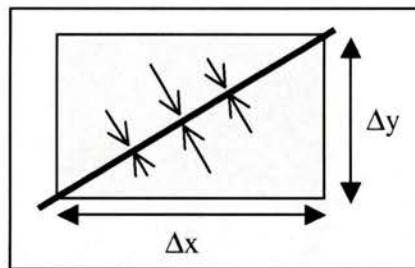
3. Fracture in xy-direction.

Figure 3-4 Fracture diagonally through grid cell

Fracture area $2 \cdot L \cdot \Delta z = 2 \cdot \sqrt{\Delta x^2 + \Delta y^2} \cdot \Delta z$

The approximate average matrix to fracture flow distance is calculated by rearranging figure 3-4 as show in figure 3-5 below.
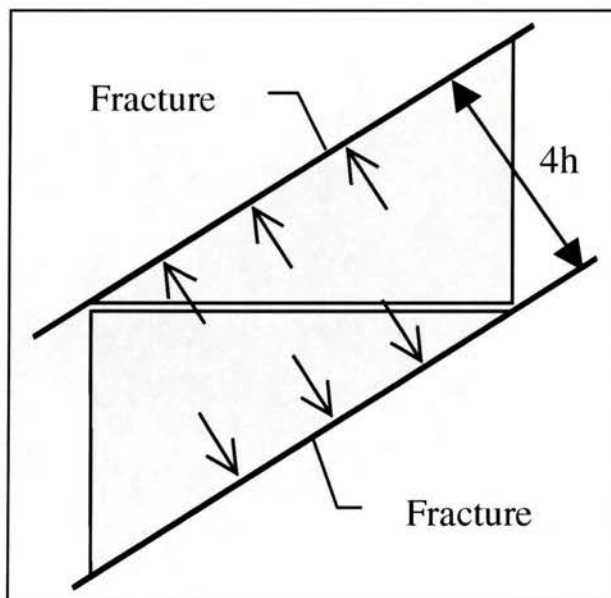

Figure 3-5 Rearrangement of diagonal fracture in grid cell

COWI

From figure 3-5 an approximate average matrix to fracture flow distance is calculated: $h = \frac{1}{4} \frac{\Delta x \cdot \Delta y}{\sqrt{\Delta x^2 + \Delta y^2}}$

and

Shape factor: $\sigma_n = 8 \cdot \left(\frac{1}{\Delta x^2} + \frac{1}{\Delta y^2} \right)$ \hfill (14)

Generally, fractures with dip angle φ and length L may be approximated by:

$$\sigma_n = \begin{cases} \dfrac{8 \cdot L}{\Delta x \cdot \Delta y^2 \cdot \cos(\varphi)} & , \varphi \text{ below or at diagonal,} \\[2em] \dfrac{8 \cdot L}{\Delta x^2 \cdot \Delta y \cdot \sin(\varphi)} & , \varphi \text{ above diagonal.} \end{cases}$$ \hfill (15)

- At dip $0°$ (φ below diagonal) eq. (15) reduces to the horizontal fracture case, 1, eq. (12).
- At dip $90°$ (φ above diagonal) eq. (15) reduces to case 2, eq. (13).
- At the diagonal $\cos(\varphi) = \frac{\Delta x}{\sqrt{\Delta x^2 + \Delta y^2}}$ and $L = \sqrt{\Delta x^2 + \Delta y^2}$ eq. (15) reduces to case 3, eq.(14).

COWI

4   UP-SCALING, EXAMPLE

An example on the calculation of the effective shape factor for a general fracture pattern in an area of size $100m \times 100m$ is presented below. Figure 4-1 show the distribution of the local shape factors on a grid of size 25×50.
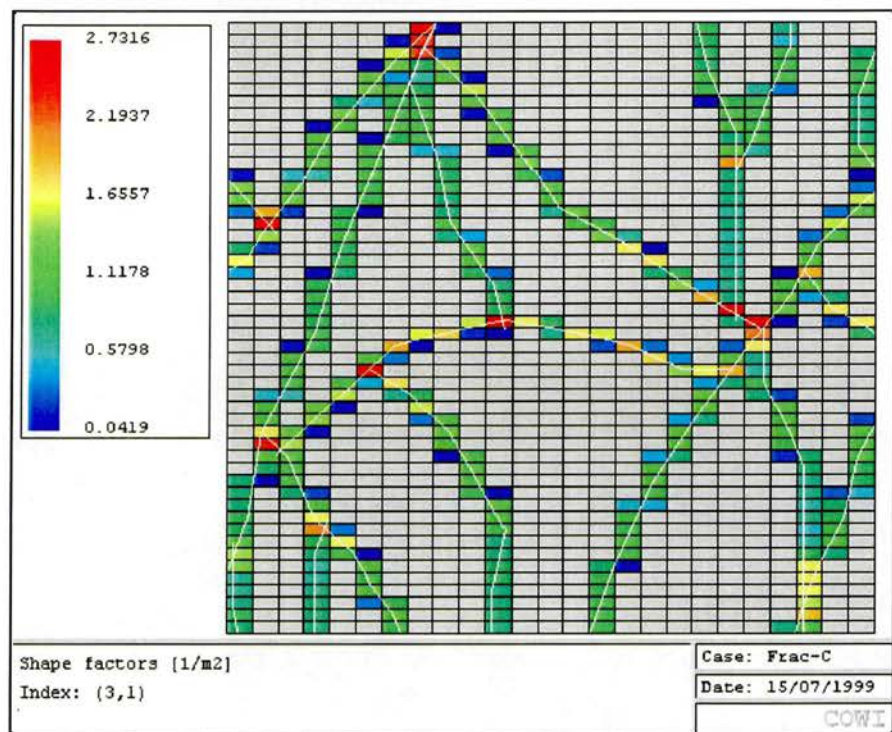

Figure 4-1 Distribution of local shape factors on grid

The one-phase steady state solution to the matrix to fracture flow is the pressure distribution on the grid, figure 4-2. The matrix permeability is $K_x = 4.2$ mD and $K_y = 2.0$ mD.

Matrix areas with low pressure (blue) are effectively drained areas whereas high-pressure areas (red) represent matrix areas, which are poorly drained.
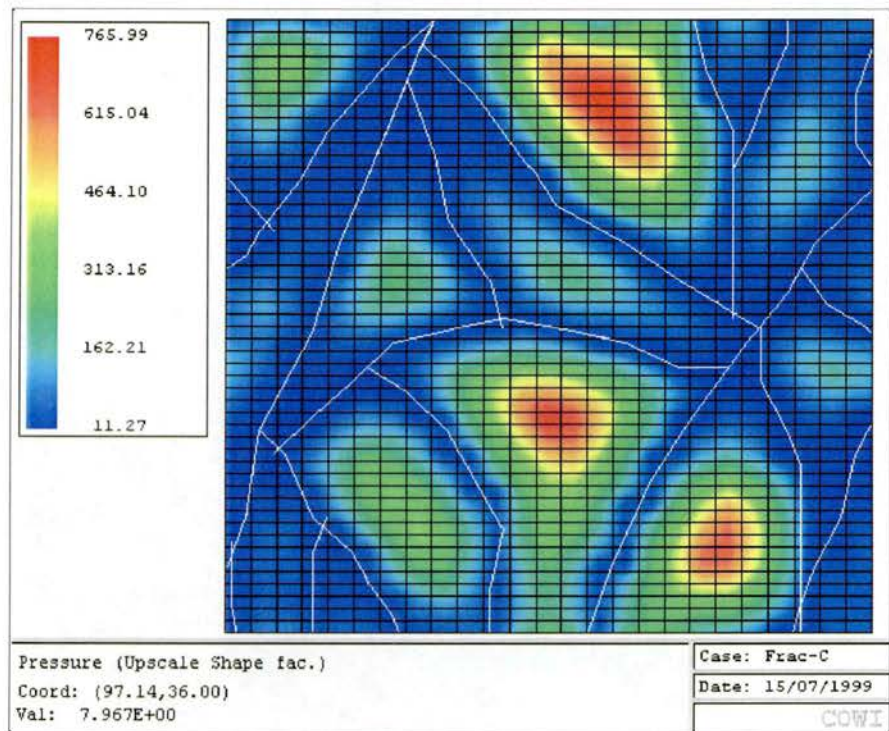
COWI

Figure 4-2 Matrix pressure distribution in the 100mx100m fractured area.

Results

Using eq. (10) and eq. (11) the effective shape factor is calculated to $\sigma_T = 0.013\,m^{-2}$.

To judge the order of magnitude of an effective shape factor a corresponding quadratic shaped matrix block system can be calculated using eq. (9) or eq. (16). The shape factor 0.013 m^{-2} corresponds to a pattern of quadratic matrix block of size approximately 26m × 26m which by visual inspection of figure 4-2 is in good agreement with the actual pattern.

5   VERIFICATION

The shape factor up-scaling procedure is verified by applying the procedure on fracture patterns forming rectangular matrix blocks for which analytic expressions for the shape factor exist. The matrix anisotropy, $\frac{k_y}{k_x}$, is varied from 0.1 to 10. The shape factor for these patterns is given by

$$\sigma = \frac{4}{\sqrt{k_x \cdot k_y}} \cdot \left(\frac{k_x}{L_x^2} + \frac{k_y}{L_y^2} \right). \tag{16}$$

Case 1

Quadratic matrix blocks

A regular fracture pattern forming quadratic matrix blocks of size $5m \times 5m$ as shown in figure 5-1.


```
Backgr    pxls: 156025        Case: Razemil-1
Frac # 2, pxls:    3975       Date: 15/07/1999
                                          COWI
```
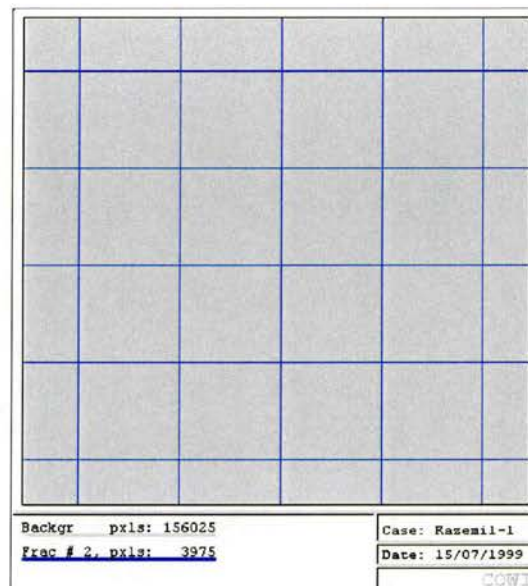
Figure 5-1 Regular pattern of quadratic matrix blocks (periodic boundary conditions)

As periodic boundary conditions are imposed the seemingly smaller matrix blocks at the boundaries are connected to the matrix blocks at the opposite boundary to form full $5m \times 5m$ matrix blocks.
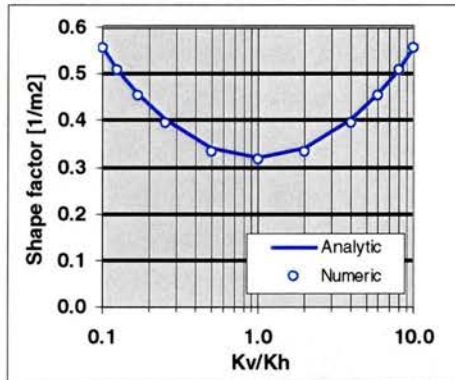
*Figure 5-2 Comparison between effective shape factor and analytic solution
for quadratic fracture pattern.*

The relative error between the analytical and the numerical calculated shape
factor shown in figure 5-2 is below 2% over the entire k_y/k_x range.

Case 2

**Rectangular
matrix blocks**

A regular fracture pattern forming rectangular matrix blocks of size $10m \times 5m$
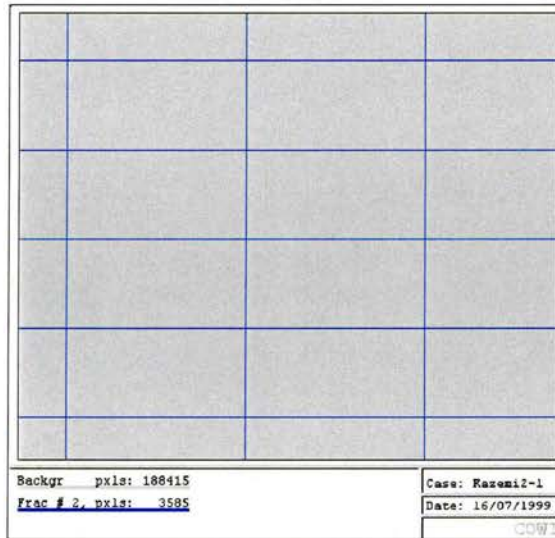as shown in figure 5-3.

Figure 5-3 Regular pattern of rectangular matrix blocks

As in Case 1 periodic boundary conditions are imposed and the smaller matrix
blocks at the boundaries are connected to the matrix blocks at the opposite
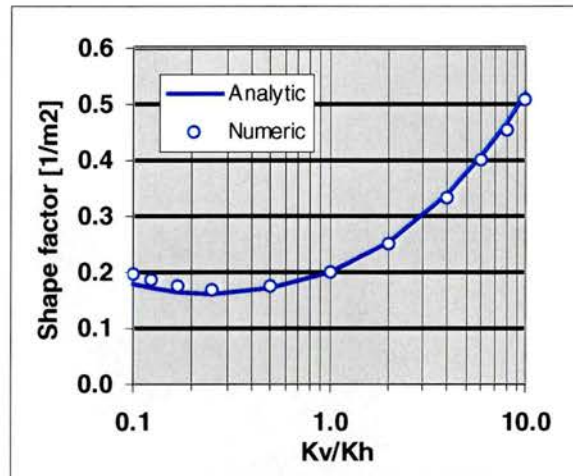boundary to form full $10m \times 5m$ matrix blocks.

COWI

*Figure 5-4 Comparison between effective shape factor and analytic solution
for rectangular fracture pattern.*

The relative error between the analytical and the numerical calculated shape
factor shown in figure 5-4 is below 3% in the range k_y/k_x = 1-10 whereas the
relative error is ~10% for very small k_y/k_x values.

6   DISCUSSION

Conclusion

A fast and easy applicable method for estimation of the magnitude of the shape factors for specific 2D fracture patterns is derived and verified for two simple fracture patterns with varying anisotropy for which analytic expressions exist.

Implementation

The method is implemented as an add-on module in the 2D version of the general fracture pattern analysis tool, FracSynt. In FracSynt the specific fracture pattern can be extracted from scanned photos of e.g. outcrops and the up-scaled matrix permeability used in the shape factor formula is also available.

Some caution must be taken by the user to select a grid in which the fracture pattern can be represented. On a coarse grid the fine scale fracture pattern may be lost while on a very fine grid the fracture pattern, represented as lines of col-oured pixels, can not be transformed correctly into local shape factors. Accord-ing to eq. 15 the local fractures are supposed to be straight lines.

7   REFERENCES

1. Barenblatt, G.L. , Zheltov, Iu.P. and Kochina I.N. "Basic Consepts in the Theory of Seepage of Homogeneous Liquids in Fissured Rocks", J. Appl. Math. (1960) **24**, 1286.

2. Warren, J.E. and Root, P.J. "The Behaviour of Naturally Fractured Reservoirs", SPE Journal (Sep. 1963) 245.

3. Hazemi, H., Merrill, L.S., Porterfield, K.L. and Zeman, P.R. "Numerical Simulation of Water-Oil Flow in Naturally Fractured Reservoirs", SPE Journal (Dec. 1976) 317.

8   NOMENCLATURE

A	Area of reservoir
g	Gravitational acceleration
j	(subscript) phase index ($j = oil,\ gas,\ or\ water$)
k_r	Relative permeability
k	Absolute matrix permeability
k_x	Absolute matrix permeability in x-direction
k_y	Absolute matrix permeability in y-direction
k_z	Absolute matrix permeability in z-direction
h	Average matrix to fracture flow distance
L	Length of single fracture in grid cell
L_x	Length of matrix block in x direction
L_y	Length of matrix block in y direction
L_z	Length of matrix block in z direction
N^{mb}	Number of matrix blocks contained in a reservoir volume
P^{frac}	Fracture pressure
P^{matr}	Matrix pressure
q^{mf}	Matrix to fracture exchange. Volume per unit time
U	Darcy velocity
V	Reservoir volume
Δx	Length of grid cell in x direction
Δy	Length of grid cell in y direction
Δz	Length of grid cell in z direction
φ	Dip angle of single fracture line in grid cell
μ	Viscosity
ρ	Density
σ_K	Kazemi shape factor
σ_n	Local shape factor in grid cell
σ_T	Effective shape factor for reservoir area

Appendix E

Nørgaard, Olsen, Reffstrup & Springer, SPE Reservoir Evaluation and Engineering 2,2, p 141-148, 1999.

Capillary-Pressure Curves for Low-Permeability Chalk Obtained by Nuclear Magnetic Resonance Imaging of Core-Saturation Profiles

J.V. Nørgaard, SPE, Technical U. of Denmark; **Dan Olsen**, SPE, Geological Survey of Denmark and Greenland; **Jan Reffstrup**, SPE, Dansk Olie og Naturgas A/S; and **Niels Springer**, SPE, Geological Survey of Denmark and Greenland

Summary

A new technique for obtaining water–oil capillary pressure curves, based on nuclear magnetic resonance (NMR) imaging of the saturation distribution in flooded cores is presented.

In this technique, a steady-state fluid saturation profile is developed by flooding the core at a constant flow rate. At the steady-state situation where the saturation distribution no longer changes, the local pressure difference between the wetting and nonwetting phases represents the capillary pressure.

The saturation profile is measured using an NMR technique and for a drainage case, the pressure in the nonwetting phase is calculated numerically. This paper presents the NMR technique and the procedure for calculating the pressure distribution in the sample.

Inhomogeneous samples produce irregular saturation profiles, which may be interpreted in terms of variation in permeability, porosity, and capillary pressure.

Capillary pressure curves for North Sea chalk obtained by the new technique show good agreement with capillary pressure curves obtained by traditional techniques.

Introduction

Accurate petrophysical properties of reservoir rock such as capillary pressure, permeability, and relative permeability functions are essential as input for reliable oil in place estimations and for the prediction of the reservoir performance. Traditional methods for capillary pressure measurements are the mercury injection method, the diaphragm method, and the centrifuge method.

In the mercury injection method,[1] the nonwetting phase is mercury which displaces a gas. The samples are usually evacuated to a low pressure and Hg is then injected in steps allowing for pressure equilibrium at each step, or alternatively Hg is continuously injected. Corresponding data on injected volume of Hg and the injection pressure are recorded. This technique is widely used for measuring capillary pressure functions for low permeability rocks. This is primarily because it is generally believed that pressure equilibrium in each pressure step is readily obtained, while this is normally a problem for other methods where a liquid is the wetting phase. The disadvantage of this technique is the uncertainty in the scaling of the measured data to reservoir fluid data and conditions.

In the diaphragm method or porous plate method, the problem concerning the scaling of the measured data is avoided, since this technique allows for the direct use of reservoir fluids. A water

saturated sample is placed on a water-wet diaphragm to impose a boundary condition $p_c=0$ to the wetting phase, i.e., the wetting phase is allowed to drain through the outlet end of the sample, at the same time as the nonwetting phase (oil or gas) is impeded. Pressure is added to the nonwetting phase and through a limited number of pressure steps, the capillary pressure curve is recorded. However, an important requirement is that equilibrium is obtained at each pressure step. This is the major problem when the diaphragm method is used on microporous materials. The drainage time may be considerable for each step, e.g., several weeks. In recent studies, thin micropore membranes have been used in an attempt to reduce the experimental time.[2] Such a reduction will be less pronounced for low permeability rocks such as chalk since the flow resistance in the core is relatively more important.

In the centrifuge method, the amount of liquid produced from the outlet end of the plug sample at a certain spin rate is read directly from a measuring tube during rotation. From the geometry of the centrifuge, the spin rate and the average fluid saturation in the plug, it is possible to calculate the capillary pressure relative to the inlet end of the sample.[3] However, a number of assumptions must be made[3,4]: the sample must be homogeneous and have a well-defined outlet pressure boundary condition, i.e., $p_c=0$, and drainage equilibrium must be established at each spin rate. Most of these conditions can only be approximated in practice. For the centrifuge method, the condition of drainage equilibrium may be questionable even for sandstone samples.[5] Slobod[6] reported that equilibrium had not been attained for a 2 mD sample after 20 hr of spinning. King[7] concluded that low permeability rock samples may suffer from very long equilibrium times. After 10 days of spinning in the centrifuge, a Berea sandstone sample of 200 mD had just reached equilibrium.

The objective of the development of the method presented here has been to avoid some of the disadvantages of the conventional methods described above. In this method a capillary pressure curve is obtained from a measured saturation profile after flooding the core. A similar experimental procedure was used by Richardson et al.[8] to study end effects associated with flooding processes. The technique described here can be used with reservoir fluids. There is no porous plate to increase the flow resistance and the measurement of the capillary pressure function can be an integrated part of traditional flooding processes as performed with, e.g., unsteady-state relative permeability measurements. Only a very limited number of steps are needed, in principle only one step is required, therefore the time requirement for obtaining drainage equilibrium has not proved to be a problem. The technique utilizes the unavoidable end effect present in experiments with low permeability rocks. The capillary pressure function is obtained from the steady-state saturation profile in the core at drainage equilibrium.

Nuclear magnetic resonance (NMR) imaging is used to measure the saturation profile along the sample, but in principle any
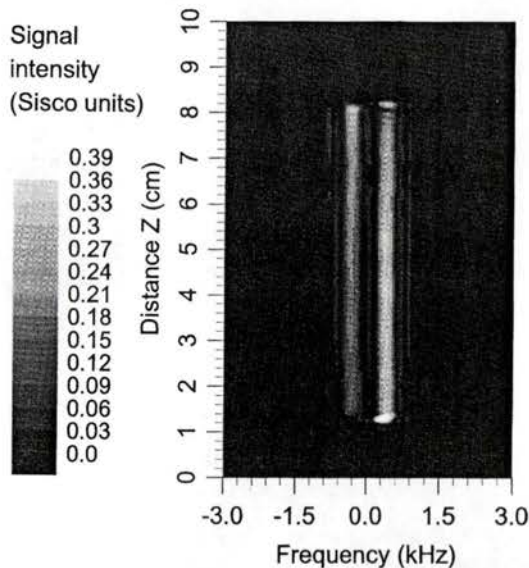
Fig. 1–Gray tone rendering of 2D NMR data set, sample M717. Light shades indicate high signal intensity. Water phase signal to the left of the center frequency, oil phase signal to the right. Inlet end of sample at bottom, outlet end at top. Note the strong gradients in signal intensity along the length of the sample.

the frequency axis of a NMR spectrum. **Fig. 1** shows a gray tone rendering of a data set. To serve as input to the numerical calculation of Eqs. (4) or (5), the frequency dimension must be eliminated. This is done by summation across suitable frequency windows according to

$$M_{1D,w}(N) = \sum_{\omega=f_{w1}}^{f_{w2}} M_{2D}(\omega, N), \qquad (7)$$

$$M_{1D,o}(N) = \sum_{\omega=f_{o1}}^{f_{o2}} M_{2D}(\omega, N), \qquad (8)$$

which is equivalent to area summation in a NMR spectrum. $M_{1D,w}(N)$ and $M_{1D,o}(N)$ are the magnetizations of the water and oil of pixel N in the 1D profile. $M_{2D}(\omega, N)$ is the magnetization at frequency ω, row N of the 2D data set. The water and oil peak magnetizations are separated by approximately 700 Hz, cf. Fig. 1. Summation limits f_{w1}, f_{w2}, f_{o1} and f_{o2} are frequencies chosen to select intervals of 1000 Hz around the water and oil peaks.

Relaxation correction. The initial magnetization M_I in the slice of detection is proportional to the amount of fluid in the selected slice. The magnetization decays in accordance with a law, which is approximated by a single exponential decay

$$M_t = M_I e^{(-t/T_2)}, \qquad (9)$$

where M_t is the magnetization at time t, and T_2 is the spin–spin relaxation constant of the sample. The effect of relaxation is corrected by acquiring CSI1D images for several different echo times T_E and performing a modeling according to Eq. (9) to obtain the initial magnetization M_I for every pixel position of the image set.[21-23] Use of Eq. (9) requires the relaxation to be essentially single exponential, and T_2 to be large enough to allow the signal relaxation to be properly defined. Samples of Maastrichtian chalk are well modeled by a single exponential relaxation model,[22] and T_2 constants of approximately 10 ms allow the relaxation to be adequately defined.[22] Magnetization is measured in arbitrary units (Sisco units).

Proton Density Correction. The intensity profiles resulting from Eqs. (7), (8) and (9) are corrected for the proton densities of

the fluids. Proton densities are calculated from the chemical composition of the fluids. Fluid properties are specified in the Reservoir and Fluid Data section.

Saturation Calculation. Saturation profiles are calculated from the proton density corrected profiles according to

$$S_w(N) = \frac{M_{w,\text{corr}}(N)}{M_{w,\text{corr}}(N) + M_{o,\text{corr}}(N)}, \qquad (10)$$

$$S_o(N) = \frac{M_{o,\text{corr}}(N)}{M_{w,\text{corr}}(N) + M_{o,\text{corr}}(N)}. \qquad (11)$$

$S_w(N)$ and $S_o(N)$ are saturations of water and oil of the Nth pixel in the profile. $M_{w,\text{corr}}(N)$ and $M_{o,\text{corr}}(N)$ are magnetization intensities of water and oil of the Nth pixel in the profile, corrected for relaxation and proton density. It should be noted that the saturations are calculated from intensity ratios. It is therefore not necessary to calibrate the arbitrary Sisco magnetization units to absolute SI units. Equations (10) and (11) are valid if the pore space of the sample does not contain a free gas phase. Care was taken to eliminate free gas from the sample. The resulting profiles for water and oil contain exactly the same information, as $S_w(N) + S_o(N)$ equals 1. Pixel values influenced by the fluids in the end fittings of the core holder are eliminated from the saturation profiles before use in the capillary pressure calculation procedure.

Limitations and Sensitivity of the NMR Method. Spin–spin relaxation and resolution of spectral peaks restrict the choice of samples suitable for NMR saturation profiling. Although the method is only demonstrated for chalk samples, it is considered suitable for many samples which have T_2 time constants greater than 2 ms when measured at 200 MHz. This encompasses samples of limestone and clean sandstone.

The accuracy of the produced NMR profiles is difficult to assess since no comparable method was available for calibration. Comparison of profile mean saturations with conventional bulk saturation determinations indicates an accuracy of 2.0% points on the mean saturation. The accuracy of the pixel saturations is inferior, perhaps around 4% points.

Saturation profiles are typically 256 pixels long, resulting in a spatial resolution of 0.39 mm for a 100 mm profile.

Reservoir and Fluid Data

The core material used for the experiments was chalk of Maastrictian age from the Danish sector of the North Sea. A total of three cores were used. The cores were all cleaned in a Soxhlet extractor using methanol and toluene. After drying, the porosity was determined by a standard helium injection technique.

Capillary pressure functions were measured for one of the test cores, M717, using both the mercury injection technique and the centrifuge method. The measured capillary pressure data for the reference core are shown in **Fig. 2**.

The permeability of the cores varied from 0.9 to 1.7 mD. Porosity varied from 29% to 37%. The average diameter and length of the cores were 3.8 and 7.3 cm, respectively.

Drainage relative permeability functions were not available for the samples used in the present study. Approximate drainage relative permeability functions were obtained from imbibition relative permeability functions by a mapping of the wetting phase saturation axis. In this mapping, the interval $[S_w, 1]_{\text{dr}}$ on the drainage curve saturation axis was mapped onto the interval $[S_{wi}, 1 - S_{or}]_{\text{imb}}$ on the imbibition curve saturation axis by using a linear transformation procedure, described in Appendix A. End points were mapped onto end points. An interior point on the drainage curve saturation axis was mapped onto the mid-point of the interval in the imbibition curve saturation axis. This interior point was adjusted by a regression procedure so that the measured rate for
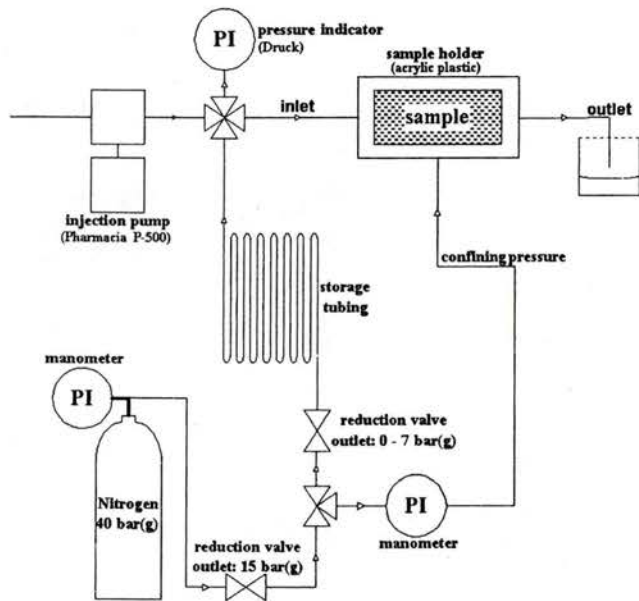
Nørgaard *et al.*: Capillary-Pressure Curves

Fig. 6—sketch of mobile flooding unit.

Fig. 7—Measured saturation distribution, sample M717.

tion. After measurement the sample may be transported back to the laboratory for continued experimentation.

Results

Measuring Capillary Pressure Functions. To test the procedure described above, capillary pressure functions were measured for the same core using mercury injection, the centrifuge method and the technique developed in the present paper. The core, M717, used for this experiment had an absolute permeability of 1.2 mD and a porosity of 32%. Initially the core was fully saturated with simulated formation water. The steady-state saturation distribution for the core was obtained after flooding with laboratory oil at a constant rate of 1 mL/h for a period of 4 days. Breakthrough time was observed after 24 hr, but the flooding was continued in order to ensure steady-state flowing conditions. No water was produced for the last 45 h. Final injection pressure at the steady-state condition was 2.66 bar.

Measured Saturation Distribution. The drainage saturation distribution obtained by the NMR technique for sample M717 is shown in **Fig. 7**. As can be seen from Fig. 7, the saturation increases gradually from $S_w = 0.25$ at the inlet to $S_w \approx 1.0$ at the outlet. The end effect at the outlet of the core is very pronounced for this type of low permeability core. The pressure at the outlet end was fixed to atmospheric pressure.

Capillary Pressure Curve from Saturation Profile. The saturation distribution shown in Fig. 7 was used to calculate the corresponding capillary pressure curve. Because of the very steep saturation gradient in these chalk samples the NMR saturation data are sparse at the outlet of the core, even though the NMR pixel resolution is good. To generate additional data to ensure a smoother capillary pressure curve at high water saturations an interpolation scheme has been adopted. An additional pixel value is generated by linear interpolation between the last pixel within the core and the outlet face value of unity. Then additional values were added between the last three pixels by linear interpolation. A drainage relative oil permeability function is generated by the transformation procedure described in the Reservoir and Fluid Data section. The resulting function is shown in Fig. 4. Using this function, the pressure distribution in the oil phase is calculated directly by Eq.
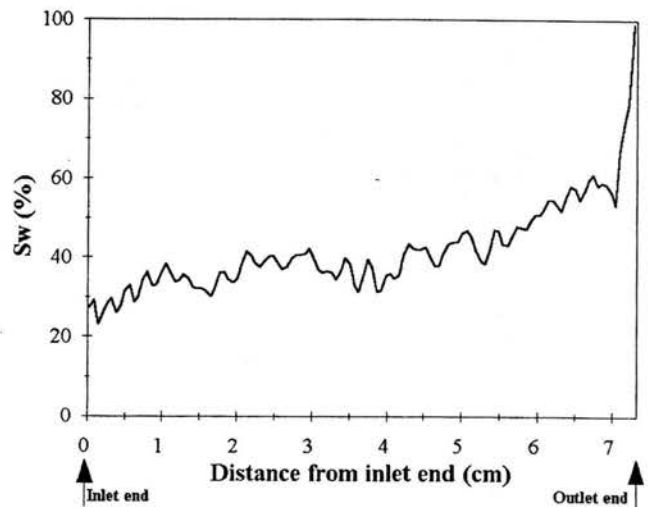
(4) and the corresponding capillary pressure is obtained from Eq. (3). The sensitivity of the procedure to errors in the input imbibition relative permeability function has been investigated by adding an error band of ± 3 saturation % points to the input function, Fig. 3. The resulting error band of the drainage relative permeability function produced by the linear transformation and regression procedure is significantly narrowed, Fig. 3. This further results in a narrow error band for the calculated capillary pressure function, **Fig. 8**.

Comparison of Different Methods. The calculated capillary pressure curve was compared with capillary pressure curves measured with Hg and the centrifuge methods. Hg capillary pressure curves were scaled according to Eq. (6), using interfacial tensions listed in the Reservoir and Fluid Data section. Data obtained by the centrifuge technique could be directly compared since the same fluids were used in the centrifuge and saturation profile experiments. A direct comparison of the three methods is presented in Fig. 8. It is seen that the deviation between the centrifuge technique and the saturation profile technique is small. The threshold pressure and the plateau are correctly predicted. Since the
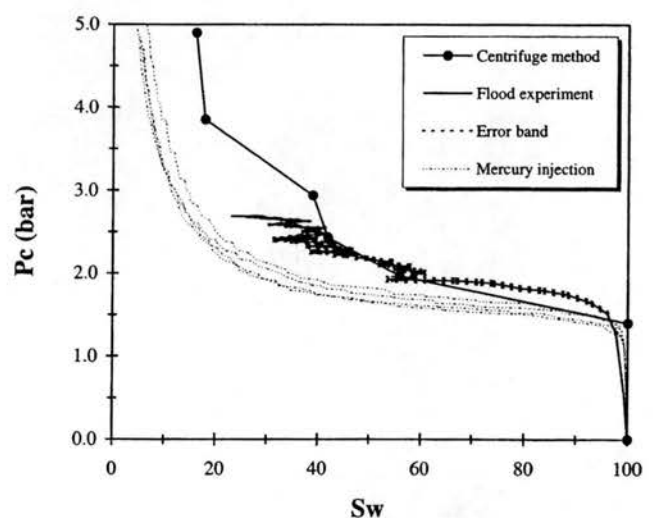

Fig. 8—Comparison of capillary pressure curves measured by the saturation profile method with conventional centrifuge and Hg-injection methods, sample M717.

observed. The variations are large compared to the precision of the NMR method. The variations are believed to be caused by the observed inhomogeneities in the core. Using the scaling function of Eq. (6), the variations in saturation could be expressed as an equivalent variation in the permeability or porosity distribution.

Conclusions

A new procedure for obtaining drainage capillary functions has been developed, described and demonstrated. Detailed saturation profiles in low permeability chalk display a pronounced capillary retention of the wetting phase at the end of drainage experiments, commonly known as the capillary end effect. Steady-state saturation profiles are recorded by an NMR imaging technique and the capillary pressure functions are calculated from the pressure distribution of the displacing fluid.

Saturation profiles with a spatial resolution of 0.39 mm, and a mean accuracy on saturations of 2% points were generated by the NMR technique. The technique used is at present restricted to rock material having T_2 time constants above 2 ms measured at 200 MHz, and susceptibility contrasts low enough to allow resolution of spectral peaks. A mobile flooding unit with a nonmetallic Hassler-type core holder was developed.

It is demonstrated that the mobile flooding unit enables experiments encompassing repeated NMR measurement of saturation profiles during periods of up to 5 weeks of sustained fluid flow through the sample.

The integrated procedure consisting of the flooding, NMR imaging for obtaining saturation profiles and the suggested calculation procedure, represents an independent new technique for obtaining capillary pressure functions. Since reservoir fluids may be used directly, the method does not depend on correct scaling assumptions for the rescaling of the measured capillary pressure curves, as in the case of the Hg technique.

It is further inferred that variation in reservoir properties, such as porosity and permeability, can be related to variations in the detailed saturation profile. Consequently, a quality check of the homogeneity — and hence representativity — of the sample used is directly obtained.

A comparison between drainage capillary pressure functions acquired by the saturation profile method and the centrifuge method shows good agreement.

The use of the NMR technique for obtaining the capillary pressure functions imposes practical restrictions on the choice of samples and on pressure and temperature conditions. All measurements were carried out at room conditions. If other saturation measurement techniques were to be applied at elevated temperature and pressure, e.g., resistivity techniques, the procedure described here could, in principle, generate capillary pressure functions on native state samples at reservoir conditions. This would provide the best chance of preserving the reservoir wettability in laboratory tests.

Nomenclature

A = area of cross section, cm^2
f = frequency, Hz
k = absolute permeability, mD
k_r = relative permeability, fraction
L = sample length, cm
M = magnetization, Sisco units
N = pixel row number
p = pressure, bar
q = flow rate, mL/h
S = Fluid saturation, fraction
T_2 = spin–spin relaxation constant, ms
T_E = echo time, ms

t = time, min, ms
x = distance from inlet end, cm
μ = viscosity, cP
σ = interfacial tension, N/m
Φ = porosity, fraction
ω = angular frequency, Hz

Subscripts

c = capillary pressure
dr = drainage
I = relating to initial magnetization
imb = imbibition
o = oil
or = residual oil
$o1,o2$ = summation limits for oil relating to NMR spectrum
w = water
wi = irreducible water
$w1,w2$ = summation limits for water relating to NMR spectrum
t = time
$1D$ = relating to one-dimensional data set
$2D$ = relating to two-dimensional data set

References

1. Purcell, W.R.: "Capillary Pressures — Their Measurement Using Mercury and the Calculation of Permeability Therefrom," *Trans.*, AIME **186**.
2. Hammervold, W.L. and Skæveland, S.M.: "Improvement of the Diaphragm Method for Drainage Capillary Pressure Measurement with Micro Pore Membrane," *Advances in Core Evaluation III*, P.F. Worthington and C. Chardaire-Rivière (eds), Gordon and Breach Science Publishers S.A., Singapore (1993) pp. 91–111.
3. Hassler, G.L. and Brunner, E.: "Measurement of Capillary Pressures in Small Core Samples," *Trans.*, AIME **160**.
4. Christensen, R.L.: "Geometric Concerns for Accurate Measurement of Capillary Pressure Relationships with Centrifuge Methods." SPE Form. Eval. **7**, 311–314 (December 1992).
5. Forbes, P. *et al.*: "Local Saturation Measurements while Centrifuging (MWC) for Improving Centrifuge Capillary Pressure Curve Determination," paper SCA 9215, Presented at the 1992 33rd Annual Symposium of the SPWLA, Oklahoma City, 15–17 June.
6. Slobod, R.L., Chamber, A., and Prehn, W.L.: "Use of Centrifuge for Determining Connate Water, Residual Oil, and Capillary Pressure Curves of Small Core Samples," *Trans.*, AIME **192**.
7. King, M.J., Narayanan, K.R., and Falzone, A.J.: "Advances in Centrifuge Methodology for Core Analysis," paper SCA 9011, Presented at the 1990 Society of Core Analysts Annual Technical Conference, Dallas, 14–16 August.
8. Richardson, J.G. *et al.*: "Laboratory Determination of Relative Permeability," *Trans.*, AIME **195**.
9. Chardaire-Rivière, C. *et al.*: "Simultaneous Estimation of Relative Permeabilities and Capillary Pressure," *SPE Form. Eval.* **7**, 283–289 (December 1992).
10. Anderson, W.G.: "Wettability Literature Survey - Part 4: Effects of Wettability on Capillary Pressure," *J. Pet. Technol.* **30**, 1283–1300 (October 1987).
11. Enwere, M.P. and Archer, J.S.: "NMR Imaging for Core Flood Testing," paper SCA 9218, Presented at the 1992 33rd Annual Symposium of the SPWLA, Oklahoma City, 15–17 June.

Appendix F

Abstract accepted for presentation at the 2001 SPE ATCE, 30 September – 3 October 2001, New Orleans, 2001.

Title:
Improved Determination of Oil/Water Drainage and Imbibition Saturation Functions of Chalk Core Plugs From Flooding Experiments

Authors:
Niels Bech, Dan Olsen and Carsten M. Nielsen

Abstract
This paper presents improvements to a recently developed experimental method which is particularly suitable for the determination of the oil/water capillary pressure and relative permeability for water wet samples of chalk for both drainage and imbibition. Inherently chalk has high capillary pressure, and conventional laboratory determinations of saturation functions on such material are complicated by strong scale effects, particularly by the capillary end effect. The end effect does, however contain detailed information about the saturation functions of the sample and this information is utilized in the method.

The saturation functions are represented by analytical expressions that are determined by matching simulated results and measured data. A three-step core flooding scheme provides the fluid distributions and production data from which the relative permeabilities and capillary pressures are computed for both drainage and imbibition by a least squares technique. A chemical shift NMR technique is used for fluid distribution determination while the simulation of the experiments are carried out by a commercial reservoir simulator.

In previous work with this method simple power functions were used to represent relative permeability functions. The present paper demonstrates the use of more flexible analytical expressions which enables a better representation of certain function shapes. Also an improved representation of capillary pressure is incorporated in the method. The new technique is applied to chalk samples from the North Sea.

For chalk, the procedure is preferable to the mercury injection, centrifuge and porous plate methods. They are mainly developed for rocks of lower capillary pressure and higher mechanical strength and application to chalk may be questionable. The experimental time for the new method is intermediate between the centrifuge and porous plate methods.